Dissertation
submitted to the
Combined Faculties for the Natural Sciences and Mathematics
of the Ruperto-Carola-University of Heidelberg, Germany
for the degree of
Doctor of Natural Sciences

put forward by
Mikhail Leonidovich Goncharov
born in Sevastopol, Ukrainian SSR

Date of oral examination: May 14, 2014

High-precision Penning-trap mass spectrometry
at SHIPTRAP and PENTATRAP
for neutrino physics research

Referees: Prof. Dr. Klaus Blaum

Prof. Dr. Markus Oberthaler

Моим родителям

Abstract

In neutrino physics, a variety of experiments aim for the determination of the neutrino mass by means of the beta-decay and electron-capture spectra, while a detection of the neutrinoless double-electron capture would reveal the Majorana nature of neutrinos. However, a lack of knowledge on the total decay energy (Q-value) of these processes constrains present neutrino experiments.
To this end, high-precision measurements of the Q-values are obligatory. In order to find suitable nuclides for neutrinoless double-electron capture experiments, a determination of the Q-values by direct Penning-trap mass-ratio measurements on ^{106}Pd/^{102}Ru, ^{106}Cd/^{106}Pd, ^{144}Sm/^{144}Nd and ^{156}Dy/^{156}Gd with a relative precision of a few 10^{-9} were performed for the first time at SHIPTRAP using the Time-of-Flight Ion-Cyclotron-Resonance (ToF-ICR) detection technique and the multiresonance phenomenon in ^{156}Dy was discovered.
A novel Phase Imaging Ion-Cyclotron-Resonance detection technique was developed being substantially faster and providing ca. 40-fold gain in resolving power in comparison with the presently used ToF-ICR technique.
The novel Penning-trap mass spectrometer PENTATRAP aims for direct mass-ratio measurements with a relative precision better than 10^{-11}, which is required for the beta-decay and electron-capture experiments. In this context, the PENTATRAP Control System was developed in order to maximize the efficiency of the measurement process.

Zusammenfassung

In der Neutrinophysik beschäftigt sich eine Reihe von Experimenten mit der Bestimmung der Neutrinomasse über den Betazerfall oder Elektroneneinfang, während die Detektion von neutrinolosem doppelten Elektroneneinfang die Majorananatur der Neutrinos zeigen würde. Die Unkenntnis der totalen Zerfallsenergie (Q-Wert) dieser Prozesse beschränkt jedoch derzeitige Neutrinoexperimente.
Daher werden hochpräzise Messungen der Q-Werte benötigt. Um geeignete Nuklide für Experimente bezüglich neutrinolosem doppelten Elektroneneinfang zu finden, wurden Q-Werte von ^{106}Pd/^{102}Ru, ^{106}Cd/^{106}Pd, ^{144}Sm/^{144}Nd und ^{156}Dy/^{156}Gd über direkte Massenverhältnismessungen in Penningfallen mit einer relativen Präzision von 10^{-9} an SHIPTRAP bestimmt. Dabei wurde die Flugzeitionenzyklotron-Resonanzmethode (ToF-ICR) benutzt und ein Multiresonanzphänomen in ^{156}Dy entdeckt.
Eine neuartige, phasensensitive Ionenzyklotronresonanz-Detektionsmethode wurde entwickelt, die wesentlich schneller als derzeit verwendete ToF-ICR Techniken ist und eine 40-fach höhere Auflösung bietet.
Das neuartige Penningfallen-Massenspektrometer PENTATRAP zielt auf direkte Massenverhältnismessungen mit einer relativen Präzision von besser als 10^{-11}, da dies für Betazerfalls- und Elektroneneinfangsexperimente benötigt wird. In diesem Bereich wurde das PENTATRAP Kontrollsystem entwickelt, um die Effizienz des Messprozesses zu maximieren.

Table of Contents

List of Figures

List of Tables

Chapter 1

Introduction

Since Sir Isaac Newton, the meaning of the term "mass" has been evolved from "*The Quantity of Matter*" [1] to the number of definitions depending on the field of physics, nevertheless still being one of the most intricate subjects in modern physics, "the fundamental property of matter" [2]. Together with the term "binding energy" (in the most generic sense) mass measurements constitute a broad range of scientific researches namely known as "mass spectrometry". Since it has started in 1886 with studies of "*Kanalstrahlen*" ("canal rays") in a gas discharge tube by Eugen Goldstein [3] and continued by J. J. Thomson with the discovery of the electron and the measurement of its mass-to-charge ratio[1] [4], today mass spectrometry is a standard technique in a wide range of applications, which are often departing from the scope of natural sciences.

In contemporary physics mass spectrometry plays a major role in experimental studies of many phenomena. Within present thesis work we will focus on applications of high-precision atomic mass spectrometry in neutrino physics. However, a brief historical review of a broader range of applications (such as, e.g., nuclear physics or fundamental constants) has to be presented in the following for a better understanding of the work. The first excerpt is the discovery of the mass excess in nuclei, so let us come back to the history of mass spectrometry.

Followed by J. J. Thomson, who also discovered the first stable isotopes (^{20}Ne and ^{22}Ne [5]), his student Francis William Aston conducted a great series of works investigating more than 200 new stable isotopes [6–8]. In his research he used the improved version of the Thomson's mass spectrograph with a velocity-focusing of ions through a sequence of electric and magnetic fields. Aston received the Nobel Prize in Chemistry in 1922 "*for his discovery, by means of his mass spectrograph, of isotopes, in a large number of non-radioactive elements, and for his enunciation of the whole-number rule*". The latter *rule* stated: "*...with the exception of hydrogen*[2]*, all the atomic weights of all elements so far measured are exactly whole numbers on the scale O = 16 to the accuracy of experiment (1 in 1000)*" [6]. This was the first experimental hint to the nuclear fusion reaction[3]

[1] The Nobel Prize in Physics 1906 was awarded to J.J. Thomson "*in recognition of the great merits of his theoretical and experimental investigations on the conduction of electricity by gases*".

[2] The mass of hydrogen was found to be 1.008(1) with respect to the mass of oxygen.

[3] In his Nobel lecture [7] Aston was speaking about the loss of mass due to the formation of helium

and, with the beautiful Einstein's formula $E_0 = mc^2$ [9] giving a distinct connection between the binding energy and mass of a complex system, to the concept of the nuclear binding energy elucidated by Sir Arthur Eddington [10]. Further developments of the spectrograph allowed Aston to improve accuracy up to 1 part in 10000. This was sufficient to derive a nuclear binding energy curve [8], which had a remarkable consequences for science. This curve was in a good agreement with the "*liquid drop model*" proposed by Gamow [11] and developed by von Weizsäcker [12], Bethe and Bacher [13].

New developments in mass spectrometry have been often resulted in the origin of new theories and concepts in atomic, nuclear and astroparticle physics. Improvements can be expressed as an increase in precision of about one order of magnitude per decade [14]. It is well known today, that the highest measurement precision can be achieved if a measurand is expressed in units of a frequency, since a frequency is a quantity which can be measured with the most highest accuracy[4]. In mass spectrometry a conversion from mass measurements to the frequency measurements is a natural property of ion storage devices: Paul traps, storage rings and Penning traps. Here we will focus on the latter one.

A Penning-trap mass spectrometer was developed in the 1950s by Hans Dehmelt[5] and utilized in his experiments on electrons [15]. The trap is a superposition of homogeneous magnetic and quadrupole electric fields (Penning-trap principles are described in 3). Later developments allowed him in the 1970s to trap a single Ba^+ ion for the first time and to perform with his student, van Dyck, high-precision measurements on the electron-to-positron mass ratio [16] in 1980. In parallel, Penning-trap experiments with protons were committed in Mainz by G. Gräff *et al.* [17], where the proton-to-electron mass ratio was measured with a relative uncertainty of 0.6 ppm. Gräff's Penning-trap experiment utilized the Time-of-Flight Ion-Cyclotron-Resonance (ToF-ICR) detection technique, which served as the basis for the first forthcoming high-precision mass measurements on short-lived nuclides at ISOLTRAP (ISOLDE/CERN) in 1990 by H.-J. Kluge *et al.* [18]. To date improvements in cooling and detection techniques have been resulted in relative measurement uncertainties below 10^{-11} for stable nuclides, reported by van Dyck *et al.* (UW-PTMS[6]) [19] and Myers *et al.* (FSU) [20], and better than 10^{-8} for short-lived nuclides (see, e.g., [21–23]).

As it is said above, present thesis work is dedicated to the mass-ratio measurements with high- and ultra high-precisions for needs of neutrino physics. In this field many fundamental questions beyond the Standard Model still lack answers. Since the discov-

nucleus, noticing "*If instead of considering single atoms we deal with quantities of matter in ordinary experience, the figures for the energy become prodigious.*"

[4] A frequency has a native unit of the most accurately known standard – an atomic clock.

[5] Hans Dehmelt received the Nobel Prize for his work on Penning traps together with Norman Ramsey and Wolfgang Paul. The name "Penning trap" was given after Frans M. Penning in order to appreciate his basic idea concerning a superposition of electric and magnetic fields.

[6] The experiment moved in 2008 from the University of Washington (Seattle, US) to MPIK (Heidelberg, Germany), where the measurements on the mass ratio of ^{3}He and ^{3}H with a higher resolution are to be continued (details are given in Sec. 2.3.1).

ery of neutrino flavor oscillations in the atmospheric neutrino flux [24], the neutrino is known to be a massive particle. However, its absolute mass value remains one of the main questions in modern physics. A variety of experiments aim to the direct mass determination of the electron (anti-)neutrino (details are given in Sec. 2.3). To perform the experiment one should know Q-values (total decay energy between ground states of mother and daughter nuclides) of corresponding processes with an extremely high accuracy below few eV, what means better than 10^{-11} for medium-heavy nuclides. Within this mass range it is planned to measure a β-decay spectrum of ^{187}Re (the MARE project [25]) and electron capture (EC) in ^{163}Ho (the ECHo project [26]) by means of cryogenic microcalorimetry. In addition, for the development of these projects it is necessary to know Q-values with an accuracy of about 50 eV (or a few times 10^{-10}), since the Q-value is linked to the amount of the required detector material.

The Q-value measurements with a precision below 10^{-11} is one of the main goals of the novel Penning-trap mass spectrometer PENTATRAP, which is located at the Max-Planck-Institute for Nuclear Physics in Heidelberg, Germany [27]. PENTATRAP is the first open Penning-trap setup utilizing a stack of five Penning traps in a cryogenic environment. Such a system has several unambiguous advantages over an ordinary Penning-trap setup. First of all, it will be possible to measure simultaneously frequencies of two ion species in adjacent traps, what should significantly decrease the effect of the magnetic field fluctuations. A cryogenic environment allows to employ highly sensitive non-destructive detection techniques together with the effective resistive cooling. Moreover, openness grants access to highly charged medium-heavy and heavy ions, produced by two independent Electron Beam Ion Traps (EBIT). It is a remarkable property since the precision of the Penning trap scales with the charge-to-mass ratio of the ion, and ultra-high precision mass measurements on medium-heavy and heavy nuclides become feasible.

Another open question in neutrino physics is whether a neutrino is its own anti-particle (a Majorana particle) or not (a Dirac particle). The unambiguous proof of a Majorana nature of the neutrino could be done with experiments on neutrinoless double-beta processes (see Sec. 2.4). Here the neutrinoless double-electron capture ($0\nu\epsilon\epsilon$) is promising, since it lacks a continuous background problem of the double-beta decay. In general, nuclides which can undergo $0\nu\epsilon\epsilon$-decay are virtually stable and thus prevents a performance of the experiment, but in rare cases the decay probability can be enhanced resonantly to the experimentally feasible value. The search for suitable candidates requires to know Q-values of the mother and daughter pairs with an uncertainty better than a few hundreds eV (meaning a few times 10^{-8} and better in the corresponding mass range). In order to find proper candidates for $0\nu\epsilon\epsilon$-capture a series of works was performed with several Penning-trap mass spectrometers (a comprehensive overview can be found in [28]). A majority of measurements was done with the SHIPTRAP mass spectrometer at GSI (Darmstadt, Germany), using the Ramsey ToF-ICR detection technique. The Q-values were measured with the relative uncertainty around 10^{-9}, and two perspective results were obtained. First, a transition in ^{152}Gd to the nuclear ground state of ^{152}Sm was found to be resonantly enhanced with the estimated half-

life of 10^{26} years[7]. Second, an interesting multiresonance phenomenon in ^{156}Dy was discovered.
Recently in the field of Penning-trap mass spectrometry on short-lived nuclides a new elegant Phase-Imaging Ion-Cyclotron-Resonance (PI-ICR) detection technique was developed at SHIPTRAP. The goal of the new technique is to improve resolving power and to decrease the measurement time while keeping the precision constant as compared to the presently used ToF-ICR detection technique. In PI-ICR the radial motion of the ion in the trap is projected onto a high-resolution position-sensitive detector, and the free cyclotron frequency is determined from the phases of the radial eigenmotions. The new technique shows a gain 40 in resolving power and allows to provide substantially faster measurements in comparison with the Ramsey ToF-ICR technique. Thus, it provides a gain of ~ 5 in precision resulting in the absolute uncertainty of about 75 eV/c^2 for the medium-heavy ions. Coming back to the development of the MARE and ECHo projects, the PI-ICR technique could be a proper instrument for the mass-ratio measurements of corresponding nuclides with the required precision of a few 10^{-10} and better in order to provide a systematic check of those experiments.

This thesis is organized in the following order:

Chapter 2 gives an introductory overview concerning the problems of neutrino physics, where Penning-trap mass spectrometry can be employed, and highlights corresponding experiments.

Basic principles of Penning traps are described in chapter 3.

Mass-ratio measurements on ^{106}Cd, ^{102}Pd, ^{144}Sm and ^{156}Dy with relative uncertainty of a few ppb and better for the Q-value determination of neutrinoless double-electron capture are presented in chapter 4. The measurements were performed at SHIPTRAP by means of the Ramsey ToF-ICR technique.

A novel PI-ICR detection technique, developed recently at SHIPTRAP, together with systematic studies is presented in chapter 5.

Chapter 6 is dedicated to the novel five-trap mass-spectrometer PENTATRAP. After a short review of the experimental setup, the chapter will focus on the development of the PENTATRAP Control System.

In conclusion, achieved results and future perspectives are summarized in chapter 7.

[7]The estimated half-life is normalized to the effective Majorana neutrino mass $|m_{\beta\beta}| = 1$ eV.

Chapter 2

High-precision mass spectrometry for neutrino physics

As it is stated in Chap. 1, Penning-trap mass spectrometry can contribute to neutrino physics with high-precision measurements on the Q-values of respective β-decays. The following chapter reveals in brief the problems of neutrino mass and nature, gives an overview on the corresponding experiments, which are related to the present work, and explains the role of the mass ratio measurements within neutrino physics research.

2.1 Introducing the neutrino

A nuclear β-decay was systematized in 1899 by Ernest Rutherford out of the nuclear radioactivity discovered by Henri Becquerel and Marie and Pierre Curie couple of years before [29]. A broad continuous spectrum of the β-decay (experimentally shown in 1908 by Lise Meitner and Otto Hahn, see citations, e.g., in [29]) was in contradiction with the main conservation laws of a system consisting of a nucleus emitting a single particle, which would produce a mono-energetic spectrum. Wolfgang Pauli in 1930 postulated a hypothetical idea[1] that it could be a three-body system, and the third unknown particle should be involved there. It was named "*neutrino*" by Enrico Fermi in his theoretical paper concerning the beta-radioactivity [31].
Within the Standard Model (SM), neutrinos are assumed to be electrically neutral lepton fermions with zero mass [32]. They are subject only to the weak interaction and thus their direct detection causes experimental difficulties. Three flavors of neutrinos $\{\nu_e, \nu_\mu, \nu_\tau\}$ and their anti-neutrinos $\{\overline{\nu}_e, \overline{\nu}_\mu, \overline{\nu}_\tau\}$ are known today, corresponding to three generations of charged leptons $\{e^-, \mu^-, \tau^-\}$ and their anti-particles $\{e^+, \mu^+, \tau^+\}$. In the SM a lepton charge for each flavor is assumed to be conserved and only left-handed neutrinos (and right-handed anti-neutrinos) are considered.
If neutrinos are not massless particles, their flavor eigenstates should differ from their mass eigenstates. As a consequence, neutrino flavor oscillations or transformations between the neutrino flavors should take place. Both concepts were predicted by Ziro

[1] Pauli's letter to the Physical Society of Tubingen is reproduced in [30].

Maki, Masami Nakagawa and Shoichi Sakata [33] and Bruno Pontecorvo [34] in the 1960s. Since the first hints on the neutrino oscillations [35], the very fundamental question has been pronounced: if the neutrino is a massive particle, how massive should it be and why is it so much lighter than the charged leptons? The latter could be explained, e.g., if the neutrino is its own anti-particle or a Majorana particle rather than a Dirac particle. An observation of the neutrinoless double-beta decay will be the evidence of the Majorana nature of the neutrino. All these questions underlay the neutrino theory beyond the Standard Model.

2.2 Neutrino flavor oscillations

Neutrino mixing appears from the generalization of the weak interaction theory[2]. There the massive neutrino flavors are linear combinations of mass eigenstates with the corresponding coefficients, which form a so-called Pontecorvo-Maki-Nakagawa-Sakata (PMNS) unitary matrix:

$$|\nu_l\rangle = \sum_{i=1}^{3} U_{li} \, |\nu_i\rangle \, , \tag{2.1}$$

where l denotes three flavors $\{e, \mu, \tau\}$, ν_i is a mass eigenstate and U_{li} are the matrix coefficients, depending on three mixing angles θ_{12}, θ_{13}, θ_{23} and on three CP-violating phase factors: a Dirac phase factor δ and Majorana phase factors α_1 and α_2. For a two neutrino case with a mixing angle $\theta_{j,k}$ and assuming the neutrino momentum $p >> m_{j,k}c$, the probability that the neutrino, created in the flavor state $|\nu_\alpha\rangle$, is in the state $|\nu_\beta\rangle$ at the distance L from a neutrino source, is given by

$$P\left(|\nu_\alpha\rangle \rightarrow |\nu_\beta\rangle\right) = \sin^2\left(2\theta_{j,k}\right) \sin^2\left(\frac{\pi L}{L_{jk}^{\mathrm{osc}}}\right), \quad \text{with} \;\; L_{jk}^{\mathrm{osc}} = \frac{4\pi E}{m_j^2 - m_k^2} \, , \tag{2.2}$$

where $m_{j,k}$ are masses of the neutrino eigenstates and E is the energy of the neutrino. Eq. (2.2) shows a clear oscillatory behavior and a mass-difference dependence of the probability, and thus the observation of the neutrino flavor oscillations should mean different and non-zero masses (or at least one mass) of the neutrinos.
As it is mentioned in Sec. 2.1, the first hints on the neutrino oscillations appeared in 1968 by Davis *et al.* [35], who found that the detected radioactivity, induced by the solar neutrino flux, is less than the expected one. 30 years later, in 1998, a strong evidence of the atmospheric neutrino oscillations was published by the Super-Kamiokande experiment [36], where the dominance of the $\nu_\mu \leftrightarrow \nu_\tau$ oscillation was observed. The SNO (Sudbury Neutrino Observatory) collaboration was able to detect the solar flux from all neutrino flavors, what gives today probably the best estimate on the Δm_{21}^2 [37]. Combining the results of all neutrino oscillation experiments, the summary analysis of

[2] As a good primer on the neutrino physics see, e.g., [32].

the data [38] estimates the mass differences of the eigenstates to be

$$\begin{aligned} \Delta m^2_{21} &= (7.59 \pm 0.20) \cdot 10^{-5} \left(\mathrm{eV/c^2}\right)^2, \\ \Delta m^2_{32} &= (2.43 \pm 0.13) \cdot 10^{-3} \left(\mathrm{eV/c^2}\right)^2. \end{aligned} \tag{2.3}$$

Although the neutrino oscillation experiments provided unambiguous proofs of the massiveness of the neutrinos and of the lepton number violation, a question on absolute masses remains unresolved. Numerous experiments worldwide aim to the direct mass measurements of the (anti-)neutrinos, some of them with the relation to the topic of the thesis will be introduced in the next section.

2.3 Single-beta decay transitions and neutrino mass

In Sec. 2.1 a neutrino was introduced in order to interpret a continuous spectrum of a β^--decay:

$$(\mathrm{Z,\ A}) \rightarrow (\mathrm{Z{+}1,\ A}) + e^- + \overline{\nu}_e. \tag{2.4}$$

Here a neutron within the parent atomic nucleus transforms into a proton while emitting an electron e^- and an electron anti-neutrino $\overline{\nu}_e$. It is a weak spontaneous process. As it was already mentioned by Enrico Fermi [31] in 1934, a neutrino mass can be derived from the shape of the electron energy distribution spectrum. In the simplest case, assuming the absence of the neutrino mixing and a transition to the ground state, the electron energy distribution spectrum can be written from the kinematics of the process and Fermi's Golden Rule in the following form [39]:

$$\frac{dN}{dE} \sim \frac{1}{2\pi^3} G_F^2 V_{ud}^2 \left|M\right|^2 F(E,Z) pE \left(E_0 - E\right) \sqrt{\left(E_0 - E\right)^2 - m_\nu^2 c^4}, \tag{2.5}$$

where G_F is the Fermi constant, V_{ud} is the element of the Cabibbo–Kobayashi–Maskawa (CKM) matrix [40, 41], M is the nuclear matrix element of the transition, $F(E,Z)$ is the Coulomb function, p and E are the energy and momentum of the electron, E_0 is the maximal endpoint energy of the spectrum and m_ν is the electron anti-neutrino mass. From Eq. (2.5) it is expected that the neutrino mass should distort the spectrum significantly in the very closest range to the endpoint energy, where the free electrons have the maximal energy and the neutrino is at rest. The relation between the maximal electron energy, the total energy of the decay and the neutrino mass in the non-relativistic approach is given by

$$E^{\max} \cong E_0 - m_\nu c^2 = \left[m(\mathrm{Z,\ A}) - m(\mathrm{Z{+}1,\ A}) - m_\nu\right] c^2, \tag{2.6}$$

where the total energy is a Q-value or a mass difference between mother and daughter nuclides (here the recoil energy of the nucleus and the atomic electron energy difference

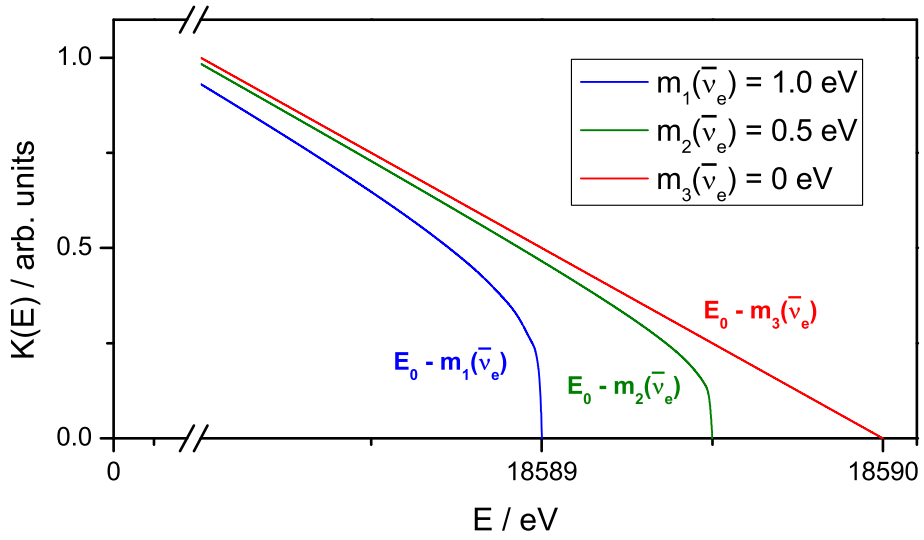

Figure 2.1: Kurie plots of Eq. (2.8) of the tritium β-decay near the endpoint $E_0 \approx 18590$ eV. A picture shows the effect of three different neutrino masses as the difference in the maximal endpoint energies. The amplitude of the spectra is not representative.

are neglected[3]):

$$E_0 \equiv Q = [m(\mathrm{Z},\ \mathrm{A}) - m(\mathrm{Z{+}1},\ \mathrm{A})]\, c^2. \tag{2.7}$$

It is convenient to transform Eq. (2.5) into a Kurie plot (omitting the energy-independent constants) in order to emphasize the dependence of the spectrum from the neutrino mass:

$$K(E) \equiv \sqrt{\frac{dN/dE}{F(E,Z)pE}} \sim (E_0 - E) \sqrt[4]{1 - \left(\frac{m_\nu c^2}{E_0 - E}\right)^2}. \tag{2.8}$$

Fig. 2.1 shows a Kurie plot for the β-decay of tritium. For a massless neutrino the spectrum is a straight line crossing the abscissa at $E = E_0$. Assuming the neutrino mass $m_\nu \neq 0$, the maximum energy shifts correspondingly, revealing a possibility of the direct experimental anti-neutrino mass determination. The latest estimates of the neutrino mass from cosmology and previous direct experiments give a value of $m\,(\overline{\nu}_e) < 2$ eV/c^2 at 95% CL [38]. However, in this region the count rate is depressed drastically (e.g., it is below 10^{-13} in 10^{11} tritium decays per second in the last 1 eV [43]), challenging experimentalists to aim for extremely high resolution techniques.

[3] For the precise mass determination of the neutrino it is important to have a solid theoretical description of the process. However, as it is shown, e.g., in [39], accurate relativistic calculations of a β-decay of tritium involving the recoil energy of the nucleus, which is ~ 3.4 eV, give the same Kurie function as in the non-relativistic approach due to a small Q-value of ~ 18.6 keV. In addition, ionization energies of corresponding atoms are known with exhaustive accuracies (see, e.g., [42]).

2.3.1 Tritium beta-decay

As stated, in a direct neutrino mass determination the task is to measure the very end of a β-decay spectrum with a resolution < 1 eV according to the current neutrino mass estimations. One of the keystones here is a source of β-decaying nuclides, which should comprise altogether a sufficient activity, a low background and a low endpoint energy. The latter is very important since the count rate in a tiny region ΔE slightly below the endpoint energy E_0 scales as

$$n\,(E_0 - \Delta E) \sim (\Delta E/E_0)^3 \;\; [44]. \tag{2.9}$$

Therefore tritium has been found to be one of the most attractive isotopes for direct neutrino mass determination experiments. It experiences a pure β-decay with a half-life of 12.32 y and a low Q-value of 18589.8(12) eV [45]. The ^{3}H isotope and its daughter, ^{3}He, have a simple atomic structure resulting in simple theoretical calculations of atomic corrections. Moreover, a $^3\mathrm{H} \rightarrow {}^3\mathrm{He}$ β-transition is super-allowed, what simplifies significantly a calculation of the nuclear matrix element.
Up to date, various experiments employed tritium as a β-emitter using different measurement techniques. However, the required sensitivity has not been reached so far. The most precise upper limits on the electron anti-neutrino mass have been given independently with similar uncertainties by Troitsk [46] and Mainz [47] experiments, based on the electrostatic filters with magnetic adiabatic collimation[4] (MAC-E-Filters). Their results are dominant in the last final estimation of the today's mass limit [38]:

$$m\,(\overline{\nu}_e) < 2 \text{ eV}/c^2 \quad \text{at } 95\% \text{ CL}. \tag{2.10}$$

At the moment both groups collaborate in order to improve the result, developing the novel **Ka**rlsruhe **Tri**tium **N**eutrino (KATRIN) experiment in Karlsruhe, Germany [43, 44]. The main technical improvement is a colossal increase of the size of the MAC-E-Filter, what should give a 10-times better sensitivity on the mass determination. As a consequence of the statistical and systematic uncertainties, the planned upper limit is

$$m\,(\overline{\nu}_e) \leq 0.2 \text{ eV}/c^2 \quad \text{at } 90\% \text{ CL}. \tag{2.11}$$

Independent measurements of the Q-value of the tritium β-decay should provide a check on systematic errors of the KATRIN experiment. Here the required precision can be reached by Penning-trap mass spectrometry [48]. Today the most precise measurement of the $^3\mathrm{H} - {}^3\mathrm{He}$ mass difference is given by SMILETRAP [45]:

$$Q(^3\mathrm{H} \overset{\beta^-}{\rightarrow} {}^3\mathrm{He}) = 18589.8(12) \text{ eV}. \tag{2.12}$$

[4] In MAC-E-Filters electrons after a β-emission are guided through a combination of magnetic and electric fields, while their energy is controlled. Only electrons of a certain energy are detected. A β-source and a detector are separated by an effective distance, which defines a spectrometer's resolution and gives several systematic problems.

However, a planned sensitivity of the KATRIN mass spectrometer requires at least a 200-times higher precision in the Q-value determination, what is the main challenge of the THe-Trap (**T**ritium-**He**lium-Trap) [49] (a former UW-PTMS experiment, see Chap. 1) and the FSU-TRAP experiments[5]. The project now is on the final stage of development at the Max-Planck-Institute for Nuclear Physics (Heidelberg, Germany).

2.3.2 Rhenium beta-decay

A β^--decay of ^{187}Re is an alternative to the tritium experiments. It has an even lower Q-value of 2466.7(16) eV [50], but a longer half-life $T_{1/2} \approx 43.2$ Gy, what means that a massive solid β-source should be used and MAC-E-Filter spectrometers are no longer applicable. In this case modern cryogenic micro-calorimeters (or cryo-bolometers) are proper tools for ^{187}Re β-decay investigations. Here total decay energy is measured as a heat dissipation in a volume of a solid detector containing a source material, what allows to avoid many systematic effects of the tritium experiments (for details on a comparison between two techniques see, e.g., [51]).
Bolometric spectrometry of ^{187}Re have been already done by two experimental groups: MANU [52] utilizing a single metallic rhenium crystal and Mi-BETA [53] with arrays of ten crystals of silver perrhenate ($AgReO_4$). The first group reported on an electron anti-neutrino mass limit of 26 eV/c^2 (95% CL) [54] from about 6×10^6 statistical events, while the second group gave a limit of $m(\overline{\nu}_e) < 15$ eV/c^2 at 90% CL processing $\sim 6.2 \times 10^6$ decay events [55].
After these achievements both groups have incorporated into a new ambitious project MARE [25] (Micro-calorimeter Array for a Rhenium Experiment) to proceed further in sensitivity up to modern expectations of the neutrino mass. A new experiment consists of two consecutive steps, each step requires an improvement in sensitivity by a factor of 100. This will be done by multiplying the number of detectors as well as by increasing the size of source crystals. Thus, a new limit of $m(\overline{\nu}_e) \leq 0.2$ eV similar to the KATRIN project is aimed for.
The most precise Q-value of the $^{187}\text{Re} \rightarrow {}^{187}\text{Os}$ β-decay (dominating in the latest AME 2012 adjustment [50]) is given by Mi-BETA [55]:

$$Q(^{187}\text{Re} \xrightarrow{\beta^-} {}^{187}\text{Os}) = 2465.3(16) \text{ eV}. \tag{2.13}$$

For calibration purposes this value should be measured with a higher precision well below 1 eV. In terms of relative uncertainties this means about 5 parts in 10^{12}. Such high-precision measurements are planned with the novel Penning-trap mass spectrometer PENTATRAP (see Chap. 6). Moreover, an uncertainty of about a few tens eV can provide a systematic check of a development of the MARE experiment concerning the necessary amount of detector material. This can be done by means of the new PI-ICR technique recently implemented at SHIPTRAP (Chap. 5) [56, 57].

[5] http://fsunuc.physics.fsu.edu/~myers/projects.html

2.3.3 Electron capture in ^{163}Ho

Besides the β^--decay experiments, an electron-capture process (EC) can resolve an electron neutrino mass problem, and, in addition, in case of the experimental equivalence $m(\overline{\nu}_e) \equiv m(\nu_e)$, prove the CPT-symmetry in weak interactions. In this process a nucleus absorbs an electron from the closest shell of an atom and emits an electron neutrino ν_e, while a proton turns into a neutron:

$$(\mathrm{Z},\ \mathrm{A}) + e^- \rightarrow (\mathrm{Z\text{-}1},\ \mathrm{A}) + \nu_e. \tag{2.14}$$

Subsequently a daughter atom de-excites emitting X-rays, Coster-Kronig and Auger electrons. Energy balance of the process is given by the following equation:

$$m(\mathrm{Z},\ \mathrm{A})c^2 = m(\mathrm{Z\text{-}1},\ \mathrm{A})c^2 + E_H + E_\nu + m_\nu c^2, \tag{2.15}$$

where E_H is the de-excitation energy of the daughter nuclide (which equals approximately to the binding energy of the captured electron), E_ν is the kinetic energy of the neutrino, and the recoil energy is neglected. Introducing a Q-value of the decay, Eq. (2.15) converts into

$$Q_{\mathrm{EC}} - E_H = E_\nu + m_\nu c^2, \tag{2.16}$$

where

$$Q_{\mathrm{EC}} = \left[m(\mathrm{Z},\ \mathrm{A}) - m(\mathrm{Z\text{-}1},\ \mathrm{A})\right] c^2. \tag{2.17}$$

A probability of the electron capture has a form similar to the β^--decay [58]:

$$\lambda_{\mathrm{EC}} \sim (Q_{\mathrm{EC}} - E_H) \sqrt{(Q_{\mathrm{EC}} - E_H)^2 - m_\nu^2 c^4}\ . \tag{2.18}$$

Thus, if a total decay spectrum minus the neutrino energy is measured, then an influence of the neutrino mass on the shape of the spectrum is more pronounced if Q_{EC} is close to the binding energy of the electron, while the maximal released energy of the EC-spectrum is defined as $E^{\max} = Q_{\mathrm{EC}} - m_\nu c^2$.
Several isotopes were considered to have a $Q_{\mathrm{EC}} - E_H$ difference small enough for the neutrino mass determination (see, e.g. [59]). Among them ^{163}Ho is the most promising candidate today. It has the lowest known $Q_{\mathrm{EC}} = 2555(16)$ eV [50], a half-life of about 4570 y and the binding energy of the M1 electron $B_{M1} = 2128$ eV [60]. The best limit on the electron neutrino mass has been obtained using the inner bremsstrahlung emitted in the EC decay of ^{163}Ho [38, 61]:

$$m(\nu_e) < 225\ \mathrm{eV}/c^2 \quad \text{at } 95\%\ \mathrm{CL}. \tag{2.19}$$

Today a new project named ECHo (Electron Capture in Holmium) aims to achieve a sensitivity on the electron neutrino mass determination better than a few eV by means

of metallic magnetic calorimeters [26]. Together with a total de-excitation spectrum it is necessary to know Q_{EC}, and thus to fix the endpoint, with a very high precision better than 1 eV. Current results of the ECHo collaboration have provided $Q_{\mathrm{EC}} = 2.80(8)$ keV, what is in contradiction with the latest AME evaluation [50]. Hence independent measurements of the ^{163}Ho – ^{163}Dy mass difference are of a great importance and is one of the main goals of PENTATRAP, where the uncertainty better than 10^{-11} is to be reached.

2.4 Double-beta decay transitions and neutrino origin

While a study of single β-transitions is probably the most suitable way to solve the question on the neutrino mass, another important problem is whether the neutrino is a Dirac or a Majorana particle. It comes from a theoretical side in attempts to describe neutrino physics in a qualitative way. Being an uncharged massive fermion, neutrinos can be indistinguishable from their own anti-particles (a Majorana type) violating the lepton number conservation law, and this can be tested experimentally via the neutrinoless double-beta processes. Moreover, on a direct neutrino mass determination double-beta transitions can be less promising, but still appropriate from the experimental point of view.

2.4.1 Neutrinoless double-beta decay

An electron double-beta decay ($2\nu\beta\beta$) is a second order weak process, where two neutrons in the nucleus decay simultaneously, emitting two electrons and corresponding anti-neutrinos:

$$(\mathrm{Z},\ \mathrm{A}) \rightarrow (\mathrm{Z{+}2},\ \mathrm{A}) + 2e^- + 2\overline{\nu}_e. \tag{2.20}$$

It was proposed by Maria Goeppert-Mayer [62] in 1935, and a possibility of the neutrinoless decay was proposed in 1939 by Furry [63]:

$$(\mathrm{Z},\ \mathrm{A}) \rightarrow (\mathrm{Z{+}2},\ \mathrm{A}) + 2e^-, \tag{2.21}$$

where an anti-neutrino is emitted and consumed by the nucleus (a so-called virtual exchange) (see Fig. 2.3 a) – the process, which is allowed only for massive Majorana neutrinos [64]. The probability of the neutrinoless double-beta decay ($0\nu\beta\beta$) scales with the absolute square of the so-called effective Majorana neutrino mass $|m_{\beta\beta}|^2$ [65]

$$\lambda_{0\nu\beta\beta} = G_{0\nu\beta\beta}|M_{0\nu\beta\beta}|^2|m_{\beta\beta}|^2, \tag{2.22}$$

where $G_{0\nu\beta\beta}$ is a phase-space factor (see Fig. 2.2) and $M_{0\nu\beta\beta}$ is the nuclear matrix element. $G_{0\nu\beta\beta}$ depends on the Q-value of the decay as $\sim Q^{10}$ and on the Fermi coupling constant as $\sim G_F^4$. Thus, the probability of the transition is strongly suppressed by the weak interaction constant. Besides that it is a very long process with half-lives of more

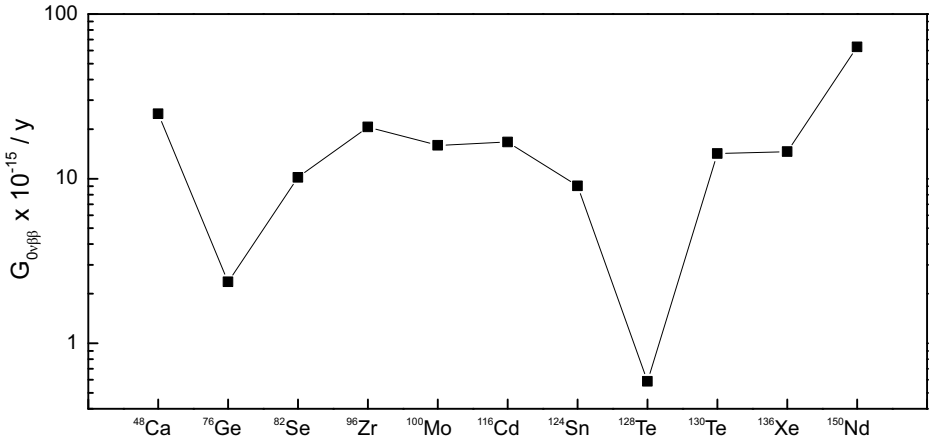

Figure 2.2: Phase-space factors $G_{0\nu\beta\beta}$ of the neutrinoless double-beta transitions in the listed isotopes, calculated in [65] using screened exact finite-size Coulomb wave functions.

than 10^{20} y, a double-beta decay can be observable only when a single-beta decay is suppressed energetically. This happens if M(Z,A) − M(Z+1,A) is not enough for an ordinary β-decay, while M(Z,A) − M(Z+2,A) is enough for a double-beta transition. From the experimental point of view, a signature of the $0\nu\beta\beta$-decay is the detection of two emitted electrons in a coincidence resulting in a peak at the endpoint energy of the spectrum $Q_{\beta\beta} = M$(Z,A) − M(Z+2,A), while the shape of the $2\nu\beta\beta$ spectrum is continuous and similar to the β-decay spectrum.
In the last few decades a great experimental work has been done in order to observe the neutrinoless double-electron transition. However, no single evidence of $0\nu\beta\beta$ above background has been found so far. A brief historical review and the current status of the experiments can be found in [66, 67]. At the moment, several experiments employing the $0\nu\beta\beta$-decay reported on effective Majorana neutrino mass limits between 170 and 900 meV at 90% CL (Heidelberg-Moscow [68], Cuoricino [69], NEMO-3 [70]), and many of them are running or in a preparation (see references in [67]).
It is worth mentioning that the task of registering the $0\nu\beta\beta$-decay against the background of the $2\nu\beta\beta$-decay requires to know preliminary $Q_{\beta\beta}$ with very high precisions, where Penning-trap mass spectrometry plays a significant role (see, e.g., [71–73]).

2.4.2 Neutrinoless double-electron capture

In the previous section it is pointed out that a peak of the $0\nu\beta\beta$-decay would reveal the neutrino nature and provide a proper value of the Majorana neutrino mass. However, a competitive $2\nu\beta\beta$-decay produces an exceedingly large background imposing strong constraints to the experiments: extreme shielding conditions, an extra high purity of the detector material, a high resolution of the detector are required in a search for $0\nu\beta\beta$. On the other hand, there is another second order weak process, which can solve fundamental problems of neutrino physics – a neutrinoless double-electron capture

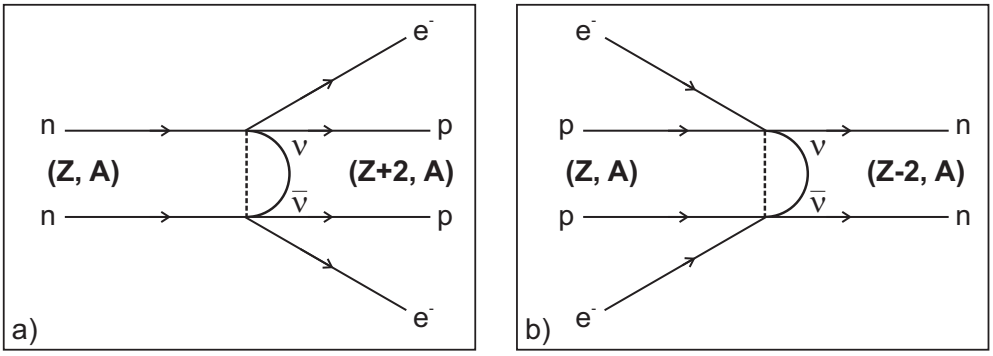

Figure 2.3: Exemplary Feynman diagrams of two neutrinoless double-beta processes: a double-beta decay with emission of two electrons (a) and a double-electron capture (b). Two neutrons decay into two protons and *vice versa*, correspondingly, while a neutrino is emitted by one nucleon and consumed by another one (a virtual exchange), what is possible only in a Majorana neutrino case.

($0\nu\epsilon\epsilon$).
A simplified Feynman diagram illustrates the process in Fig. 2.3 b). Two protons in a nucleus capture two electrons from the closest atomic shells, decaying into neutrons with a virtual neutrino exchange, which is only the case of the neutrino being a massive Majorana particle. The energy diagram of the $0\nu\epsilon\epsilon$ is shown in Fig. 2.4 and the mass-energy balance of the process can be written as follows:

$$\begin{aligned} M(\mathrm{Z},\,\mathrm{A})c^2 &= M(\mathrm{Z\text{-}2},\,\mathrm{A})^* c^2 + B_{2h} \\ &\hookrightarrow M(\mathrm{Z\text{-}2},\,\mathrm{A})c^2 + E_\gamma, \end{aligned} \tag{2.23}$$

where the parent nuclide M(Z, A) decays into the excited state of the nuclide with M(Z-2, A) containing two atomic holes with the corresponding energy B_{2h} and subsequently de-excites to the ground daughter state emitting a) X-rays and Auger electrons due to the relaxation of the atomic shell and b) γ-rays (carrying away the energy E_γ, respectively) in case of the transition to the nuclear excited state. The process is only possible if a single-electron capture to the intermediate nuclide with (Z-1, A) is energetically forbidden. In addition, a Q-value of the neutrinoless double-electron capture process

$$Q_{\epsilon\epsilon} = \left[M(\mathrm{Z},\,\mathrm{A}) - M(\mathrm{Z\text{-}2},\,\mathrm{A})\right] c^2 = B_{2h} + E_\gamma \tag{2.24}$$

should not exceed $2m_e c^2$ causing the occurrence of the competitive processes with emission of one and more positron(s) [74]. With the relevant isotopes (see Sec. 4.1) a detection of the concomitant de-excitation radiations in coincidence would definetely imply the occurrence of the $0\nu\epsilon\epsilon$-decay.
The neutrinoless double-electron capture was already considered by Winter in 1955 [75]. However, it was out of the scope of experimental physics since the estimated half-lives of the corresponding nuclides were much higher ($T_{1/2}^{0\nu\epsilon\epsilon} > 10^{24}$ y) than in the $0\nu\beta\beta$ case. Whereas in the double-beta decay an energy excess is carried away by two elec-

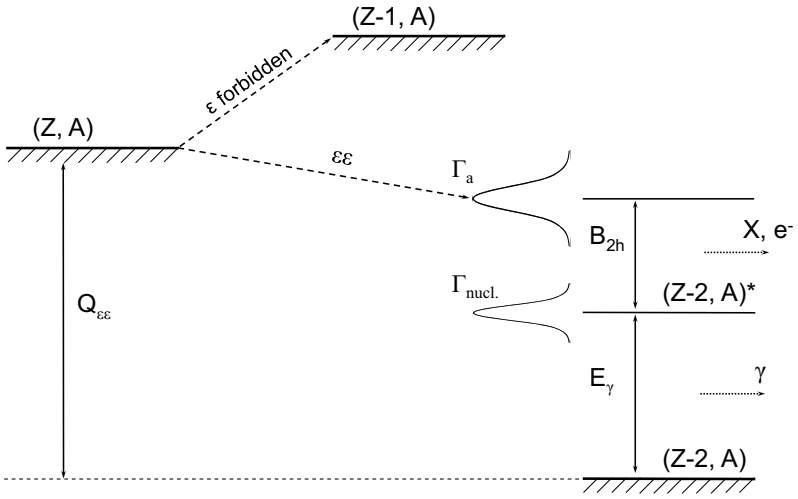

Figure 2.4: Double-electron capture energy diagram. The nuclide with (Z, A) captures two electrons $\epsilon\epsilon$ from the atomic shell with the corresponding energy B_{2h} and thus decays into the excited atomic state of the daughter nuclide (Z-2, A). Relaxation causes emission of X-rays, Auger electrons and, if the daughter nucleus is excited too, a γ-radiation with the energy E_γ. Γ_a and $\Gamma_{\text{nucl.}}$ are atomic and nuclear level widths, respectively. A transition (Z, A) $\xrightarrow{\epsilon}$ (Z-1, A) is energetically forbidden.

trons, as well as in the double-electron capture with emission of two neutrinos, in the $0\nu\epsilon\epsilon$-decay the energy and momentum conservation is not fulfilled unless some additional processes, such as, e.g., electron-positron pair creation or inner bremsstrahlung photon emission [76], are considered. These processes suppress even more the already small chance of the $0\nu\epsilon\epsilon$-decay to be observed (Eq. (2.22)), but in 1983 it was shown in [77] that the excited atomic state of the daughter nuclide with the natural width Γ_a can overlap with the initial state of the mother nuclide, giving a natural resonance condition for the probability of $0\nu\epsilon\epsilon$. Moreover, further investigations with a perturbative approach have shown [78] that in certain circumstances a radiative resonance enhancement of the order of $10^4 - 10^5$ takes place.
The probability of the neutrinoless double-electron capture can be written as [77]

$$\lambda_{0\nu\epsilon\epsilon} = \frac{\ln 2}{T_{1/2}} = \frac{(g_A G_F \cos\theta_c)^4}{(4\pi R)^2} P_{\epsilon\epsilon} |m_{\epsilon\epsilon}|^2 |M_{\epsilon\epsilon}|^2 \frac{\Gamma}{\Delta^2 + \Gamma^2/4}, \tag{2.25}$$

where g_A is the axial-vector nucleon coupling constant, G_F is the Fermi constant, θ_c is the Cabibbo angle, R is the nuclear radius, $m_{\epsilon\epsilon}$ is the effective Majorana neutrino mass (see Eq. (2.22)), $M_{\epsilon\epsilon}$ is the nuclear matrix element and $P_{\epsilon\epsilon} = |\Psi_{h1}|^2 |\Psi_{h2}|^2$ is the product of the electron wave functions of the captured electrons h_1 and h_2. The latter fraction is a so-called resonance enhancement factor

$$F = \frac{\Gamma}{\Delta^2 + \Gamma^2/4}, \tag{2.26}$$

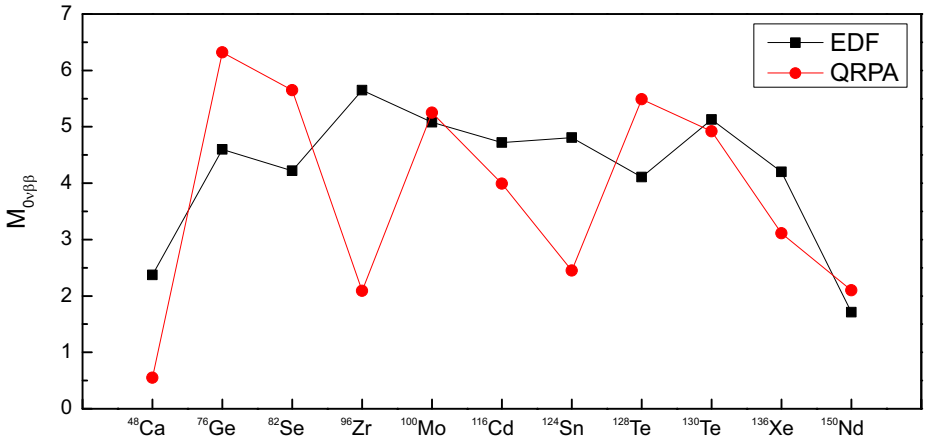

Figure 2.5: Nuclear matrix elements $M_{0\nu\beta\beta}$ of the neutrinoless double-beta transitions, calculated in [82] and [83] using the QRPA and EDF theoretical approaches, respectively.

where $\Gamma \approx \Gamma_a + \Gamma_{\text{nucl.}}$ [79] is the total width of the excited nuclear and two-hole atomic states of the daughter nuclide and Δ is the degeneracy factor for overlapping of the initial and final states of the $0\nu\epsilon\epsilon$-transition:

$$\Delta = Q_{\epsilon\epsilon} - B_{2h} - E_{\gamma}. \tag{2.27}$$

Thus the resonance enhancement factor is maximal when $\Delta = 0$, what significantly reduces the scope of the search for the appropriate isobaric pairs (see Chap. 4).
Since the calculations of the half-lives of the probable $0\nu\epsilon\epsilon$-transitions is out of the scope of the present thesis work due to the results obtained, only short notes on the calculations of the included parameters will be given in the following, while the fundamentals of the neutrinoless double-electron capture theory and its further development can be found, e.g., in [76–81].
In Eq. (2.25) the energy levels of single electron holes are known with a very high precision[6] (see, e.g., [84]), while the wave functions of the captured electrons $P_{\epsilon\epsilon}$ and the energies of the two-hole atomic states can be calculated very precisely using the modern knowledge concerning the Coulomb interactions and QED. The latter is important if the degeneracy parameter Δ is on the order of a few hundred eV, a coarse approximation $B_{2h} = B_{h1} + B_{h2}$ can be used otherwise.
The widths Γ_a of the atomic holes can be estimated simply as $\Gamma_a = \Gamma_{h1} + \Gamma_{h2}$ and the nuclear widths $\Gamma_{\text{nucl.}}$ can be neglected since they are typically much smaller than the widths of the atomic states (or in a case of the $0^+ \rightarrow 0^+$ transition, see below). In addition, the capture of K- and L-shell electrons has the largest probability due to the overlap of the electron wave functions with the nucleus.
Concerning the nuclear transitions, the most highest probability is considered in the $0^+ \rightarrow 0^+$ transitions between nuclear ground states, where emission of two neutrinos

[6] With respect to the current topic.

can be suppressed by the phase space [85]. Thus, the even-even nuclei are favorable and the calculations are more reliable. However, even in this case precise calculations of the nuclear matrix elements $M_{\epsilon\epsilon}$ cause difficulties due to the complicated nuclear structure, while typically $0\nu\epsilon\epsilon$-emitters lay in a range of medium and medium-heavy masses. Different theoretical approaches like the energy-density functional [83] (EDF) or the quasi-particle random phase approximation [82] (QRPA) give the values of the $0\nu\beta\beta$ nuclear matrix elements between $\sim$1 and 6 (see Fig. 2.5) for the ground-to-ground state transitions, which are nevertheless higher than for the transitions to the nuclear excited states (see, e.g., [86]). It should be mentioned, that the transitions to the excited states provide an additional signature as the emission of gamma-rays in coincidence with the de-excitation spectrum of the atomic shell, and the transitions to a variety of the excited states within a particular nuclide are also possible (a so-called *multiresonance phenomenon*, see Sec. 4.5).

To summarize, the neutrinoless double-electron capture can be promising for the experimental investigation of the neutrino mass and nature and competitive to the neutrinoless double-beta decay if suitable nuclides would be found. The requirements on the latter concern in general the next three points:

- The nuclide should fulfill the energy balance requirements due to the already small probability of the $0\nu\epsilon\epsilon$-decay.
- The resonance enhancement factor F given by Eq. (2.26) should be maximal, and thus the degeneracy factor Δ should be close to zero, what requires $Q_{\epsilon\epsilon} \cong B_{2h} + E_{\gamma}$.
- The nuclear ground-to-ground state transitions are favorable due to the largest value for the nuclear matrix elements, which can be reliably calculated.

The last two conditions are interrelated in a sense of the nuclear ground and excited state transitions. While the ground-to-ground state transitions are favorable because of the nuclear part of the decay probability, the multiresonance enhancement by transitions to the excited states together with an additional signature in a form of γ-emission could compensate a lack of the resonance enhancement if it is the case.
A search for the resonantly enhanced candidates has been pushed forward by the lack of precise atomic and nuclear data and by the recent progress in the double-beta decay sector. The lack of precise data on the $Q_{\epsilon\epsilon}$-values initiated a series of Penning-trap mass spectrometry experiments, where the current thesis data contribute with several $Q_{\epsilon\epsilon}$-values (Chap. 4). In case a proper nuclide will be found, the techniques already employed in a search for $0\nu\beta\beta$ (like, e.g., cryogenic micro-calorimetry) could be used to reveal the fundamental properties of these weak neutral leptons.

Chapter 3

Principles of Penning-trap mass spectrometry

Nowadays a variety of advanced cooling and detection techniques together with well-developed ion production and transportation mechanisms make Penning-trap mass spectrometry a versatile tool for a broad range of researches. Neutrino physics investigations require data on the atomic mass differences of the isobaric pairs with a 1 ppb precision and better. Since no high-precision measurements could be done without a solid theoretical foundation, the following chapter is a review of the theory of Penning traps, which covers the studies within present thesis work.

3.1 Ion motion in the ideal Penning Trap

A charged particle with charge q and mass m in a homogeneous magnetic field $\boldsymbol{B} = B_0\boldsymbol{e}_z$, directed along the z-axis, moves periodically in the xy-plane on a circular orbit under the action of the Lorentz force $\boldsymbol{F} = q[\boldsymbol{v} \times \boldsymbol{B}]$. This motion is called a *free cyclotron motion* and the frequency of the motion (a so-called *free cyclotron frequency*) is given by

$$\omega_c = \frac{q}{m}B_0. \tag{3.1}$$

In order to confine a particle in the axial direction, a quadrupole electrostatic field is applied

$$\phi(\rho, z) = C(z^2 - \frac{\rho^2}{2}) \quad \text{(in cylindrical coordinates)}, \tag{3.2}$$

$$\boldsymbol{E}(\rho, z) = -\boldsymbol{\nabla}\phi(\rho, z) = C(-2z\boldsymbol{e}_z + \rho\boldsymbol{e}_\rho), \tag{3.3}$$

where C defines the field strength. This special combination of fields $\boldsymbol{B}$ and $\boldsymbol{E}$ is named "Penning trap". The resulting equations of motion due to the Lorentz force are

$$m\ddot{\boldsymbol{r}} = q(\boldsymbol{E} + [\boldsymbol{v} \times \boldsymbol{B}]) \tag{3.4}$$

with $\boldsymbol{r}$ is given in Cartesian coordinates.
Hence, the particle is stored in the axial direction, while the free cyclotron motion

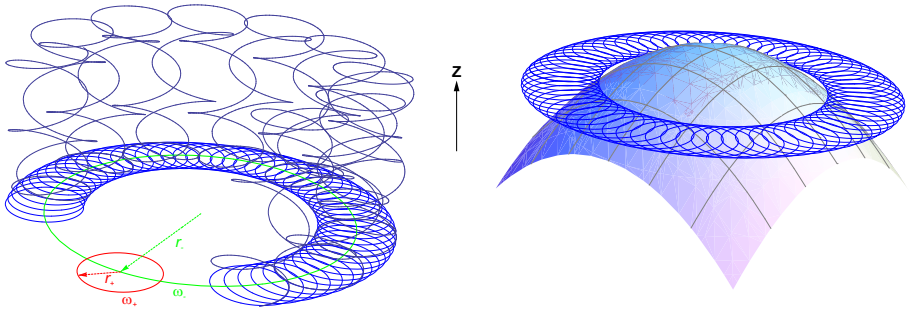

Figure 3.1: (left) An example of a three-dimensional ion motion in the Penning trap and its projection onto the radial plane. A red circle denotes the modified cyclotron orbital motion slowly drifting along the magnetron orbit (green). $r_\pm$ and $\omega_\pm$ are radii and frequencies of the motions, correspondingly. (right) A repulsive potential causing the loss of stability with an increase of the magnetron energy.

undergoes a modification into a *modified cyclotron motion* caused by the repulsive radial field component of the electrostatic potential reducing the centrifugal force, and a new mode (*magnetron motion*) appears in the radial plane due to the azimuthal $[\boldsymbol{E} \times \boldsymbol{B}]$ drift. A sketch of the resulting motion and its projection onto the radial plane are shown in Fig. 3.1 (left). The fast modified cyclotron motion with the frequency ω_+ (red circle on a plane) slowly drifts along the orbit of the magnetron motion (green) with the frequency ω_-, while in the axial direction the particle simply oscillates with the frequency ω_z (a so-called *axial motion*). All three motions are considered as three independent harmonic oscillators with respective eigenfrequencies

$$\omega_+ = \frac{\omega_c}{2} + \frac{1}{2}\sqrt{\omega_c^2 - 2\omega_z^2}, \tag{3.5a}$$

$$\omega_- = \frac{\omega_c}{2} - \frac{1}{2}\sqrt{\omega_c^2 - 2\omega_z^2}, \tag{3.5b}$$

$$\omega_z = \sqrt{C\frac{q}{m}}. \tag{3.5c}$$

The frequencies $\omega_\pm$ and ω_z are the observables in Penning-trap experiments and the free cyclotron frequency is the main measurand in the mass measurements due to its plain dependence on the mass of the particle and the stability of the magnetic field over the stability of the electric field. The ideal Penning trap holds the following relations between the frequencies:

$$\omega_c = \omega_+ + \omega_-, \tag{3.6}$$

$$\omega_z^2 = 2\omega_+\omega_-. \tag{3.7}$$

From Eq. (3.5b) and Eq. (3.5c) the magnetron frequency ω_- in first order approximation

does not depend on particle properties

$$\omega_- \approx \frac{C}{2B_0}, \tag{3.8}$$

what together with Eq. (3.6) gives a solid relation between the free and modified cyclotron frequency. This is advantageous in, e.g., the ToF-ICR or PI-ICR mass ratio measurements at SHIPTRAP (see Chap. 4 and Chap. 5).
However, in the presence of trap imperfections of the real trap these two equations are weakened, while the so-called invariance theorem [87] stays unaffected

$$\omega_c^2 = \omega_+^2 + \omega_-^2 + \omega_z^2, \tag{3.9}$$

what is a key point of the ultra-high precision Penning-trap experiments like PENTATRAP (Chap. 6) or the FSU-TRAP [73] employing the axial frequency based detection techniques (Sec. 6.1.4).
Stability of the particle confinement follows from the requirement to the expressions under the radicals in Eq. (3.5) to be real. This yields the following conditions

$$\omega_c > \sqrt{2}\omega_z \quad \Leftrightarrow \quad \sqrt{\frac{q}{m}} > 2\sqrt{\frac{C}{B_0^2}}, \tag{3.10}$$

$$qC > 0. \tag{3.11}$$

The first condition represents the fact that the nature of the radial component of the electrostatic field is repulsive and thus should be smaller than the strength of the magnetic field. The second condition defines a sign of the electrostatic potential in order to provide a minimum in the axial direction with respect to a sign of the charged particle. A typical field configuration of the Penning trap, in which the magnetic field is much stronger than the electrostatic field, together with the charges and masses of the trapped ions cause the eigenfrequencies to follow the hierarchy

$$\omega_c > \omega_+ \gg \omega_z \gg \omega_-. \tag{3.12}$$

The meaning of the frequency hierarchy can be seen from the energies of the corresponding eigenmotions [87]

$$E_+ = \frac{m}{2}\omega_+^2\rho_+^2 - \frac{m}{4}\omega_z^2\rho_+^2, \tag{3.13a}$$

$$E_- = \frac{m}{2}\omega_-^2\rho_-^2 - \frac{m}{4}\omega_z^2\rho_-^2, \tag{3.13b}$$

$$E_z = \frac{m}{2}z_0^2\omega_z^2, \tag{3.13c}$$

where z_0 and $\rho_\pm$ are the amplitudes of the eigenmotions. Thus, the energy of the axial motion oscillates between potential and kinetic energy. The energy of the modified cyclotron motion is almost purely kinetic due to $\omega_+ \gg \omega_z$, while the energy of the

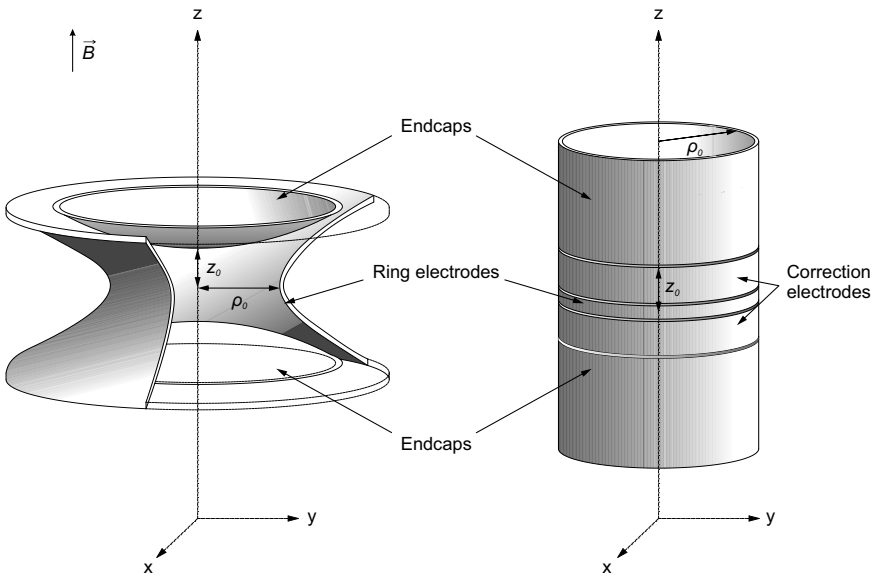

Figure 3.2: A sketch of a hyperboloidal (left) and a cylindrical Penning trap (right). For details see text.

magnetron motion is mostly potential because of $\omega_z \gg \omega_-$. The latter results in a repulsive "metastable" character of the magnetron eigenmotion (see Fig. 3.1 (right)): with an increase of the magnetron radius its kinetic energy increases slightly whereas potential energy decreases significantly (the particle "slips" down the radial potential hill).

3.2 Systematics of the real Penning Trap

Unlike the idealized picture given in the previous section, the Penning trap in the laboratory is a complicated system with many degrees of freedom. In order to obtain the high-precision results on the free cyclotron frequency measurements it is obligatory to investigate and, if possible, exclude all the systematic effects leading to the shifts in the frequency determination. These shifts arise among others from the non-ideal configuration of the E- and B-fields, electrostatics and electrodynamics of the trapped particles.

Typically, the core of the trap is a strong superconducting magnet with $B_0 = 7$ T (as an example of the SHIPTRAP and PENTATRAP magnetic fields) and a homogeneous region in its center. The quadrupolar electrostatic potential can be produced by electrodes with a shape following the field lines of Eq. (3.3) (see Fig. 3.2 (left)). There a central electrode is called "the ring" and upper and lower electrodes are called "the endcaps". A close to the harmonic potential can be created also by the cylindrical configuration involving two additional correction electrodes (Fig. 3.2 (right)). This configuration is more often in use due to an easier machining and an open access to

the trap. The characteristic dimension of the trap is given by $d^2 = 1/2(z_0^2 + \rho_0^2/2)$ and thus the constant C in Eq. (3.5c) is turned to $C = U_0/d^2$ giving the commonly used relation

$$\omega_z = \sqrt{\frac{q}{m}\frac{U_0}{d^2}}. \tag{3.14}$$

Here U_0 denotes the voltage difference applied between the ring and the endcaps.

3.2.1 Electrostatic imperfections

Due to the finite geometry of the trap electrodes and machining imperfections the electrical field is only close to the ideal one, especially in the case of the cylindrical trap. This leads to the anharmonicities in the motion of the ion. Effectively they are described by the real electrostatic potential given as a solution of the Laplace equation $\Delta\phi(\rho, z) = 0$ around the trap centre with the boundary conditions defined by the potentials applied to the trap electrodes

$$\phi(\rho, z) = U_0 \sum_{j=0}^{\infty} c_j (\rho^2 + z^2)^{j/2} P_j\left(\frac{z}{\sqrt{\rho^2 + z^2}}\right), \tag{3.15}$$

where P_j are the Legendre polynomials and the coefficients c_j are pure functions of the electrode geometry and the applied voltages. These coefficients, calculated for a five-pole cylindrical trap in [88], define the anharmonicity of the potential, what can be clearly seen from the Taylor expansion:

$$\begin{aligned} \phi(\rho, z)/U_0 = \; & c_0 \\ & + c_2 \left(z^2 - \frac{1}{2}\rho^2 \right) \\ & + c_4 \left(z^4 - 3\rho^2 z^2 + \frac{3}{8}\rho^4 \right) \\ & + c_6 \left(z^6 - \frac{15}{2}\rho^2 z^4 + \frac{45}{8}\rho^4 z^2 - \frac{5}{16}\rho^6 \right) \\ & + \ldots \; . \end{aligned} \tag{3.16}$$

where odd terms vanishes due to the $z \to -z$ symmetry. Hence, the c_2 coefficient defines the strength of the electric field and Eq. (3.14) can be written as

$$\omega_z = \sqrt{\frac{q}{m} 2 c_2 U_0}. \tag{3.17}$$

In order to minimize the influence of the higher order terms one can consider the following suggestions from [87]: if the symmetric voltages U_{CE} applied to the correction

Table 3.1: Approximate frequencies of $^{133}Cs^+$ and $^{85}Rb^+$ ions specific for the SHIPTRAP Penning trap mass spectrometer.

Eigenfrequency[1]	$^{133}Cs^+$	$^{85}Rb^+$
ν_-/Hz	1322	1321
ν_z/Hz	46221	57826
ν_+/Hz	808005	1265455
ν_c/Hz	809327	1266776

electrodes and the endcaps are grounded, coefficients can be rewritten in a from

$$c_j = e_j + \mathrm{TR} \cdot d_j, \tag{3.18}$$

where coefficients e_j and d_j ideally depends on the geometry of the trap, and $TR = U_{CE}/U_0$ is a so-called *tuning ratio*. Thus, the ratio can be chosen in a way that c_4 and c_6 vanish at the same time and the trap is then called *compensated*. If d_2 vanishes, c_2 and thus ω_z (see Eq. (3.17)) do not depend on the TR anymore, what is called *orthogonality*. The trap can be made orthogonal if proper geometry is found.
Nevertheless, high-precision measurements require to estimate the influence of the anharmonic potential to the eigenfrequencies. This can be done by solving the equations of motion (Eq. (3.4)) with the potential given in Eq. (3.16) (see discussion in [89]) or by the perturbative approach, as shown in [87, 90]. For c_4 and c_6 the axial frequency shift is given by

$$\frac{\Delta\omega_z}{\omega_z} = \frac{3}{4}\left(\frac{c_4}{c_2^2} + \frac{5}{4}\frac{c_6}{c_2^3}\frac{E_z}{qU_0}\right)\frac{E_z}{qU_0}, \tag{3.19}$$

and for the leading coefficient c_4 the shifts of all the frequencies are

$$\begin{pmatrix}\Delta\omega_+/\omega_+\\ \Delta\omega_z/\omega_z\\ \Delta\omega_-/\omega_-\end{pmatrix} = \frac{3}{qU_0}\frac{c_4}{c_2^2}\begin{pmatrix}\frac{1}{4}(\omega_z/\omega_+)^4 & -\frac{1}{2}(\omega_z/\omega_+)^2 & -(\omega_z/\omega_+)^2\\ -\frac{1}{2}(\omega_z/\omega_+)^2 & \frac{1}{4} & 1\\ -(\omega_z/\omega_+)^2 & 1 & 1\end{pmatrix}\begin{pmatrix}E_+\\ E_z\\ E_-\end{pmatrix}. \tag{3.20}$$

The total effect of all the shifts on the free cyclotron frequency is then given by its relative uncertainty

$$\frac{\Delta\omega_c}{\omega_c} = \sqrt{\left(\frac{\omega_+}{\omega_c^2}\Delta\omega_+\right)^2 + \left(\frac{\omega_z}{\omega_c^2}\Delta\omega_z\right)^2 + \left(\frac{\omega_-}{\omega_c^2}\Delta\omega_-\right)^2}, \tag{3.21}$$

[1] Frequencies are given by definition $\omega = 2\pi\nu$ of the angular frequency.

which is derived from the invariance theorem, see Eq. (3.9). Thus, e.g., the frequencies of the $^{133}Cs^+$ and $^{85}Rb^+$ ions specific for the SHIPTRAP mass spectrometer are given in Tab. 3.1. It can be seen, that the relative contributions of the axial and magnetron modes are strongly suppressed with respect to the modified cyclotron frequency, which hence is dominant in the free cyclotron frequency determination.

3.2.2 Imperfections of the magnetic field

Similarly to the electric field anharmonicities, the inhomogeneities of the magnetic field can be found from the Laplace equation followed from the Gauss's law $(\boldsymbol{\nabla} \cdot \boldsymbol{B}) = 0$. Since $[\boldsymbol{\nabla} \times \boldsymbol{B}] = 0$, the magnetic field can be defined from a scalar potential $\boldsymbol{B} = -\boldsymbol{\nabla}\psi$ leading to the equation $\Delta\psi = 0$. The solutions around the trap centre are given in cylindrical coordinates as follows

$$\psi(\rho, z) = -\sum_{j=0}^{\infty} \frac{b_j}{j+1} (\rho^2 + z^2)^{\frac{j+1}{2}} P_j(\frac{z}{\sqrt{\rho^2 + z^2}}). \tag{3.22}$$

Since the Laplace equation has no mixed derivatives, the radial and axial components can be uncoupled. Taking the gradient of the magnetic potential, the axial $\boldsymbol{B}^{(z)}(\rho, z)$ and radial $\boldsymbol{B}^{(\rho)}(\rho, z)$ magnetic field components are written [91]

$$\boldsymbol{B}^{(z)}(\rho, z) = \sum_{j=0}^{\infty} b_j \sum_{k=0}^{\lfloor \frac{j}{2} \rfloor} \frac{(-1)^k}{2^{2k}} \frac{j!}{(j-2k)!(k!)^2} z^{j-2k} \rho^{2k}, \tag{3.23}$$

$$\boldsymbol{B}^{(\rho)}(\rho, z) = \sum_{j=1}^{\infty} b_j \sum_{k=1}^{\lfloor \frac{j+1}{2} \rfloor} \frac{(-1)^k k}{2^{2k-1}} \frac{j!}{(j-2k+1)!(k!)^2} z^{j-2k+1} \rho^{2k-1}. \tag{3.24}$$

Usually the higher orders of the magnetic field inhomogeneities can be neglected. Thus the magnetic field can be expanded up to the second order as

$$\boldsymbol{B}(\rho, z) = b_0 \boldsymbol{e}_z + b_1 \left(z\boldsymbol{e}_z - \frac{\rho}{2}\boldsymbol{e}_\rho \right) + b_2 \left(\left(z^2 - \frac{\rho^2}{2} \right) \boldsymbol{e}_z - z\rho \boldsymbol{e}_\rho \right). \tag{3.25}$$

First, omitting b_1, the higher order terms cause the dependence of the eigenfrequencies on the radial amplitude ρ or, what is the same, on the energy, see Eq. (3.13). Due to the relations $\omega_+ \approx \omega_c \sim B$ and $\omega_- \sim B^{-1}$ the effect is clear, while for the axial frequency it is not so obvious. The ion orbiting in the radial plane is simply a current perpendicular to the magnetic field lines. For the modified cyclotron motion this leads to a force

$$F_2^{(z)} = \frac{\partial}{\partial z}(\mu_+ B^{(z)}) = -q\omega_+ \rho_+^2 b_2 z \tag{3.26}$$

acting on the magnetic moment of the ion $\boldsymbol{\mu} = -q\frac{\omega_+\rho_+^2}{2}\boldsymbol{e}_z$ in the axial direction. The shifts of all three eigenfrequencies with respect to the b_2 term are given by

$$\begin{pmatrix} \Delta\omega_+/\omega_+ \\ \Delta\omega_z/\omega_z \\ \Delta\omega_-/\omega_- \end{pmatrix} = \frac{1}{m\omega_z^2}\frac{B_2}{B_0}\begin{pmatrix} -(\omega_z/\omega_+)^2 & 1 & 2 \\ 1 & 0 & -1 \\ 2 & -1 & -2 \end{pmatrix}\begin{pmatrix} E_+ \\ E_z \\ E_- \end{pmatrix}. \tag{3.27}$$

Considering now the b_1 term, the radial motions do not feel this shift of the B-field. The shift of the radial frequencies is caused by the shift of the "equilibrium" point of the axial oscillation due to the force $F_1^{(z)} = -q\omega_+\rho_+^2 b_1$. The radial modes feel a shifted magnetic field. However, this shift is negligible compared to the influence of b_2.

3.2.3 Voltage drifts

Fluctuations of the voltage source can be split in two groups with respect to the measurement time. *Fast* fluctuations in principle can be neglected since they are averaged out during the measurement and do not lead to the visible frequency shifts. However, a *slow* voltage drift on a time scale comparable with the measurement time can result in shifts due to the dependence of the axial and magnetron frequencies on the electric field strength.
The relative magnetron frequency shift is given by

$$\frac{\Delta\omega_-}{\omega_-} = \frac{\Delta U_0}{U_0}. \tag{3.28}$$

With the damping factor in Eq. (3.21) of the relative contribution to the determination of the free cyclotron frequency by means of the invariance theorem (Eq. (3.9)) it can be neglected. However, the systematic studies of the novel PI-ICR technique showed that the voltage drift might cause drift of the modified cyclotron frequency of about a few tens of mHz for $^{133}Cs^+$ according to the SHIPTRAP setup at the moment when the studies were performed (see Sec. 5.3.3).
The axial frequency shift due to the drift of the trap voltage is given by

$$\frac{\Delta\omega_z}{\omega_z} = \frac{1}{2}\frac{\Delta U_0}{U_0}. \tag{3.29}$$

The determination of the free cyclotron motion via the invariance theorem on the precision level of better than 10^{-11} requires a determination of the axial frequency on the level of about 10^{-8} and thus the same level of stability of the voltage source (see Sec. 6.1) over the measurement time.

3.2.4 Fluctuations of the magnetic field and the mass ratio determination

In order to discuss the influence of the magnetic field fluctuations, it is convenient to introduce a mass ratio measurement principle. Since absolute values of the magnetic fields are usually not known at the level required by the cyclotron frequency determination, and, in addition, the charge of the ion, which is an integer number multiplied by the elementary charge, is known today with the relative uncertainty of about 2×10^{-8} [92], the determination of the mass ratios is necessary for high-precision measurements. Assuming equally charged ions with masses m_1 and m_2, the mass ratio can be determined as follows

$$\frac{m_1}{m_2} = \frac{B(t_1)}{B(t_2)} \frac{\omega_{\mathrm{c}}^{(2)}(t_2)}{\omega_{\mathrm{c}}^{(1)}(t_1)}. \tag{3.30}$$

If the knowledge on the absolute mass of a certain nuclide is obligatory for a specific application, the mass ratio measurements can be considered as a calibration of the Penning-trap spectrometer. It is then convenient to use clusters of ^{12}C since it conventionally defines the atomic mass unit.
Under these circumstances, the fluctuations of the magnetic field have to be estimated if it is technically not possible to measure two cyclotron frequencies at the same time[2]. A shift in the mass ratio determination is given by

$$\Delta\left(\frac{m_1}{m_2}\right) = \frac{\Delta B}{\overline{B}} \frac{\omega_{\mathrm{c}}^{(2)}(t_2)}{\omega_{\mathrm{c}}^{(1)}(t_1)}, \tag{3.31}$$

where $\Delta B = B(t_1) - B(t_2)$ is the magnetic field drift and $\overline{B}$ is the arithmetic mean of $B(t_1)$ and $B(t_2)$. This shift might be significant and usually a lot of efforts is invested into the stabilization of the magnetic field. Moreover, different technical approaches have been developed in order to minimize the influence of the drift, as discussed in Chap. 5 and Chap. 4.

[2] While in the case of a simultaneous measurement of both frequencies the magnetic field terms in Eq. (3.30) are simply truncated.

Chapter 4

Q-value measurements at SHIPTRAP

4.1 Neutrinoless double-electron capture and Q-values

As it is pointed out in Sec. 2.4.2, the probability of a neutrinoless double-electron capture transition (see Eq. (2.25)) can be resonantly enhanced if the degeneracy parameter Δ vanishes and thus the enhancement factor F becomes maximal:

$$F = \frac{\Gamma}{\Delta^2 + \Gamma^2/4} \rightarrow \frac{4}{\Gamma} \quad \Leftrightarrow \quad \Delta = Q_{\epsilon\epsilon} - B_{2h} - E_\gamma \rightarrow 0. \tag{4.1}$$

In this case the resonantly enhanced transition rates of $0\nu\epsilon\epsilon$ could be comparable to the transition rates of the neutrinoless double-beta decay, meanwhile comprising some certain advantages like the absence of a strong background from two-neutrino mode or the possibility of multiple decays to the nuclear excited states, what is much less probable for the $0\nu\beta\beta$-transitions [93].
In order to find suitable candidates, which could be employed in the $0\nu\epsilon\epsilon$-experiments, one has to investigate all parameters in Eq. (2.25). This was done, e.g., in [79], where the authors provided a list of possible candidates and concluded that the lower bound on the corresponding half-lives normalized to the Majorana neutrino mass $|m_{\beta\beta}| = 1$ eV is $\sim 10^{22}$ y, which is about a factor of 100 or 1000 below lifetimes predicted for $0\nu\beta\beta$-transitions. The dominating error in their predictions was coming from the uncertainty of mass differences $Q_{\epsilon\epsilon}$, estimated from "The 2003 Atomic Mass Evaluation" [94].
Under these circumstances and with the development of Penning-trap mass spectrometry, a search for resonantly enhanced $0\nu\epsilon\epsilon$-transitions has been started implying the measurements of the $Q_{\epsilon\epsilon}$-values with a very high absolute uncertainty of a few hundreds eV. According to the proposed lists of probable $0\nu\epsilon\epsilon$-transitions (see, e.g., [79, 96, 97]), the search was narrowed down to about 16 known isobaric pairs. A list of the preliminarily estimated degeneracy parameters of the isobaric pairs probed with Penning traps is given in Tab. 4.1. Here the first three are the ground-to-ground state transitions, which were supposed to be the most promising due to the largest value for the nuclear matrix elements and the advantageous phase-space factor. The next group comprises the transitions, for which the $Q_{\epsilon\epsilon}$-value measurements were performed with

Table 4.1: Estimated parameters of the neutrinoless double-electron capture transitions. E_γ and I_f^π are the energy and spin/parity of the final nuclear excited state (equals to 0 keV and 0^+ for the ground states, respectively) [95]. $B_{2h} = B_{h1} + B_{h2}$ is a coarse estimate of the energy of the two-hole atomic state based on the electron binding energies given in [84] (here the uncertainties are neglected). Column 4 indicates electron orbitals. $Q_{\epsilon\epsilon}$ is the mass difference of corresponding isobars taken from [94]. Δ is the degeneracy parameter.

Transition	E_γ (keV)	I_f^π	Orbitals	B_{2h} (keV)	$Q_{\epsilon\epsilon}$ (keV)	Δ (keV)
^{152}Gd $\rightarrow$ ^{152}Sm		0^+	KL_1	54.57	54.6(35)	0.03(350)
^{164}Er $\rightarrow$ ^{164}Dy		0^+	L_1L_1	18.09	23.3(39)	5.21(390)
^{180}W $\rightarrow$ ^{180}Hf		0^+	KK	130.70	144.4(45)	13.7(45)
^{102}Pd $\rightarrow$ ^{102}Ru	1103.047(13)	2^+	KL_3	24.96	1173.0(36)	45.0(36)
^{106}Cd $\rightarrow$ ^{106}Pd	2705.30(8)	1^+	KL_1	27.95	2770.0(72)	36.8(72)
	2713.89(8)	$(2,3)^+$	KL_3	27.52		28.6(72)
	2748.2(4)	$(2,3)^-$	KL_3	27.52		-5.7(72)
^{144}Sm $\rightarrow$ ^{144}Nd	1560.92(13)	2^+	KL_3	49.78	1781.2(18)	170.5(18)
^{156}Dy $\rightarrow$ ^{156}Gd	1946.375(6)	1^-	KL_1	58.61	2012.2(74)	7.2(74)
	1952.385(7)	0^-	KM_1	52.12		7.7(74)
	1988.5(2)	0^+	L_1L_1	16.75		6.9(74)
	2003.749(5)	2^+	M_1N_3	2.17		6.3(74)

the Penning-trap mass spectrometer SHIPTRAP within the present thesis work, and the results are presented in the end of this chapter.

4.2 Mass ratios and the Q-value determination

The $Q_{\epsilon\epsilon}$-value of the double-electron capture transition is the mass difference of the initial and final states of the corresponding nuclides

$$Q_{\epsilon\epsilon} = M_i - M_f, \tag{4.2}$$

where M_i and M_f are the atomic masses of parent and daughter nuclides, respectively. Employing Penning-trap mass spectrometry, the mass of the corresponding ion can be determined by the measurement of its free cyclotron frequency ν_c defined by Eq. (3.1). For a singly charged nuclide the mass of the ion is given by

$$M^+_{i,f} = M_{i,f} - m_e + B_{i,f}, \tag{4.3}$$

where m_e is the mass of the electron and $B_{i,f}$ its binding energy. Introducing a mass (or a frequency) ratio[1]

$$R = \frac{M^+_i}{M^+_f} = \frac{\nu^f_c}{\nu^i_c}, \tag{4.4}$$

the mass difference can be expressed as

$$Q_{\epsilon\epsilon} = (M_f - m_e)(R-1) + RB_f - B_i. \tag{4.5}$$

Since the binding energy differences for the last electrons in the atomic shells of nuclides from Tab. 4.1 are in the order of a few eV [98], they can be neglected and Eq. (4.6) reduces to

$$Q_{\epsilon\epsilon} = (M_f - m_e)(R-1). \tag{4.6}$$

Thus, a determination of the $Q_{\epsilon\epsilon}$-value of the $0\nu\epsilon\epsilon$-transition reduces to a measurement of the mass or frequency ratio R with the corresponding uncertainties δM_f and δR. The resulting relative uncertainty of $Q_{\epsilon\epsilon}$ is given by

$$\frac{\delta Q_{\epsilon\epsilon}}{Q_{\epsilon\epsilon}} = \sqrt{\left(\frac{\delta M_f}{M_f - m_e}\right)^2 + \left(\frac{\delta m_e}{M_f - m_e}\right)^2 + \left(\frac{\delta R}{R-1}\right)^2}. \tag{4.7}$$

In order to significantly improve data from Tab. 4.1, the $Q_{\epsilon\epsilon}$-values have to be determined with an absolute uncertainty of about a few 100 eV, at least. For the isobaric pairs investigated in the present thesis this results in relative uncertainties of $\sim 10^{-4} - 10^{-5}$, while $R-1$ is in the order of a few parts in 10^{-5}. Since the electron mass and the atomic masses are known with relative uncertainties of about 4×10^{-10} [99] and a few 10^{-8}, respectively, the first two terms under the radical in Eq. (4.6) can be omitted, and the measurement of the mass ratio R with a relative uncertainty of about 1 ppb and better is required.

[1] Here the magnetic field is omitted (see Eq. (3.30) in Sec. 3.2.4).

4.2.1 Alternating frequency measurements

In general, a determination of the mass ratio requires the measurement of two cyclotron frequencies simultaneously in relation to the magnetic field drifts. This was done, e.g., by Pritchard *et al.* [100] with a relative uncertainty below 10^{-11}. Another way to provide a determination of R is to measure cyclotron frequencies alternately. For this some considerations have to be presented in order to take the magnetic field fluctuations into account (see also Sec. 3.2.4).
Let us consider a series of frequency measurements of two ion species as shown in Fig. 4.1, where mother and daughter nuclides are swapped in every next measurement. At time t_k the frequency of a daughter nuclide $\nu_c^f(t_k)$ is measured directly, while a value of the frequency of a mother nuclide $\tilde{\nu}_c^i(t_k)$ is obtained by linear interpolation between adjacent measured values $\nu_c^i(t_{k-1})$ and $\nu_c^i(t_{k+1})$:

$$\tilde{\nu}_c^i(t_k) = \frac{t_{k+1} - t_k}{t_{k+1} - t_{k-1}} \nu_c^i(t_{k-1}) + \frac{t_k - t_{k-1}}{t_{k+1} - t_{k-1}} \nu_c^i(t_{k+1}). \tag{4.8}$$

Thus, the frequency ratio $R(t_k)$ is determined at time t_k as

$$R(t_k) = \frac{\nu_c^f(t_k)}{\tilde{\nu}_c^i(t_k)} \tag{4.9}$$

with a relative uncertainty

$$\frac{\delta R}{R}(t_k) = \sqrt{\left(\frac{\delta \nu_c^f(t_k)}{\nu_c^f(t_k)}\right)^2 + \left(\frac{\delta \tilde{\nu}_c^i(t_k)}{\tilde{\nu}_c^i(t_k)}\right)^2}\,. \tag{4.10}$$

An uncertainty of the expected frequency $\delta\tilde{\nu}_c^i(t_k)$ depends on the uncertainties of the interpolated frequencies $\delta\nu_c^i(t_{k-1})$ and $\delta\nu_c^i(t_{k+1})$, which in turn depend on the magnetic field fluctuations. If time intervals are chosen to be shorter than the long-term drift of the magnetic field, linear interpolation meets the equivalence of the frequency and mass ratios and an error of the expected frequency can be written simply as

$$\delta\tilde{\nu}_c^{i,\mathrm{lin}}(t_k) = \sqrt{\left(\frac{t_{k+1} - t_k}{t_{k+1} - t_{k-1}}\right)^2 (\delta\nu_c^i(t_{k-1}))^2 + \left(\frac{t_k - t_{k-1}}{t_{k+1} - t_{k-1}}\right)^2 (\delta\nu_c^i(t_{k+1}))^2}\,. \tag{4.11}$$

In case of fast nonlinear fluctuations this method is not reliable anymore and nonlinear corrections (which are usually not known) have to be included:

$$\delta\tilde{\nu}_c^i(t_k) = \sqrt{\left(\frac{\delta\tilde{\nu}_c^{i,\mathrm{lin}}(t_k)}{\tilde{\nu}_c^i(t_k)}\right)^2 + \left(\frac{\delta\nu_c^{i,\mathrm{nonl}}}{\nu_c^i}\right)^2}\,. \tag{4.12}$$

By using a polynomial interpolation method one can avoid nonlinear problems (see a discussion in Sec. 4.4.3).

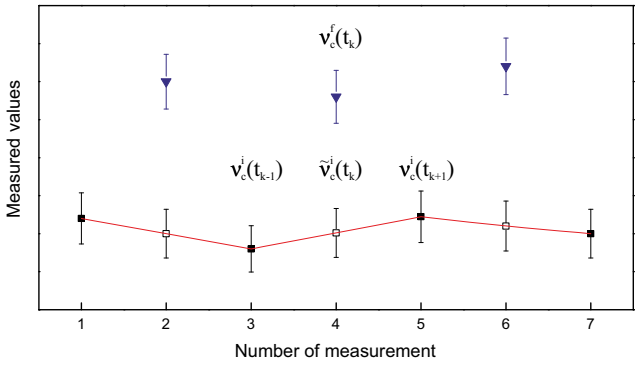

Figure 4.1: Schematic principle of a determination of a frequency ratio. The black filled squares and blue triangles correspond to the measured values of the frequencies of mother and daughter nuclides, respectively. Empty squares denote expected values of the frequencies of a mother nuclide at the time, when the measurements on the daughter nuclide are proceeding. The red lines show the result of linear interpolation between two adjacent measurements of one ion species. For details see text.

4.3 Ion manipulation and detection

In order to perform high-precision mass ratio measurements with Penning traps, a precise control over the ion cloud purity and the ion motion as well as the utilization of advanced frequency measurement techniques are of great importance. A short description of the techniques used for a determination of the Q-values at SHIPTRAP is presented below.

4.3.1 Dipolar excitation

Any of the eigenmotions in a Penning trap can be controlled individually by applying an external radiofrequency (rf) field to a trap (a *dipolar* excitation) with the corresponding eigenfrequency of the ion motion [101], what leads to an additional force in the equations of motion (Eq. (3.4))

$$q\boldsymbol{E}^i_{\mathrm{rf}}(t) = qk^{(d)}V_{\mathrm{rf}}\cos\left(\omega_{\mathrm{rf}}t + \phi_{\mathrm{rf}}\right)\cdot x_i\boldsymbol{e}_i, \tag{4.13}$$

where V_{rf}, ω_{rf} and ϕ_{rf} are the amplitude, frequency and phase of the excitation, $x_i\boldsymbol{e_i}$ denotes a coordinate for the desired direction and k is a constant, which describes a strength of a dipolar component of the rf-field due to the geometry of the trap. The result of a dipolar excitation of the eigenmotion is a nearly linear increase or decrease of its amplitude during the excitation time T_{rf}. Hence, applying the rf-field between the endcaps with $\omega_{\mathrm{rf}} = \omega_z$, the axial amplitude changes, while the radial amplitudes stay unaffected, and *vice versa*, i.e., to excite the radial modes the rf-field has to be applied across the ring electrode, which has to be split for this purpose. Typically a radial dipolar excitation is used in order to prepare ions at a certain motional radius.

4.3.2 Quadrupolar excitation

Quadrupolar excitation is used to excite the ion motion at the so-called *sidebands* – sums or differences of the eigenfrequencies – by introducing an external quadrupolar rf-field into the trap. This can be done, e.g., by applying rf-amplitudes to four segments of a split ring electrode, phase shifted with 180° for every second electrode, with the sideband frequency $\omega_{\mathrm{rf}} = \omega_+ + \omega_-$. This results in a coupling of two radial motions. The coupling of the axial mode to either of the radial modes is considered in [102] and is mentioned in Sec. 6.1.4 within the PENTATRAP cooling and detection principles.
In [103, 104] the radial coupling of the eigenmotions is described by introducing complex oscillators $\alpha_\pm(t) = |\alpha_\pm(t)| \cdot \exp(\mp i\phi_\pm(t))$, which represent the modified cyclotron and magnetron motions. In this approach the radii of the motions can be expressed as

$$r_\pm(t) = \sqrt{\frac{2\hbar}{m\left(\omega_+ - \omega_-\right)}} \cdot |\alpha_\pm| \,. \tag{4.14}$$

Interaction with an external quadrupolar rf-field leads to the complex amplitudes

$$\begin{aligned}\alpha_\pm(t) = &\exp\left[\mp i\left(\omega_\pm + \frac{\delta}{2}\right)t\right] \\ &\times\left[\left(\cos\frac{\omega_R t}{2} \pm i\frac{\delta}{\omega_R}\sin\frac{\omega_R t}{2}\right)\alpha_\pm(0) - i\frac{2g}{\omega_R}\sin\frac{\omega_R t}{2}\exp(\mp i\phi_{\mathrm{rf}})\alpha_\mp(0)\right],\end{aligned} \tag{4.15}$$

where $\delta = \omega_{\mathrm{rf}} - \omega_c$ is the detuning of the quadrupolar rf-field, $\omega_R = \sqrt{4g^2 + \delta^2}$ is the *Rabi* frequency and g is the coupling factor given by

$$g = \frac{q}{m} \cdot \frac{1}{\omega_+ - \omega_-} \cdot \frac{V_{\mathrm{rf}}}{2d^2} \,. \tag{4.16}$$

Here the main interest is the fractions of oscillator quanta in the modified cyclotron and magnetron oscillators given by

$$n_\pm(t) = \frac{|\alpha_\pm(t)|^2}{|\alpha_+(0)|^2 + |\alpha_-(0)|^2} = \frac{r_\pm^2(t)}{r_+^2(0) + r_-^2(0)}, \tag{4.17}$$

with $n_+(t) + n_-(t) = 1$ and initial values

$$n_\pm(0) = \frac{r_\pm^2(0)}{r_+^2(0) + r_-^2(0)} \,. \tag{4.18}$$

It can be seen now that a resulting time evolution of a coupled motion is an interconversion with the beating frequency $\omega_R/2$ between two radii (or two energies) of the motions.
Typically a quadrupolar excitation is applied in a form of one or more PWM (pulse-width modulated) rectangular rf-signals. Assuming that initially the ion performs a pure magnetron motion with a radius $r_-(0)$ and $r_+(0) = 0$, the time needed for one

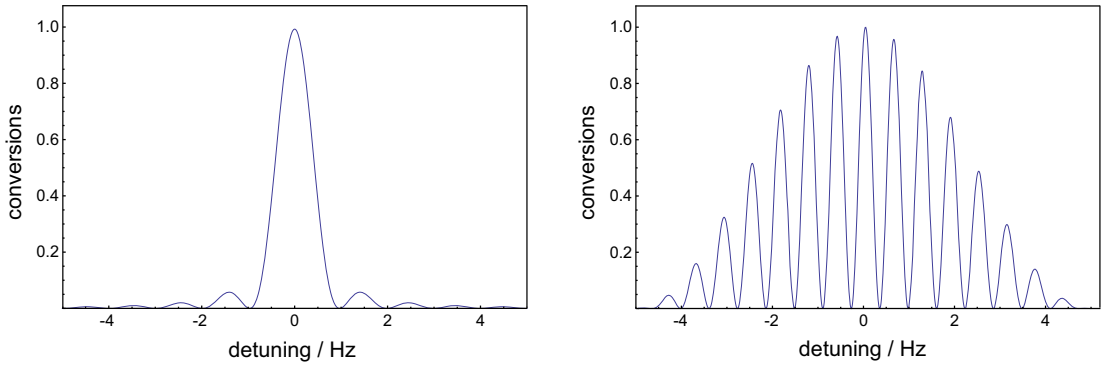

Figure 4.2: Exemplary modified cyclotron radius fractions as functions of detuning δ after a one-pulse quadrupolar excitation during the time $T_{\mathrm{rf}} = \pi/\omega_R$ (left) and a two-pulse excitation (right), where two pulses of a length $\tau_1 = \pi/(2\omega_R)$ are separated with time τ_0, resulting in the total excitation time $T_{\mathrm{rf}} = \tau_0 + 2\tau_1$.

full conversion from the magnetron to the modified cyclotron motion is defined by $T_{\mathrm{rf}} = \pi/\omega_R$. In case of a one-pulse excitation the fraction of a conversion can be expressed as

$$\frac{r_+^2(T_{\mathrm{rf}})}{r_-^2(0)} = \frac{4g^2}{\omega_R^2}\sin^2\frac{\omega_R t}{2}. \tag{4.19}$$

In Fig. 4.2 (left) a cyclotron radius fraction is plotted as a function of the detuning parameter δ. If two excitation pulses of a width $\tau_1 = \pi/(2\omega_R)$ separated by a waiting interval of duration τ_0 are applied (known as *Ramsey* method [105, 106]), then the fraction of a total conversion is given by [103, 107]

$$\frac{r_+^2(T_{\mathrm{rf}})}{r_-^2(0)} = \frac{4g^2}{\omega_R^2}\left[\cos\frac{\delta\tau_0}{2}\sin\omega_R\tau_1 + \frac{\delta}{\omega_R}\sin\frac{\delta\tau_0}{2}(\cos\omega_R\tau_1 - 1)\right]^2. \tag{4.20}$$

A plot of the fraction after a two-pulse excitation is shown in Fig. 4.2 (right).
It has to be mentioned, that other excitation schemes (like, e.g., an octupolar excitation method [108–110]) are used in Penning-trap mass spectrometry. Since they are beyond the scope of the present work, they are not discussed here.

4.3.3 Mass-selective buffer-gas cooling

Cooling of the ions is essential in high-precision Penning-trap mass spectrometry. The amplitudes of the ion motions can be decreased by employing different techniques like, e.g., a resistive cooling method as used at PENTATRAP (see Sec. 6.1.4). At SHIPTRAP a mass-selective buffer-gas cooling technique [111] is employed and thus a brief description of the basic ideas is given here. A detailed analysis of damping effects in Penning traps can be found in [112–114].
Ions in a trap filled with a neutral buffer gas (e.g., helium) experience the loss of energy due to the collisions with gas atoms. This process can be modeled by including

a damping force

$$\boldsymbol{F} = -2m\gamma\boldsymbol{V} \tag{4.21}$$

into the equations of motion (see Eq. (3.4)). The damping coefficient γ derives from the ion mobility K and is given in the form

$$2m\gamma = \frac{q}{K} = \frac{q}{K_0} \cdot \frac{(p/p_0)}{T/T_0}, \tag{4.22}$$

where K_0 is the reduced ion mobility at normal atmospheric pressure $p_0 = 1013$ mbar and room temperature $T_0 = 300$ K. In presence of a buffer gas with a pressure of, e.g., 5×10^{-5} mbar (which is typical for SHIPTRAP) amplitudes of the cyclotron and axial motions decreases with damping constants $\gamma_+ \approx 18$ s^{-1} and $\gamma_z \approx 9$ s^{-1}, respectively. However, the magnetron radius increases due to a metastable nature of the motion with a constant of about 0.03 s^{-1}.
By applying a quadrupolar excitation with the frequency $\omega_{\mathrm{rf}} = \omega_+ + \omega_-$, Eq. (4.19) in presence of the damping force turns into

$$\frac{r_+^2(T_{\mathrm{rf}})}{r_-^2(0)} = e^{-i\tilde{\gamma}_1 t} \frac{4g^2}{|\bar{\omega}_R|^2} \left| \sin \frac{\bar{\omega}_R t}{2} \right|^2, \tag{4.23}$$

where $\tilde{\gamma}_1$ is a modified damping constant, which depends on the eigenfrequencies of the ion motions, and $\bar{\omega}_R = \sqrt{(\delta + 2i\gamma)^2 + 4g^2}$ is a complex "damped" Rabi frequency. Thus, the magnetron motion converts to the cyclotron motion with a subsequent cooling of the latter, i.e., the cyclotron radius shrinks. Since this process depends on the charge-to-mass ratio, a reduction of the radii (and thus a centering) can be done mass-selectively in order to clean the ion cloud (see Sec. 4.4.1).

4.3.4 Time-of-flight detection technique

In a time-of-flight ion-cyclotron-resonance (ToF-ICR) detection technique [112], the free cyclotron frequency and thus the mass of the ion is determined from the measurement of its time of flight after the ejection from the trap through a strong gradient of the magnetic field (Fig. 4.3). The time of flight depends on the ion's orbital magnetic moment $\boldsymbol{\mu}$ given for the ion in the Penning trap by

$$\boldsymbol{\mu} = -\frac{q}{2}\left(r_+^2\omega_+ + r_-^2\omega_-\right)\boldsymbol{e}_z = -\frac{E_r}{B_0}\boldsymbol{e}_z, \tag{4.24}$$

where E_r is the radial kinetic energy of the ion. A motion of the ion through the gradient of the magnetic field is usually performed adiabatically, i.e., its orbital magnetic moment remains constant. Hence, a magnetic field acts on the magnetic moment with a force $|\boldsymbol{F}| = |\boldsymbol{\nabla}(\boldsymbol{\mu}\boldsymbol{B})|$ and the time of flight between the trap located at zero position and

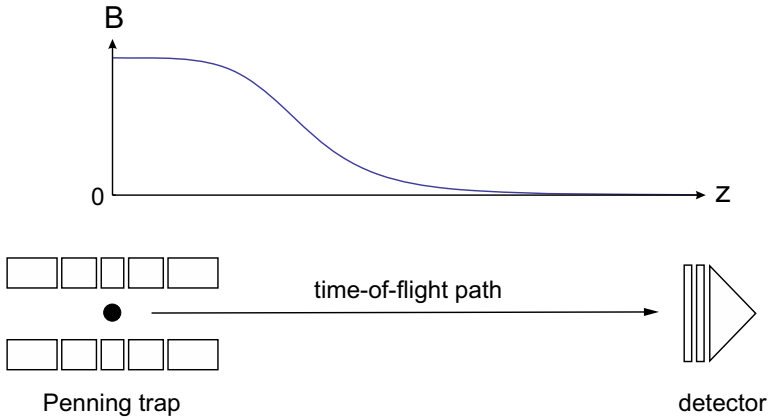

Figure 4.3: Schematic principle of the time-of-flight detection technique. The ion ejected from the trap is flying towards the detector through the gradient of the magnetic field. The time of flight is typically measured as a delay between the ejection and the ion signal coming from the detector. For details see text.

the detector at the position z_{det} can be calculated as

$$T(E_r) = \int_0^{z_{\mathrm{det}}} dz \cdot \sqrt{\frac{m}{2\left(E_0 - qV(z) - |\boldsymbol{\mu}(E_r)\boldsymbol{B}(z)|\right)}} \,, \tag{4.25}$$

where E_0 is the total initial energy of the ion, $V(z)$ and $B(z)$ are the electric potential and magnetic field, respectively, along the ion's path from the trap to the detector.
The radial kinetic energy of the ion can be manipulated by applying successively the dipolar and quadrupolar excitations with the frequencies ω_- and $\omega_c = \omega_+ + \omega_-$, respectively. If the ion is initially cooled and then prepared at a certain magnetron radius, after a full conversion with $\delta = 0$ its radial energy increases due to the increase of its radial frequency while the radius remains the same. After this, the ion is ejected from the trap towards the detector and its time of flight together with the sideband frequency is recorded. Thus, by varying the detuning of the sideband frequency around ω_c with repetitive measurement cycles a ToF-spectrum is acquired, which is supposed to be very similar to the inverted spectra in Fig. 4.2, and the free cyclotron frequency can be determined.
In Fig. 4.4 standard and Ramsey ToF-resonances of singly-charged ^{133}Cs obtained at SHIPTRAP using one-pulse and two-pulse excitation schemes are presented. The two-pulse technique is usually favorable, since it provides a better precision for the determination of the cyclotron frequency due to the more pronounced sidebands in the shape of the ToF-spectrum. Moreover, as it can be seen from Fig. 4.4, full-width-at-half-maximum (FWHM) defined by the excitation time is $\sim 0.9/T_{rf}$ for the standard resonance and $\sim 0.6/T_{rf}$ for the Ramsey resonance techniques, what assigns the better resolving power to the latter. However, a multiple fringe structure of the Ramsey ToF-ICR is a drawback in the sense that it does not allow a veracious resolution of two close masses in many practical cases.

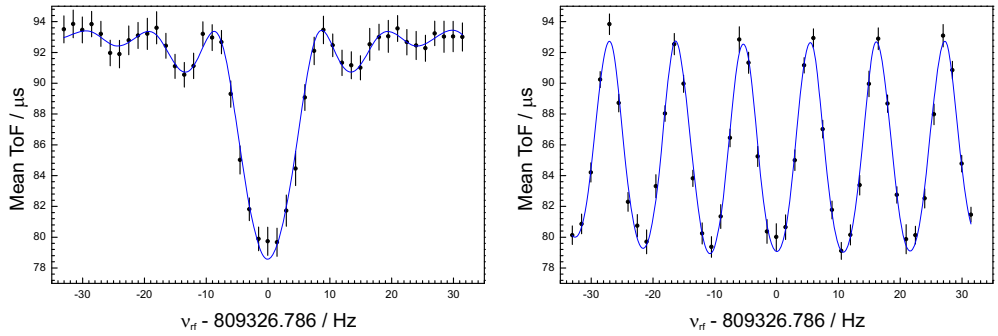

Figure 4.4: Time-of-flight ion cyclotron resonances of singly-charged ^{133}Cs obtained at SHIPTRAP using (left) a single excitation rf-pulse of length $T_{\mathrm{rf}} = 100$ ms (a standard ToF-ICR technique) and (right) two rf-pulses with identical length $\tau_1 = 10$ ms, separated by a waiting time interval $\tau_0 = 80$ ms (a Ramsey ToF-ICR technique).

4.4 Q-value measurements at SHIPTRAP

The SHIPTRAP mass spectrometer (GSI, Darmstadt, Germany) was build in order to perform direct high-precision mass measurements of short-lived heavy and super-heavy nuclides. For this purpose it was installed at the exit of the velocity filter SHIP (Separator for Heavy Ion reaction Production) [115], where heavy and super-heavy nuclei are produced in fusion-evaporation reaction. The main mission of SHIPTRAP is to investigate the regions of rare elements toward the drip lines and the expected island of stability across the chart of nuclides. It is worth mentioning that the first direct mass measurements of transuranium isotopes $^{252-254}$No and ^{255,256}Lr [116–118] were performed at SHIPTRAP. In the last few years SHIPTRAP was decoupled from the on-line ion source, what allowed to perform a series of mass ratio measurements for the determination of $Q_{\epsilon\epsilon}$-values for neutrino physics.

4.4.1 The off-line SHIPTRAP mass spectrometer

A detailed description of the on-line SHIPTRAP facility can be found in [120]. A "shortened" version of the SHIPTRAP mass spectrometer, the off-line SHIPTRAP setup, is illustrated in Fig. 4.5. Here the ions are produced by two types of sources: In the first case metallic or oxide samples are placed on a rotatable holder, where they are ionized by a laser induced desorption, fragmentation and ionization. The frequency-doubled Nd:YAG laser[2] (532 nm) has a pulse duration of 3-5 ns and a pulse energy of 4-12 mJ. The beam is focused by a lens system to a diameter of about 1 mm on the sample [121]. In the second case specimens in a gaseous form are ionized by a commercial electron-impact ion source SPECS IQE 12/38. This source was used for the measurements with singly charged ions of Xe-isotopes (see Chap. 5). After ionization, the ions are deflected with an electrostatic quadrupolar by 90° and transported towards

[2] The laser was used originally for a calibration of the spectrometer by means of carbon clusters [121].

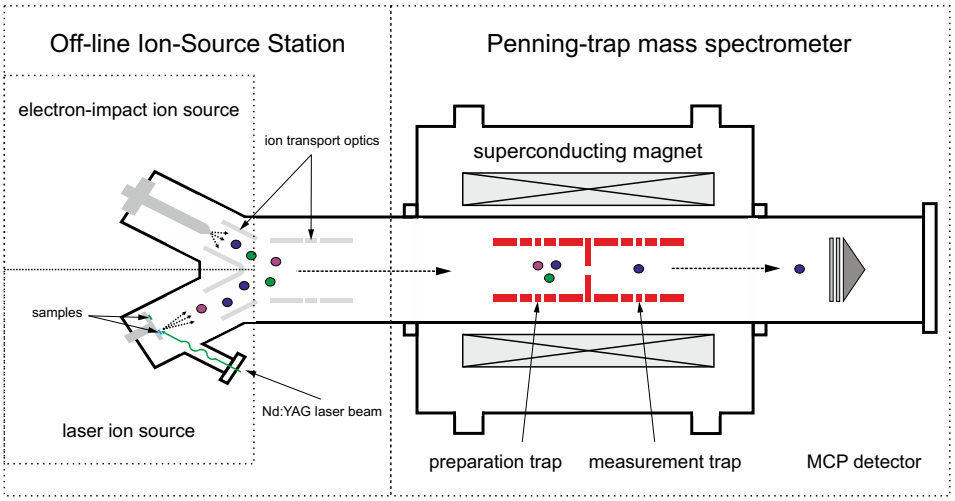

Figure 4.5: Illustration of the off-line SHIPTRAP mass spectrometer. The ions are produced with a laser ablation or an electron-impact ion source and guided by ion transport optics towards the Penning traps. After the mass-selective buffer-gas cooling and centering in the preparation trap, the ions are moved to the measurement trap, where the high-precision cyclotron frequency measurements are performed.

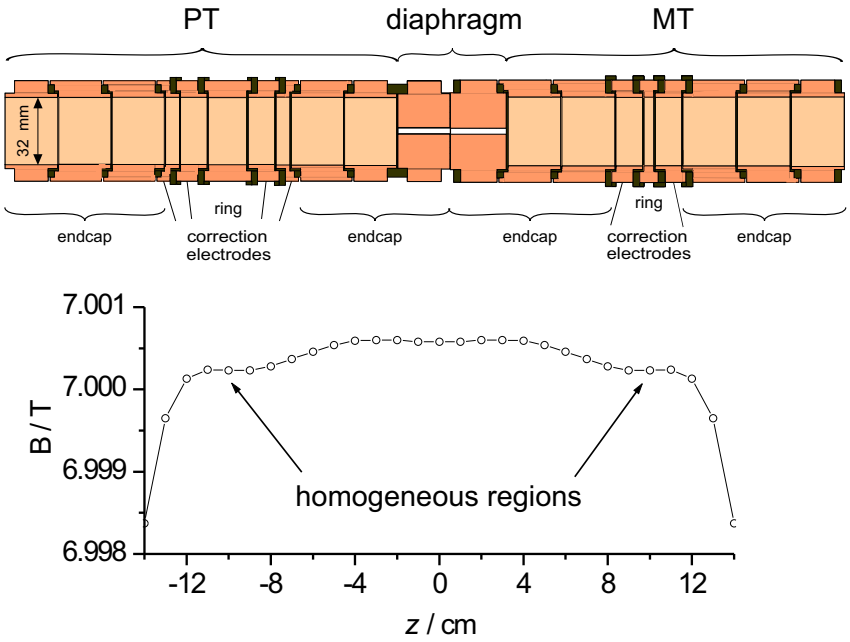

Figure 4.6: Schematic picture of the Penning-trap setup at SHIPTRAP (taken from [119]). (top-left) A 7-pole preparation trap (PT) with a wide central ring in order to maximize a capture efficiency. (top-right) A 5-pole measurement trap with a narrow ring and orthogonal geometry. Traps are separated by a thin diaphragm and set according to the position of two homogeneous regions of a 7 T magnetic field (bottom). For details see text.

the Penning traps by a series of electrostatic electrodes and Einzel lenses.
The Penning-trap section[3] of SHIPTRAP consists of two cylindrical Penning traps (see Fig. 4.6 (top)) – the preparation trap (PT) and the measurement trap (MT) – separated by a diaphragm with an inner diameter of 1.5 mm and a length of 52 mm. The geometry of the preparation trap is chosen to maximize a capture efficiency. Thus, the ring electrode has a width of 18.5 mm in comparison with a 4.7 mm width of the measurement trap's ring electrode. Inner diameter of the traps is 32 mm. In the PT ions after the injection are centered mass-selectively by means of a buffer-gas cooling technique [111] (see Sec. 4.3.3). For this the PT is filled with a helium gas at a pressure of about a few 10^{-6} mbar. Hence, the ejection of the centered ions from the PT to the MT through a tiny diaphragm allows to select single ion species of a certain mass.
The measurement trap, where the frequency measurements take place using the time-of-flight detection technique (see Sec. 4.3.4), is constructed in order to fulfill the orthogonality conditions (see Sec. 3.2.1). The diaphragm prevents the influence of a buffer-gas from the PT onto the MT, where pressure is usually below 10^{-7} mbar. Presence of buffer-gas contaminants in the measurement trap can result in unwanted systematic effects (see Sec. 5.3.3), but this was not the case for the present measurements.
Traps are positioned with respect to two homogeneous regions (Fig. 4.6 (bottom)) of a 7 T magnetic field created by a superconducting magnet. The relative spatial homogeneity in the central volume of 1 cm^3 is $\Delta B/B_0 \approx 10^{-6}$ for the PT and $\Delta B/B_0 \approx 10^{-7}$ for the MT. The long-term stability was measured over 440 days to be $\Delta B/B = -4.063(7) \times 10^{-10}$/h. Short-term fluctuations of the magnetic field are dominated by temperature and pressure variations of the environment. With pressure and temperature stabilization systems installed recently the relative magnetic field uncertainty was reduced from $\delta B/B_{old} = 3.54(17)\times10^{-8}$/h to $\delta B/B_{new} = 7.60(64)\times10^{-11}$/h. Details on the systematic studies of the magnetic field fluctuations and a description of the stabilization system can be found in [123].

4.4.2 Measurement procedure

A high-precision determination of the frequency ratio of an isobaric pair requires to provide similar initial conditions in the measurement trap. In order to fulfill this requirement, a careful maintenance starting from the ion production and up to the transportation from the PT to the MT was performed.
Ions of the corresponding isobaric pairs ^{106}Pd/ ^{102}Ru, ^{106}Cd/ ^{106}Pd, ^{144}Sm/ ^{144}Nd and ^{156}Dy/ ^{156}Gd were produced with a laser-ablation ion source. Samples of the nuclides were in form of oxides (^{106}Cd, ^{144}Sm, ^{156}Dy and ^{156}Gd) and metallic powder (^{102}Ru, ^{102}Pd, ^{106}Pd and ^{144}Nd). For isobaric purity and because of different ionization properties each sample was prepared on its own stainless steel plate. The laser intensity was tuned in every single measurement in order to keep the same count rate of up to 5 ions per measurement cycle. An alternation was realized by means of a rotating sample holder, which allowed a fast switching between two specimens. After the ionization,

[3] A detailed description of the traps can be found in the Ph.D. thesis of Günther Sikler [122].

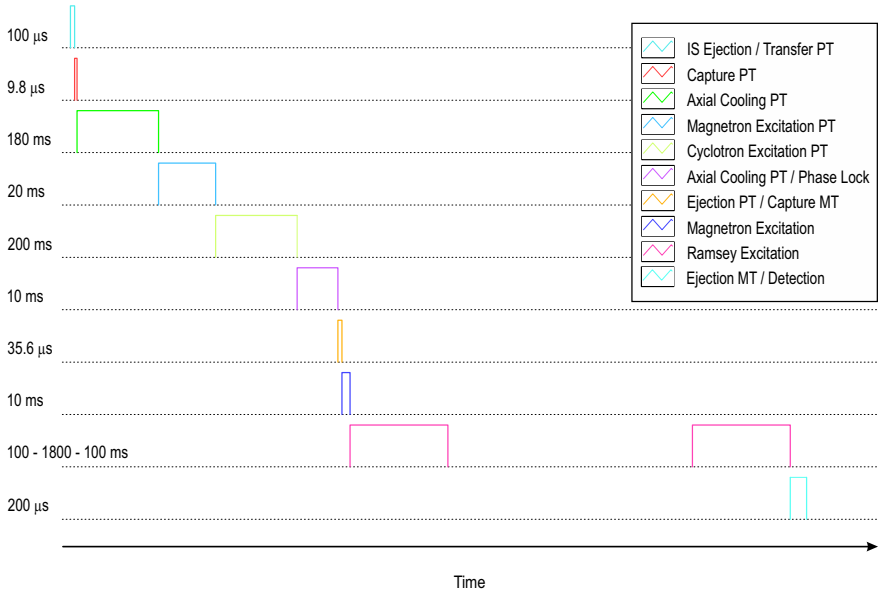

Figure 4.7: Illustration of a timing scheme for single Ramsey ToF-ICR measurements. Rectangles represent trigger pulses sent to the corresponding devices. The widths of the pulses are not in scale. For details concerning the measurement steps see text.

free ions were guided to the preparation trap and captured with a delay of about 100 μs (see Fig. 4.7). In order to keep the same initial conditions in the PT same settings of the ion optics were used for both nuclides in a pair.
In the preparation trap ions were cooled and centered mass-selectively. As it is mentioned in Sec. 4.3.3, large damping constants of the axial and modified cyclotron modes allow for the relatively fast self-cooling of these two motions (from tens to a few 100 of ms) in presence of a buffer-gas. However, the magnetron motion has to be cooled forcibly. For this a quadrupolar excitation at the sideband $\omega_+ + \omega_-$ was applied ("Cyclotron excitation PT" in Fig. 4.7) for about 180-200 ms. Prior to this a dipolar magnetron excitation ω_- was triggered, resulting in a simultaneous increase of the radii of all ions in the trap. Finally, only ions of a desired mass were kept closer to the center of the PT for further transportation through the diaphragm to the MT, and with a mass resolving power of the method estimated to be of about 100000 [124] any mass contamination was considered to be negligible. As it is possible to let the ions pass through the MT without being trapped, the cooling efficiency was controlled by directly obtaining a ToF-spectrum with respect to the cooling parameters.
In the MT cooled ions were prepared at certain magnetron radii in order to maximize the radial energy and to improve the resonant character of the ToF-spectra, what was done with a dipolar excitation at the magnetron frequency ω_-. For both isobars the same magnetron frequency was expected. After the magnetron excitation, a Ramsey-type quadrupolar excitation with two pulses of length $\tau_1 = 100$ ms separated by a time delay $\tau_0 = 1800$ ms was applied at the sideband frequency $\omega_c = \omega_+ + \omega_-$. Finally the ions were ejected towards the MCP detector and the measurement cycle was restarted.

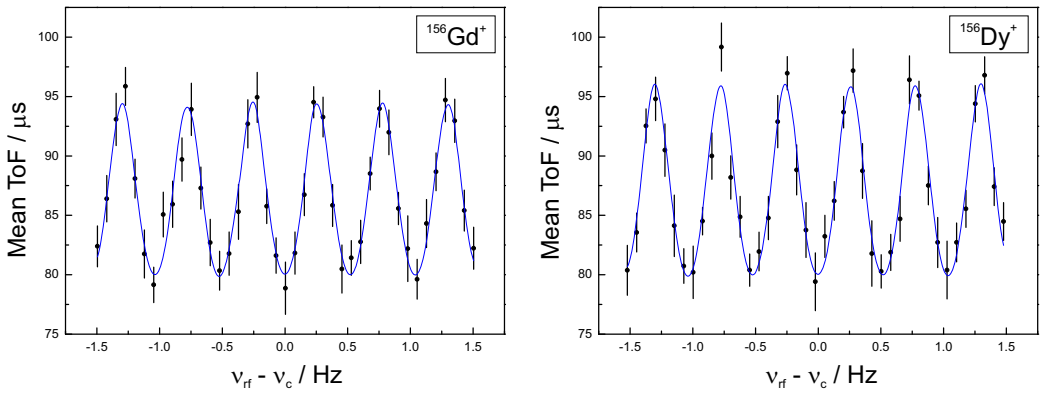

Figure 4.8: Exemplary time-of-flight resonances of $^{156}Gd^{+}$ and $^{156}Dy^{+}$. The blue lines are the theoretical fits to the data [103]. As the results of the fits, the estimated free cyclotron frequencies are 689860.462(4) Hz and 689850.937(4) Hz, respectively.

Time-of-flight spectra were obtained by scanning a narrow range of 3 Hz with 41 bins around the expected resonance frequency. For a coarse tuning of the resonance frequency standard ToF-ICR spectra were obtained prior to the Ramsey measurements (as, e.g., in Fig. 4.4 (left)). In order to minimize non-linear effects of the magnetic field fluctuations and at the same time to reach higher statistics a compromise measurement time of about 30-40 minutes was chosen resulting in an acquisition of 400-900 ions for one time-of-flight spectrum.
As an example, typical Ramsey ToF-resonances of ^{156}Gd and ^{156}Dy are shown in Fig. 4.8. Fits of a theoretical line shape (see [103] and considerations in Sec. 4.3.2) to the data points were obtained using the analysis program EVA, developed by S. Schwarz. As the results of the fits, the free cyclotron frequencies of $^{156}Gd^{+}$ and $^{156}Dy^{+}$ ions are 689860.462(4) Hz and 689850.937(4) Hz, respectively. The total data obtained at SHIPTRAP for the frequency ratio determination are shown in Fig. 4.9, Fig. 4.10, Fig. 4.11 and Fig. 4.12 for the corresponding pairs of ^{106}Pd/^{102}Ru, ^{144}Sm/^{144}Nd, ^{106}Cd/^{106}Pd and ^{156}Dy/^{156}Gd.

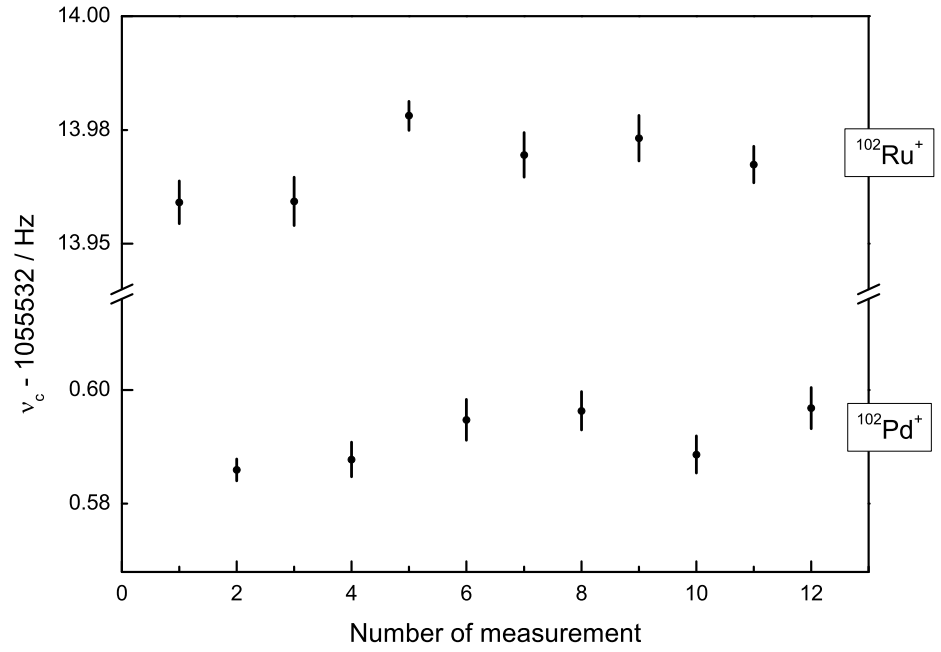

Figure 4.9: The total frequency data of $^{102}Pd^+$ and $^{102}Ru^+$, acquired over 1 day.

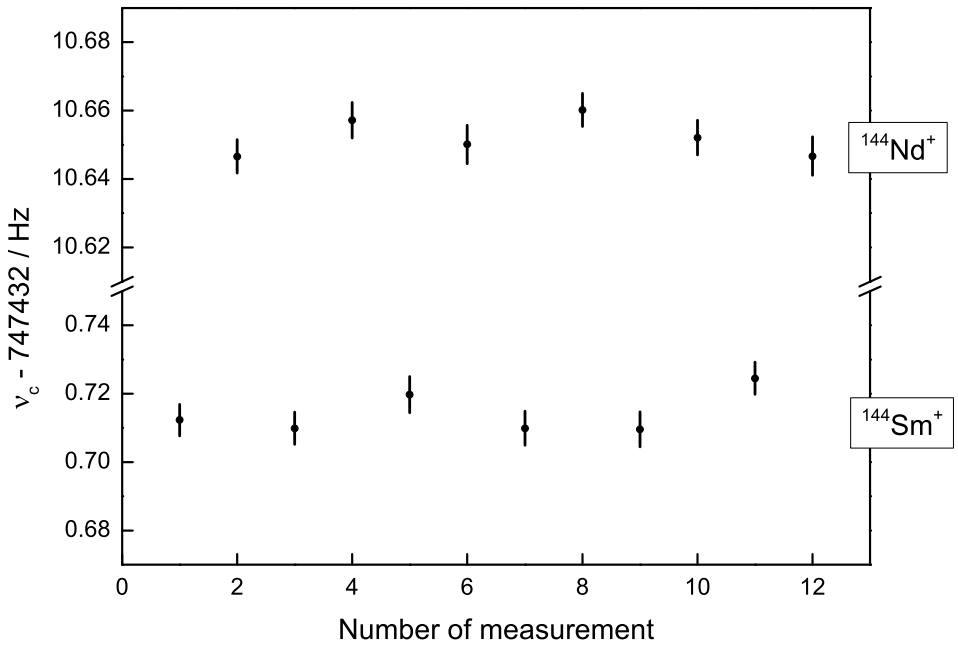

Figure 4.10: The total frequency data of $^{144}Sm^+$ and $^{144}Nd^+$, acquired over 1 day.

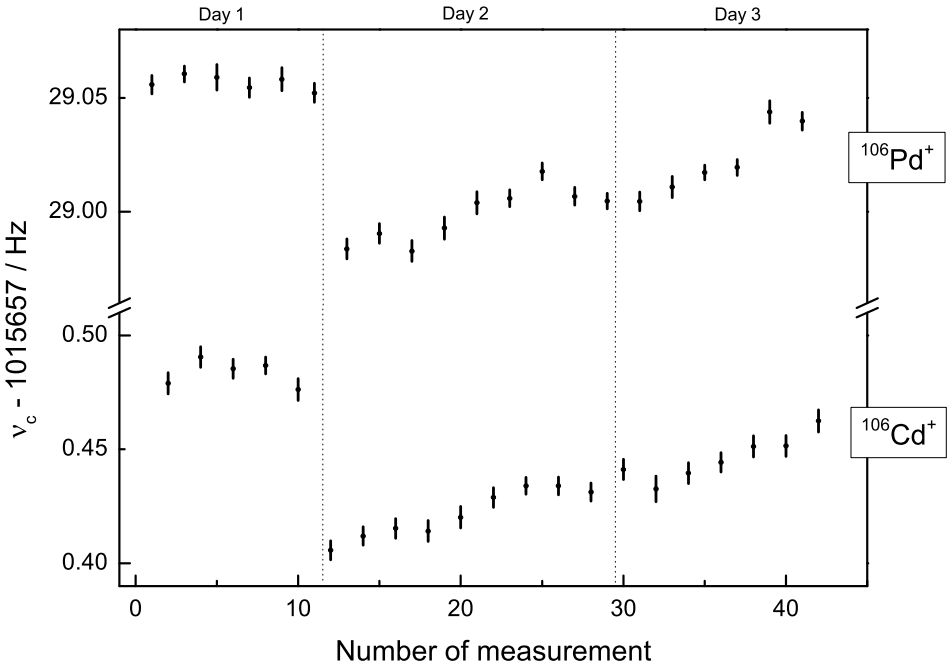

Figure 4.11: The total frequency data of $^{106}Cd^+$ and $^{106}Pd^+$, acquired over 3 days.

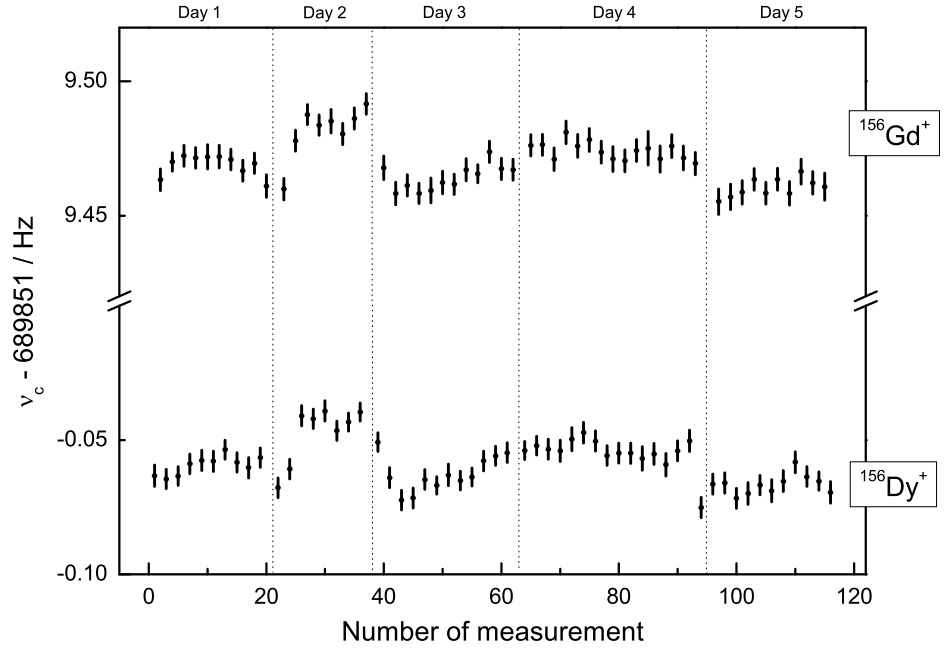

Figure 4.12: The total frequency data of $^{156}Dy^+$ and $^{156}Gd^+$, acquired over 5 days.

4.4.3 Data analysis

The total data for the frequency ratio determination of the pairs ^{102}Pd/ ^{102}Ru (Fig. 4.9), ^{144}Sm/ ^{144}Nd (Fig. 4.10), ^{106}Cd/ ^{106}Pd (Fig. 4.11) and ^{156}Dy/ ^{156}Gd (Fig. 4.12) were obtained at SHIPTRAP within one day for the first two pairs and within 3 and 5 days for ^{106}Cd/ ^{106}Pd and ^{156}Dy/ ^{156}Gd, respectively. The requirements on the statistics were set due to the expected Q-values (see Tab. 4.1) together with the preliminary analysis of the data during the data acquisition. For all pairs the SHIPTRAP setup was tuned prior to the main measurements and test data were accumulated, which are not presented here.
For a single data point (i.e. for one time-of-flight resonance) a statistical uncertainty was obtained by the fit routine of the EVA program[4]. The typical value of the uncertainty provided by the program was less than 5 mHz for all nuclides under consideration, what corresponds to the relative statistical uncertainty $\delta\nu_c^{\mathrm{stat}}/\nu_c < 7 \times 10^{-9}$.
With the aimed 1 ppb precision on the determination of the mass ratio of isobaric pairs (see Sec. 4.2) most of the sources of systematic errors were excluded in the present analysis. An extensive study of systematic effects at SHIPTRAP within Q-value measurements by means of Ramsey ToF-ICR is given in [127]. In particular, the uncertainty of the cyclotron frequency determination caused by the magnetic field fluctuations was expected to be well below 10^{-10} with the temperature and pressure stabilization system installed to govern the ambient conditions [123]. A substantial frequency shift of $\sim$ 60 mHz between days 1 and 2, which can be seen in Fig. 4.11, is due to the fluctuations of the trapping voltage caused by the fluctuations of the ambient conditions[5] (see Sec. 5.3.3, Fig. 5.10). These fluctuations introduce a relative uncertainty in the frequency ratio determination which is well below 10^{-10}, and hence can be neglected.

Error propagation of the data set

In the absence of additional systematic effects and with respect to the mass proximity of the corresponding nuclides the individual frequency ratios were determined using Eq. (4.8) and Eq. (4.9). Eq. (4.10) was used for the determination of their uncertainties. With all considerations given above only this uncertainty was used. The analysis of the data sets was done following the least-square adjustment routine given in [128, 129] with some simplifications like omitting the variance-covariance analysis. The resulting frequency ratios were obtained as weighted means of N individual ratios R_i

$$\bar{R} = \frac{\sum_i^N w_i R_i}{\sum_i^N w_i} \tag{4.26}$$

[4] Program EVA is used for data analysis in some other Penning-trap mass spectrometry experiments based on the ToF-ICR detection technique like, e.g., ISOLTRAP [125] and TRIGA-TRAP [126].
[5] Note that the voltage sources were not covered by the stabilization system.

with the individual instrumental weights given as

$$w_i = \frac{1}{\delta R_i^2} \tag{4.27}$$

and, consequently, with errors of the mean ratios given as

$$\delta\bar{R} = \frac{1}{\sqrt{\sum_i^N w_i}}. \tag{4.28}$$

Thus, an assumption on the normal distribution of the data was made. According to this the reduced χ^2 is given as

$$\chi^2 = \frac{\sum_i^N w_i(R_i - \bar{R})^2}{N-1}, \tag{4.29}$$

and even more strong

$$R_B = \sqrt{\chi^2}, \tag{4.30}$$

which is called *the Birge ratio*. In principle, Eq. (4.29) and Eq. (4.30) should indicate the convergence of the data with $\chi^2 \approx R_B \approx 1$. However, it was not the case due to the error propagation routine in the EVA program. Since the program was developed for mass-measurements on short-lived nuclides with low production rates, the error of the frequency determination in the fit routine is overestimated in case of high statistics and thus the Birge ratio[6] was typically $R_B < 1$ in the present analysis. This effect has been seen by several groups using EVA and occurs in all Q-value measurements performed recently at SHIPTRAP (see references in [74]).
In order to solve this problem the correction of the error dispersion (which is naturally given by Eq. (4.28)) can be done by

$$\delta R^2 \rightarrow \chi^2 \delta R^2, \tag{4.31}$$

and the corrected error of the mean ratio is then given by

$$\delta\bar{R}_{\mathrm{corr}} = \sqrt{\frac{1}{\sum_i^N w_i} \cdot \frac{\sum_i^N w_i(R_i - \bar{R})^2}{N-1}}\ , \tag{4.32}$$

which turns to the standard deviation, divided by $\sqrt{N}$, with the infinitely large number of measurements. Eq. (4.32) holds even in the case of strong over- and underestimation of the instrumental errors. Hence, it was chosen to define the statistical uncertainty for the mean values of the frequency ratios.

[6] Reciprocally $R_B > 1$ corresponds to the underestimated data.

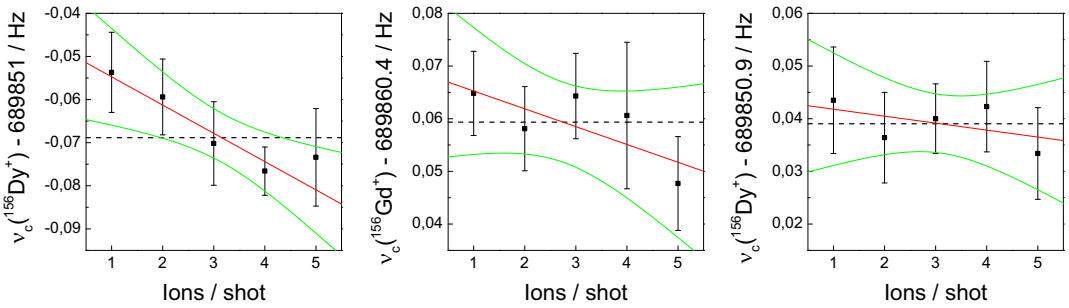

Figure 4.13: *Z*-class analysis of three consecutive frequency measurements. Data are separated by number of ions per shot (shelved on the abscissa). The red lines represent linear fits to the data and green boundaries mark the 95 % confidence bands. Dashed lines are the corresponding mean values. The decreasing of the linear trend can be due to the initial daily fluctuations of the ambient conditions influencing the preparation trap. For details see text.

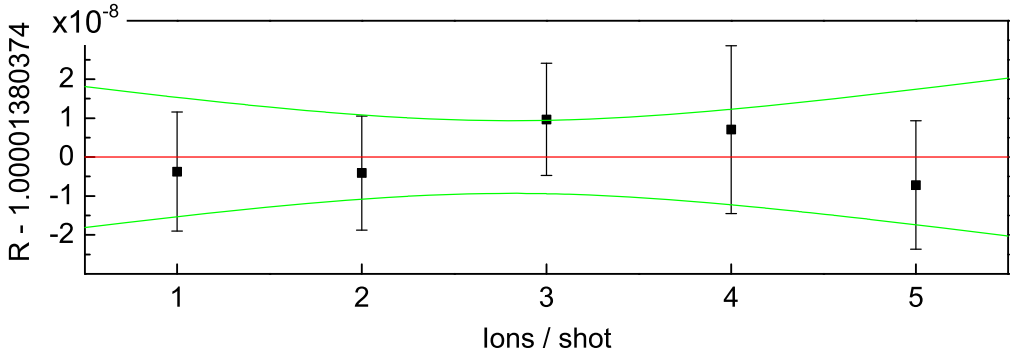

Figure 4.14: The resulting frequency ratio of the data triplet shown in Fig. 4.13 is presented depending on the number of ions per shot. The red line indicates the mean value with the green 95 % confidence bands. No visible influence of the contaminant ions can be seen. See text for details.

Z-class analysis

The Coulomb interaction between the large number of simultaneously trapped ions can result in the modified electric potential due to the image-charge effect [130]. Even though it has been found that the image-charge shift at the sideband frequency $\omega_c = \omega_+ + \omega_-$ is zero for the ions of the same mass, the effect can appear in presence of contaminant ions [112, 131]. Thus a compromise between high statistics and low number of ions in the trap was found restricting the measurements to only 1-5 ions per measurement cycle. Even with an employment of the purification procedure in the PT the presence of contaminant ion species could not be fully excluded. To this end, in order to completely investigate the influence of contamination ions on the resulting frequencies a so-called *z-class* analysis was performed.
That is, the data were separated according to the number of simultaneously trapped ions and every class was linearly interpolated in order to reveal the trend in the frequency and, consequently, in the ratio determination. An example of a suspicious behavior

Table 4.2: Mean cyclotron frequency ratios $\overline{R}$ of the isobaric pairs ^{102}Pd/ ^{102}Ru, ^{144}Sm/ ^{144}Nd, ^{106}Cd/ ^{106}Pd and ^{156}Dy/ ^{156}Gd obtained by the linear interpolation method. The data analysis was performed for both isobars of the corresponding pairs. In columns 4 and 5 relative uncertainties and Birge ratios are given, respectively.

$0\nu\epsilon\epsilon$-transition	Reference	$\overline{R}$	$\delta\overline{R}/\overline{R}$	R_B
^{102}Pd $\rightarrow$ ^{102}Ru	^{102}Pd$^+$	1.0000126764(38)	2.6 $\times 10^{-9}$	0.67
	^{102}Ru$^+$	1.0000126762(28)	1.6 $\times 10^{-9}$	0.40
^{106}Cd $\rightarrow$ ^{106}Pd	^{106}Cd$^+$	1.0000281337(10)	1.0 $\times 10^{-9}$	0.65
	^{106}Pd$^+$	1.0000281348(8)	0.8 $\times 10^{-9}$	0.51
^{144}Sm $\rightarrow$ ^{144}Nd	^{144}Sm$^+$	1.0000132986(52)	4.1 $\times 10^{-9}$	0.63
	^{144}Nd$^+$	1.0000132971(65)	5.4 $\times 10^{-9}$	0.83
^{156}Dy $\rightarrow$ ^{156}Gd	^{156}Dy$^+$	1.00001381140(63)	0.6 $\times 10^{-9}$	0.57
	^{156}Gd$^+$	1.00001381112(70)	0.7 $\times 10^{-9}$	0.65

Table 4.3: Resulting cyclotron frequency ratios R, their relative uncertainties and the $Q_{\epsilon\epsilon}$-values of the transitions ^{102}Pd $\rightarrow$ ^{102}Ru, ^{144}Sm $\rightarrow$ ^{144}Nd, ^{106}Cd $\rightarrow$ ^{106}Pd and ^{156}Dy $\rightarrow$ ^{156}Gd obtained by averaging the mean ratios of the corresponding isobaric pairs.

$0\nu\epsilon\epsilon$-transition	R	$\delta R/R$	$Q_{\epsilon\epsilon}$/ keV
^{102}Pd $\rightarrow$ ^{102}Ru	1.0000126763(38)	3.8 $\times 10^{-9}$	1203.27(36)
^{106}Cd $\rightarrow$ ^{106}Pd	1.0000281343(10)	1.0 $\times 10^{-9}$	2775.39(10)
^{144}Sm $\rightarrow$ ^{144}Nd	1.0000132978(65)	6.5 $\times 10^{-9}$	1782.59(87)
^{156}Dy $\rightarrow$ ^{156}Gd	1.00001381126(70)	0.7 $\times 10^{-9}$	2005.95(10)

due to probable contaminants is shown in Fig. 4.13. Three frequency data points were obtained consequently as the first morning data in a day's measurement and thus the decreasing linear trend can be explained by the temperature fluctuations influencing the voltage sources and hence a purification in the PT. R was obtained for every z-class as a ratio between $\nu_c(^{156}\text{Gd}^+)$ (Fig. 4.13b) and $\tilde{\nu}_c(^{156}\text{Dy}^+)$, derived by linear interpolation of two adjacent frequencies (Fig. 4.13a and Fig. 4.13c, respectively) to the time, when the frequency of ^{156}Gd$^+$ was measured. The result is shown in Fig. 4.14 and no strong dependence on the number of ions is revealed.

Resulting frequency ratios and the Q-values

For completeness two cases were investigated for each isobaric pair, in which the frequencies of the mother nuclide in a pair were obtained by linear interpolation of the measured frequencies of the daughter nuclide (i.e., reference frequencies) and *vice versa* (see Sec. 4.2.1). The resulting ratios were obtained as a mean of both interpolations. Tab. 4.2 summarizes the estimated values of the mean ratios evaluated for both cases. In Fig. 4.15, Fig. 4.16, Fig. 4.17 and Fig. 4.18 the resulting ratios of the interpolation are presented. Here for the determination of R the frequencies of $^{102}Ru^{+}$, $^{144}Nd^{+}$, $^{106}Pd^{+}$ and $^{156}Gd^{+}$ were obtained by linear interpolation, while frequencies of $^{102}Pd^{+}$, $^{144}Sm^{+}$, $^{106}Cd^{+}$ and $^{156}Dy^{+}$ were directly measured (see Sec. 4.2.1).
The $Q_{\epsilon\epsilon}$-values of the $^{102}Pd \rightarrow {}^{102}Ru$, $^{106}Cd \rightarrow {}^{106}Pd$, $^{144}Sm \rightarrow {}^{144}Nd$ and $^{156}Dy \rightarrow {}^{156}Gd$ double-electron capture transitions were calculated according to Eq. (4.6). The uncertainty due to the discussion in Sec. 4.2 was estimated as

$$\frac{\delta Q_{\epsilon\epsilon}}{Q_{\epsilon\epsilon}} = \frac{\delta R}{R-1}. \tag{4.33}$$

Thus, the mass of either nuclide could be taken from [94]. For the present results the masses of daughter nuclides of ^{102}Ru, ^{106}Pd, ^{144}Nd and ^{156}Gd were used. The mass of the electron was taken from [99]. The final results on the R and $Q_{\epsilon\epsilon}$ determination are presented in Tab. 4.3.
It is worth mentioning the polynomial method, which was used as an alternative to the linear interpolation method for the data analysis in similar measurements presented in the Ph.D. thesis of C. Roux [88]. In the method the magnetic field (and thus the cyclotron frequencies) is approximated by a polynomial of n-th order in contrast to the linear approximation used in the present analysis. The advantage of the method is that it efficiently ignores the fast nonlinear fluctuations of the magnetic field. Hence, it is a method of choice in case of the large scattering of data. As it can be seen from pictures representing the evaluated ratios of the current analysis (Fig. 4.15, Fig. 4.16, Fig. 4.17, Fig. 4.18), the scattering can be successfully neglected for all cases and thus the linear interpolation method is sufficient. The polynomial method is a regular tool in several other Penning-trap experiments (see, e.g., [23, 132]).

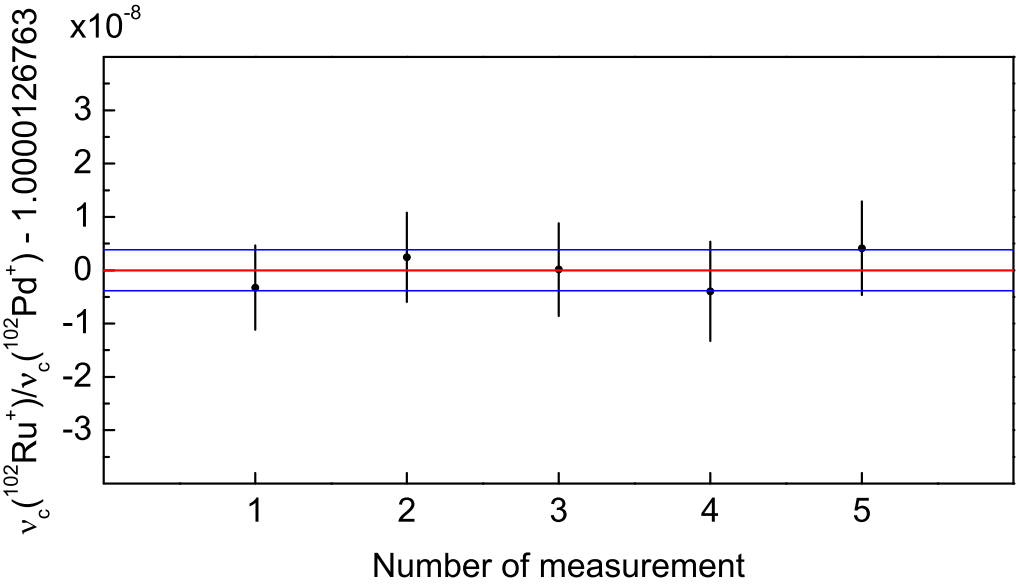

Figure 4.15: Cyclotron frequency ratios of $^{102}Ru^+$ and $^{102}Pd^+$. The red line represents the mean value and the blue lines mark its uncertainty. The ratios were calculated with $\nu_c(^{102}Pd^+)$ as the interpolated frequencies.

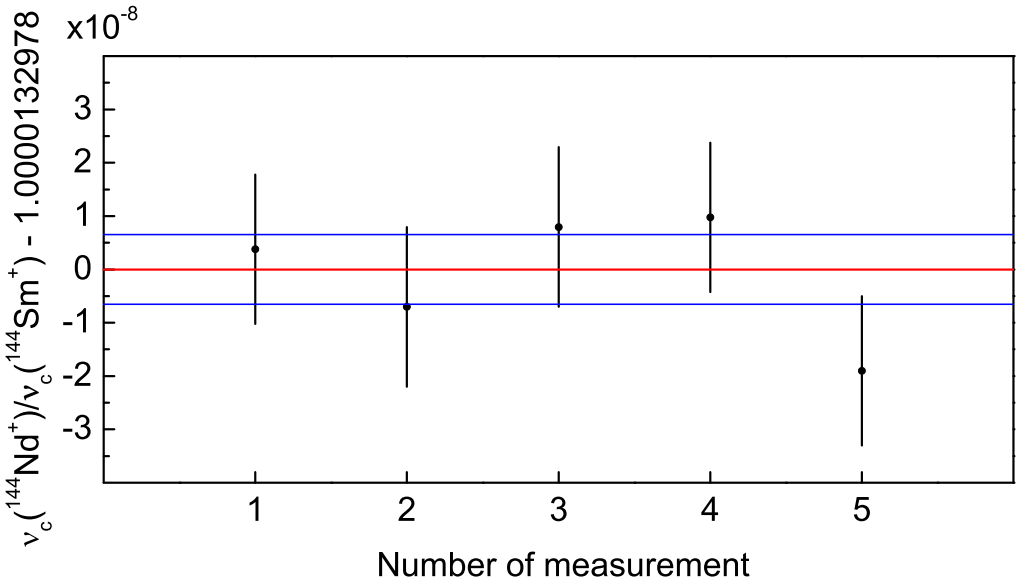

Figure 4.16: Cyclotron frequency ratios of $^{144}Nd^+$ and $^{144}Sm^+$. The red line represents the mean value and the blue lines mark its uncertainty. The ratios were calculated with $\nu_c(^{144}Sm^+)$ as the interpolated frequencies.

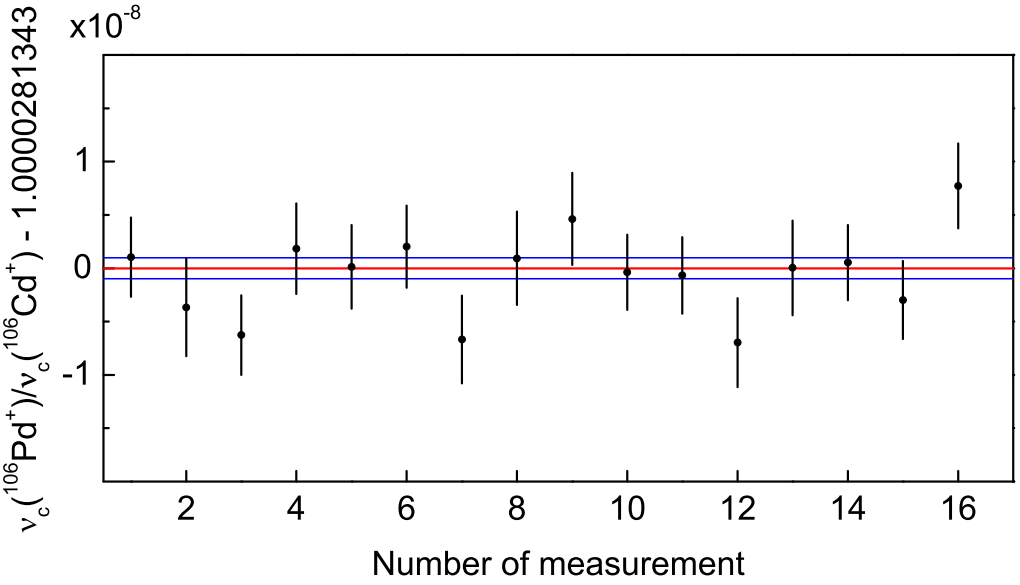

Figure 4.17: Cyclotron frequency ratios of $^{106}Pd^+$ and $^{106}Cd^+$. The red line represents the mean value and the blue lines mark its uncertainty. The ratios were calculated with $\nu_c(^{106}Cd^+)$ as the interpolated frequencies.

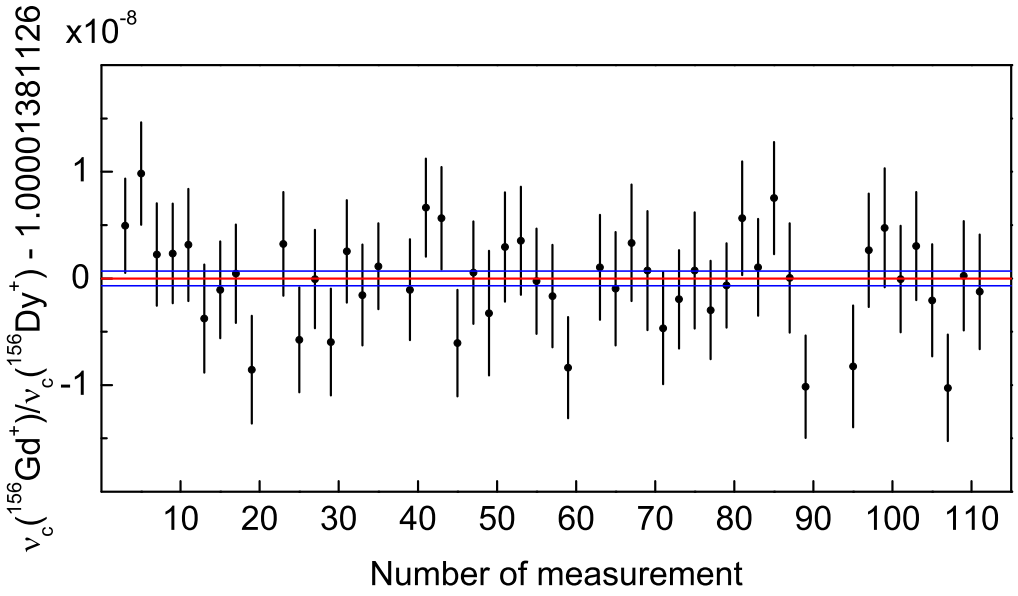

Figure 4.18: Cyclotron frequency ratios of $^{156}Gd^+$ and $^{156}Dy^+$. The red line represents the mean value and the blue lines mark its uncertainty. The ratios were calculated with $\nu_c(^{156}Dy^+)$ as the interpolated frequencies.

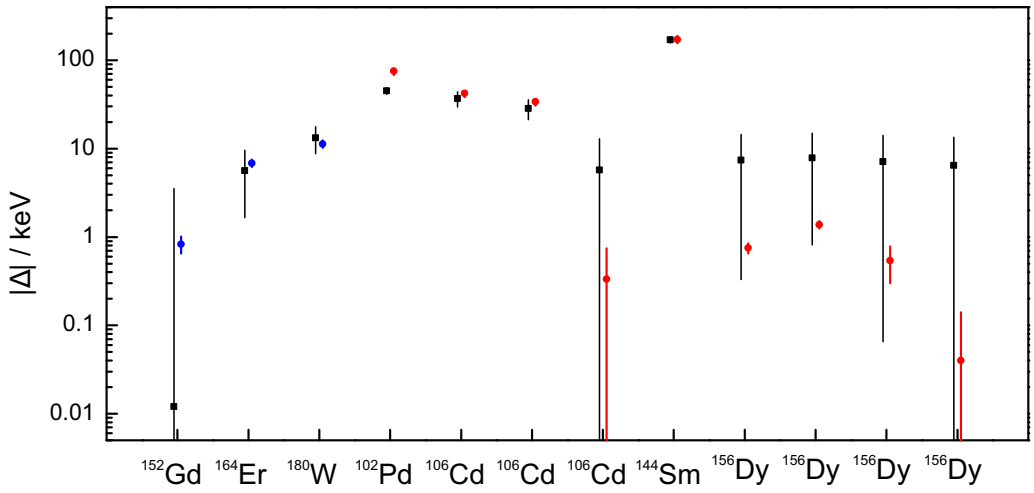

Figure 4.19: Previous and present estimates on the degeneracy parameters Δ for the transitions listed in Tab. 4.4. The black data points indicate the values calculated from the previous mass data [94], the blue points correspond to the gound-to-ground state transitions, for which Δ was directly determined at SHIPTRAP [108, 133, 134] and the red ones represent the data obtained within the present work.

4.5 Resonance enhancement of $0\nu\epsilon\epsilon$ in ^{102}Pd, ^{106}Cd, ^{144}Sm and ^{156}Dy

At SHIPTRAP, a search for the possible resonance enhancement of the neutrinoless double-electron capture transitions has started with the investigation of the ground-to-ground state transitions in ^{152}Gd [133], ^{164}Er [108] and ^{180}W [134]. These nuclides were found to be favorable due to their small estimated degeneracy fa4ctors Δ (see Sec. 4.1) and large matrix elements. The mass ratios and the corresponding Q-values of ^{102}Pd $\rightarrow$ ^{102}Ru, ^{106}Cd $\rightarrow$ ^{106}Pd, ^{144}Sm $\rightarrow$ ^{144}Nd and ^{156}Dy $\rightarrow$ ^{156}Gd were obtained within the present thesis work. The results are presented in Tab. 4.4 in order to compare with those corresponding to the ground-to-ground state transitions and with the previous values, based on differences of absolutely measured ground-state masses [94].
The degeneracy parameters Δ can be calculated first in order to estimate the enhancing nature of the resonances. Since for ^{152}Gd, ^{164}Er, ^{180}W and ^{156}Dy the expected degeneracy was less than 1 keV, accurate calculations of the two-hole binding energy B_{2h} were done in [108, 133–135], respectively, using the Dirac-Fock method, what is beyond the scope of the present work. In all other cases the two-hole binding energy was roughly estimated as $B_{2h} = B_{h1} + B_{h2}$ with $B_{h1,2}$ taken from [84]. The values E_γ of the energy of the nuclear excited states were taken from [95]. The estimates on the degeneracy parameters listed in Tab. 4.4 are shown in Fig. 4.19. Even though remarkable increase in the precision on the determination of the resonance parameters is achieved, none of the transitions experiences full degeneracy with the excited daughter states.

Table 4.4: Recently obtained Q-values of the neutrinoless double-electron capture transitions. A table summarizes the results of the Q-value measurements presented in this work in comparison with the resonance parameters of the ground-to-ground state transitions in ^{152}Gd [133], ^{164}Er [108] and ^{180}W [134] also obtained at SHIPTRAP. $Q_{\epsilon\epsilon}^{\text{old}}$ is the previous mass difference of the corresponding isobars taken from [94] and $Q_{\epsilon\epsilon}^{\text{new}}$ is obtained by means of Penning-trap mass spectrometry. Δ is the degeneracy parameter estimated with recently obtained $Q_{\epsilon\epsilon}^{\text{new}}$. For details see text.

Transition	E_γ (keV)	B_{2h} (keV)	$Q_{\epsilon\epsilon}^{\text{old}}$ (keV)	$Q_{\epsilon\epsilon}^{\text{new}}$ (keV)	Δ (new) (keV)
^{152}Gd $\rightarrow$ ^{152}Sm		54.87	54.6(35)	55.70(18)	0.83(18)
^{164}Er $\rightarrow$ ^{164}Dy		18.25	23.3(39)	25.07(12)	6.82(12)
^{180}W $\rightarrow$ ^{180}Hf		131.96	144.4(45)	143.20(27)	11.24(27)
^{102}Pd $\rightarrow$ ^{102}Ru	1103.047(13)	24.96	1173.0(36)	1203.27(36)	75.26(36)
^{106}Cd $\rightarrow$ ^{106}Pd	2705.30(8)	27.95	2770.0(72)	2775.39(10)	42.14(13)
	2713.89(8)	27.52			33.98(13)
	2748.2(4)	27.52			-0.33(41)
^{144}Sm $\rightarrow$ ^{144}Nd	1560.92(13)	49.78	1781.2(18)	1782.59(87)	171.89(87)
^{156}Dy $\rightarrow$ ^{156}Gd	1946.375(6)	58.82	2012.2(74)	2005.95(10)	0.75(10)
	1952.385(7)	52.19			1.37(10)
	1988.5(2)	16.91			0.54(24)
	2003.749(5)	2.16			0.04(10)

With the proposed lists of candidates [79, 96, 97] more isobaric pairs have been recently investigated. The first measurements on the Q-values of ^{112}Sn $\rightarrow$ ^{112}Cd, ^{136}Ce $\rightarrow$ ^{136}Ba and ^{74}Se $\rightarrow$ ^{74}Ge transitions were performed at JYFLTRAP [136–138] and ^{74}Se $\rightarrow$ ^{74}Ge was also measured at the FSU-TRAP [139]. The $Q_{\epsilon\epsilon}$-value of ^{184}Os $\rightarrow$ ^{184}W was obtained at TRIGATRAP [140] and the majority of the transitions were investigated at SHIPTRAP [108, 133, 134, 141, 142].

Within a set of the recently renewed $Q_{\epsilon\epsilon}$-values several remarkable candidates have to be mentioned. For ^{152}Gd $\rightarrow$ ^{152}Sm, for ^{106}Cd $\rightarrow$ ^{106}Pd with the transition to the nuclear energy level $E_\gamma = 2748.2(4)$ keV and for ^{156}Dy $\rightarrow$ ^{156}Gd with the multiple transitions to the nuclear excited states the degeneracy parameters Δ are smaller than 1 keV. The half-life of ^{152}Gd, normalized to the effective Majorana neutrino mass $|m_{\beta\beta}| = 1$ eV, was estimated to be of about 10^{26} years [133]. However, with the natural abundance of 0.2% this isotope not likely can be considered suitable for the $0\nu\epsilon\epsilon$ experiments. The resonance enhancement of the transition in ^{106}Cd to the nuclear excited state with $E_\gamma = 2748.2(4)$ keV is also not so promising since the probability is suppressed within

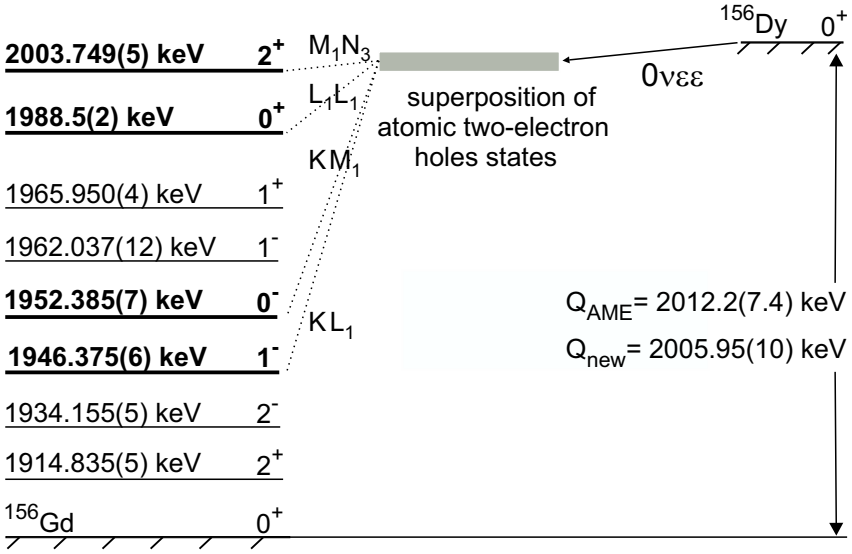

Figure 4.20: Scheme of the $0\nu\epsilon\epsilon$-transition in ^{156}Dy. Shown are only the nuclear excited states in ^{156}Gd with spin $I_f \leq 2$ [95], to which a resonantly enhanced $0\nu\epsilon\epsilon$ can result in a half-life short enough for a realistic search for neutrinoless double-electron capture. The transitions to the nuclear excited states highlighted with thick lines are resonantly enhanced.

the poor present knowledge on the nuclear structure of this isotope, which implies the possible spin state $I_f = (2,3)^-$ for this nuclear level.
An interesting phenomenon was discovered in ^{156}Dy. Here, four transitions to the nuclear excited states are resonantly enhanced (see Fig. 4.20) [135]. The transition to the nuclear excited state with energy 2003.749(5) keV is fully resonantly enhanced with $\Delta = (40 \pm 100)$ eV, but again the spin state is $I_f = 2^+$ and the electron capture goes from M- and N- shells of the atom, what strongly suppresses the probability of this transition. For the transition to the nuclear excited state with energy 1946.375(6) keV and spin $I_f = 1^-$, a small nuclear matrix element results in the estimated half-life of larger than 10^{30} years. For the two remaining transitions to the nuclear levels with spins and energy 0^+ and 1988.5(2) keV, 0^- and 1952.385(7) keV, the partial half-life, normalized to $|m_{\beta\beta}| = 1$ eV, was estimated to be 6×10^{28} years [135] assuming that the corresponding values of the nuclear matrix elements are similar to those of the transitions to the ground states due to zero spins of both nuclear excited states. In all cases the major restriction on the probability of the transition arises from the poor knowledge of the nuclear structure. Thus, the multiresonance enhancement of the neutrinoless double-electron capture in ^{156}Dy is interesting, but not really an applicable phenomenon unless the improvements in the field of nuclear structure physics will occur.

Chapter 5

Novel Phase-Imaging Ion-Cyclotron-Resonance technique

The development of Penning-trap mass spectrometry has provided a precise instrument for the investigation of radioactive elements being far from "the valley of stability" on the chart of nuclides [14, 143]. The first Penning-trap experiments on short-lived nuclides were performed at ISOLTRAP [144–146] employing the ToF-ICR detection technique. With the same technique the masses of short-lived nuclides were also measured, e.g., at SHIPTRAP [147, 148] and JYFLTRAP [148, 149]. The applications of these investigations can be found in many fields of physics such as, e.g., studies of the nuclear structure [150, 151] or stellar nucleosynthesis [152, 153].

A relative precision of the Penning-trap mass measurements on short-lived nuclides with half-lives down to few hundreds ms is about 10^{-8} for the medium-heavy mass range. Since the production mechanisms are typically not mass-selective, the nuclides of interest and their isobars or even isomers with similar masses are to be resolved. However, the time-of-flight detection technique does not provide the mass resolution better than few 10^5 [124, 125], which corresponds to $\sim$1 MeV/c^2 for singly charged ions with $A \sim 200$. In many cases this is not sufficient to resolve ion species with very close masses. To this end, new techniques have to be developed in order to perform high-precision mass-measurement experiments on nuclides with half-lives below few hundreds ms. One recently presented approach is to employ a multi-reflection time-of-flight separator/spectrometer [154, 155], which offers a significant increase in resolving power and a reduction of the measurement time.

In this chapter a novel Phase-Imaging Ion-Cyclotron-Resonance (PI-ICR) detection technique is presented[1]. It can offer a simultaneous increase in resolving power and precision as compared to the ToF-ICR technique. Moreover, the PI-ICR technique is faster thus allowing for the mass measurements on nuclides with shorter half-lives than those which can be measured by means of the time-of-flight detection technique.

In addition to the measurements on short-lived nuclides, with the performance of the new technique presented in this chapter a systematic cross-check of the microcalorimet-

[1] This chapter follows the paper [57], where the author of the thesis made major contributions to the analysis and writing.

ric experiments MARE [25] and ECHo [26] aimed for the determination of the neutrino mass investigating the $^{187}\mathrm{Re} \rightarrow {}^{187}\mathrm{Os}$ β-decay and electron capture in ^{163}Ho can be done (see Sec. 2.3.2 and Sec. 2.3.3, respectively).

5.1 Principles of the Phase-Imaging Ion-Cyclotron-Resonance technique

Similar to the ToF-ICR technique, in the novel PI-ICR technique the mass ratio R is determined via the free cyclotron frequency determination employing Eq. (3.6) and Eq. (4.4), i.e., $\nu_c = \nu_+ + \nu_-$ and $R = M_2/M_1 = \nu_c^1/\nu_c^2$ (see Sec. 4.2). The difference between two methods is that in the phase-imaging technique ν_c is determined by measuring the phases of the magnetron and modified cyclotron ion motion, accumulated after a given period of the excitation-free phase evolution. In the present work two measurement schemes were proposed: 1) independent measurements of ν_- and ν_+, and 2) a direct measurement of ν_c. In case of measurements on isobaric pairs their magnetron frequencies can be considered equal and the determination of the free cyclotron frequency reduces to the determination of the modified cyclotron frequency, what favors the first scheme. The second scheme might become the method of choice in all other cases.
The PI-ICR technique has been implemented at the off-line SHIPTRAP setup (see Sec. 4.4.1) with the modified detection system described in Sec. 5.2. The investigation of the new technique has been performed with $^{133}\mathrm{Cs}^+$ ions and the corresponding approximate eigenfrequencies are presented in Tab. 3.1. Hence, all quantitative examples are given for these ion species and in conformity with the SHIPTRAP performance unless otherwise stated.

5.1.1 Scheme 1: independent measurements of ν_- and ν_+

In scheme 1 the magnetron and modified cyclotron motions are treated in a similar way, thus the subscripts ($\pm$) are omitted unless otherwise specified and both motions and corresponding frequencies are simply called "radial motion" and "radial frequency", respectively. The principle of the measurement of the radial frequency is shown in Fig. 5.1. The ions are assumed to be prepared at the center of the trap (position 1 in Fig. 5.1a) with the FWHM of their initial spatial distribution $2\Delta r$ defined by the previous cooling of the radial motions (see Sec. 5.1.3). Applying a dipolar rf-excitation (see Sec. 4.3.1) with a certain initial phase at the radial frequency $\nu_{\mathrm{rf}} = \nu$, the ions are excited to the average radius r (position 2 in Fig. 5.1a). After a time t of the free evolution in the trap the radial ion motion accumulates a total phase of $\phi + 2\pi n = 2\pi\nu t$ (position 3 in Fig. 5.1a), where ϕ is the polar angle between positions 2 and 3, n is the number of full revolutions the ion performs in the time t, and ν is the radial frequency. Positions 1, 2, and 3 are called the *center*, the *reference* phase and the *final* phase of the radial motion, respectively. In order to determine the number of full revolutions n the

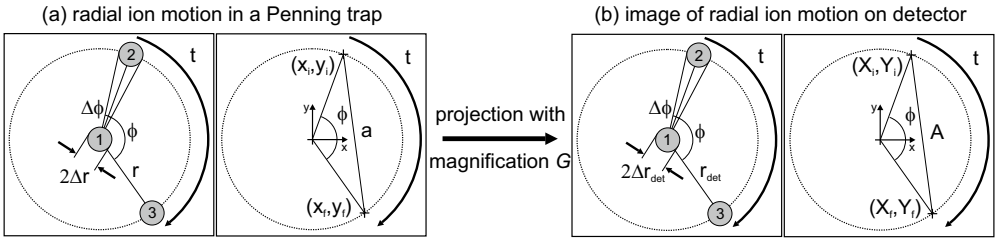

Figure 5.1: Principle of the phase-imaging measurement of the radial ion motions in a Penning trap. The radial ion motion inside the trap (a) is projected onto the position-sensitive detector (b) with certain magnification factor G. Positions 1,2 and 3 in (a) and (b) correspond to the center of the motion, reference and final phases, respectively (see text for details).

ion performs in the time t quick measurement of the radial frequency with a moderate precision by the conventional ToF-ICR technique performed every few days is sufficient due to a high temporal stability of the magnetic field and trap electric potentials.
Introducing the coordinates with uncertainties of the reference and final phases with respect to the center of the trap as $(x_i \pm \delta x_i, y_i \pm \delta y_i)$ and $(x_f \pm \delta x_f, y_f \pm \delta y_f)$ (see Fig. 5.1a), respectively, the radial frequency ν can be written as

$$\nu = \frac{\phi + 2\pi n}{2\pi t}, \text{ with } \begin{cases} \phi = \left|\arctan\left(\frac{y_i}{x_i}\right) - \arctan\left(\frac{y_f}{x_f}\right)\right| \;\Leftrightarrow\; 0 \le \phi \le \pi, \\ \phi = 2\pi - \left|\arctan\left(\frac{y_i}{x_i}\right) - \arctan\left(\frac{y_f}{x_f}\right)\right| \;\Leftrightarrow\; \pi < \phi < 2\pi. \end{cases} \tag{5.1}$$

In order to determine the radial frequencies, the ion motion is projected onto a position-sensitive detector, which is placed on the trap axis (namely z-axis) in the region of weak magnetic field [156]. The ideal projection preserves the angle ϕ while magnifying the image of the ion's relative positions on the detector by a factor G and thus transforming r and $(x \pm \delta x, y \pm \delta y)$ to $r_{\text{det}} = G \cdot r$ and $(X \pm \delta X, Y \pm \delta Y) = G \cdot (x \pm \delta x, y \pm \delta y)$, respectively (Fig. 5.1b). Eq. (5.1) becomes

$$\nu = \frac{\phi + 2\pi n}{2\pi t}, \text{ with } \begin{cases} \phi = \left|\arctan\left(\frac{Y_i}{X_i}\right) - \arctan\left(\frac{Y_f}{X_f}\right)\right| \;\Leftrightarrow\; 0 \le \phi \le \pi, \\ \phi = 2\pi - \left|\arctan\left(\frac{Y_i}{X_i}\right) - \arctan\left(\frac{Y_f}{X_f}\right)\right| \;\Leftrightarrow\; \pi < \phi < 2\pi. \end{cases} \tag{5.2}$$

Excitation-pulse schemes for the measurement of the magnetron and the modified cyclotron frequencies are presented in Fig. 5.2 (left) and (right), respectively. First, an ion of interest is injected into the Penning trap (step 1) with a subsequent dipolar excitation (Sec. 4.3.1) of the radial motion (step 2). Then, the ion spends the time t in the trap accumulating the phase $\phi + 2\pi n$. After that, the ion is ejected and its radial position

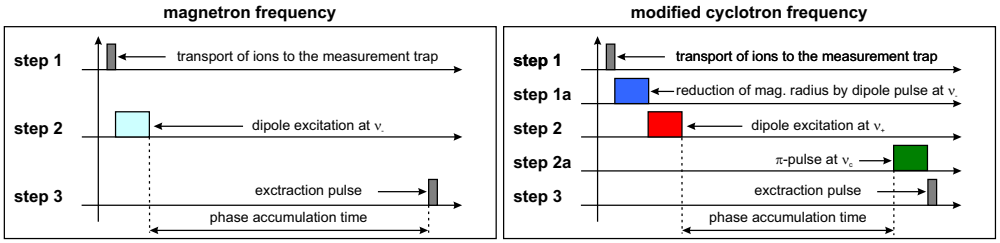

Figure 5.2: Excitation-pulse scheme for the independent measurement of the magnetron (left) and modified cyclotron (right) frequencies. The duration of the pulses can be taken to be as short as the period of the corresponding radial motion. In practice, the minimum duration is given by the amplitude of the pulse one can apply. For details see text.

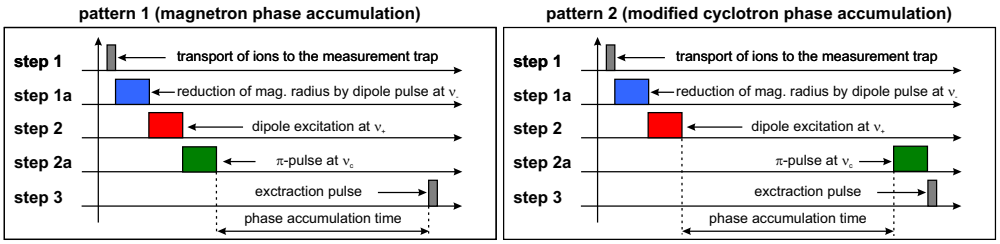

Figure 5.3: Excitation-pulse scheme for the direct measurement of ν_c. Patterns 1 (left) and 2 (right) correspond for the magnetron and modified cyclotron phase accumulation, respectively. The duration of the pulses can be taken to be as short as the period of the corresponding radial motion. In practice, the minimum duration is given by the amplitude of the pulse one can apply. For details see text.

is projected onto the position-sensitive detector (step 3) resulting in the coordinates $(X_f \pm \delta X_f, Y_f \pm \delta Y_f)$, which correspond to the position 3 in Fig. 5.1b. Consequently, the coordinates of the positions 1 and 2 can be obtained by projecting the ion motion onto the detector without excitation and right after the excitation, respectively.
Compared to ν_- (Fig. 5.2 (left)), two intermediate steps are performed for the measurement of the modified cyclotron frequency ν_+ (Fig. 5.2 (right)): First, before exciting the cyclotron motion, the coherent component of the magnetron motion is minimized by a dipolar de-excitation at ν_- (step 1a). Second, before extraction the fast cyclotron motion is converted into the slow magnetron motion by a quadrupolar rf-excitation (see Sec. 4.3.2) at the sideband frequency $\nu_{\mathrm{rf}} = \nu_+ + \nu_-$ (step 2a), which is marked as "π-pulse" in Fig. 5.2 and Fig. 5.3. A direct projection of the modified cyclotron motion is possible but results in a substantial angular spread on the detector due to the time-of-flight distribution of the ions between the trap and the detector (see Fig. 5.5c). The smearing of the time-of-flight peak is caused by the energy distribution of the axial motion in the trap. At SHIPTRAP, e.g., the FWHM of the time-of-flight peak is about a few 100 ns, which is close to the half-period of the modified cyclotron motion of $^{133}Cs^+$ ions (see Tab. 3.1). Note that the conversion of the modified cyclotron into magnetron motion preserves the modulus of the angle between the reference and the final phase of

the corresponding motions while flipping the sign of the angle (see Sec. 5.3.4). The measurement cycles for the magnetron and modified cyclotron frequencies are performed alternately many times until sufficient ion events are acquired in order to determine the free cyclotron frequency ν_c with the aimed precision.

5.1.2 Scheme 2: a direct measurement of ν_c

Scheme 2 allows a direct determination of the free cyclotron frequency ν_c instead of summing the independently measured values of ν_+ and ν_-. The excitation-pulse scheme, presented in Fig. 5.3, consists of two patterns, which differ in steps 3 and 4. In pattern 2 the ion after excitation of its cyclotron motion spends a certain time t_2 in the trap accumulating the modified cyclotron phase $\phi_+ + 2\pi n_+$ and the quadrupolar excitation is applied right before its ejection. In pattern 1 the quadrupolar excitation is applied right after the dipolar excitation of the modified cyclotron motion. The ion is ejected after a certain time t_1 in the trap thus accumulating the magnetron phase $\phi_- + 2\pi n_-$. If $t_1 = t_2 = t$, then the angle ϕ_c between the phase images corresponding to pattern 1 and 2, respectively, is given by

$$\phi_c = 2\pi\nu_c t - 2\pi(n_+ + n_-). \tag{5.3}$$

5.1.3 Comparison of the PI-ICR and ToF-ICR detection techniques

In order to compare the performance of the PI-ICR and ToF-ICR detection techniques, some additional remarks have to be discussed. According to the data obtained in many mass-measurement experiments at SHIPTRAP, the following empirical formula has been found for the estimation of the uncertainty of the cyclotron frequency determination by means of the Ramsey ToF-ICR technique [157]

$$\delta\nu_c \approx \frac{1.6}{t\sqrt{N}} \cdot \frac{\Delta r}{r_-}, \tag{5.4}$$

where N is the number of acquired ions, t is the total excitation time (here $t = \tau_0 + 2\tau_1$, see Sec. 4.3.4) and $2\Delta r$ defines a FWHM of the initial spatial distribution of the ions in the trap.

As it is mentioned in Sec. 4.3.4, even though the Ramsey ToF-ICR technique offers higher resolving power than the standard ToF-ICR technique, a multiple fringe structure of the Ramsey resonance does not allow a veracious resolution of two close masses in the majority of practical cases. Hence, the standard ToF-ICR technique can be considered the method of choice if two masses are to be resolved. The achievable resolving power is then given by [157]

$$\frac{\nu_c}{\Delta\nu_c} \approx 1.1 \cdot \nu_c \cdot t. \tag{5.5}$$

Thus, with the ToF-ICR detection technique one cannot achieve the highest possible

precision and resolving power simultaneously using the same excitation scheme.

Initial spatial distribution of the ions

The initial spatial distribution of the ions is defined by the cooling of the ion motions. Considering the buffer-gas cooling technique, described in Sec. 4.3.3, the probability density function for the energy E of cooled ions is given by the Boltzmann distribution

$$f(E)dE = \frac{1}{kT}\exp\left[-\frac{E}{kT}\right]dE, \tag{5.6}$$

where k is the Boltzmann constant and T is the gas temperature. According to Eq. (3.13a) and Eq. (3.12) the probability density function for the radius of the cooled cyclotron motion is given by

$$f_+(r_+)dr_+ \approx \frac{m\omega_+^2}{kT}\exp\left[-\frac{m\omega_+^2 r_+^2}{2kT}\right]r_+ dr_+. \tag{5.7}$$

The magnetron motion is cooled by a sideband coupling to the modified cyclotron motion (see Sec. 4.3.3). Introducing the relation $T_+ = (\omega_+/\omega_-)T_-$ between the temperatures T_+ and T_- of the cooled cyclotron and magnetron motions, respectively, the probability density function for the radius of the cooled magnetron motion is similar to that of the modified cyclotron motion and is given by

$$f_-(r_-)dr_- \approx \frac{m\omega_+^2}{kT}\exp\left[-\frac{m\omega_+^2 r_-^2}{2kT}\right]r_- dr_-. \tag{5.8}$$

Assuming that the buffer-gas cooling and the sideband cooling do not introduce correlations between the radial motions, the probability $F(r,\phi)$ to find an ion at a particular location (r,ϕ) is given by the convolution

$$F(r,\phi) = \int_{-\infty}^{\infty}\int_{-\infty}^{\infty} f_+(r_+,\phi_+)f_-(r-r_+,\phi-\phi_+)dr_+ d\phi_+. \tag{5.9}$$

It is convenient now to convert Eq. (5.9) to Cartesian coordinates, and with $\sigma = \sqrt{\frac{2kT}{m\omega_+^2}}$ one obtains

$$\begin{aligned} F(x,y) &= \int_{-\infty}^{\infty}\int_{-\infty}^{\infty} f_+(x_+,y_+)f_-(x-x_+,y-y_+)dx_+dy_+ \\ &= \frac{1}{(\pi\sigma^2)^2}\int_{-\infty}^{\infty}\int_{-\infty}^{\infty}\exp\left[-\frac{x_+^2+y_+^2+(x-x_+)^2+(y-y_+)^2}{\sigma^2}\right]dx_+dy_+ \\ &= \frac{1}{\sqrt{2\pi}\sigma}\exp\left[-\frac{x^2}{2\sigma^2}\right]\cdot\frac{1}{\sqrt{2\pi}\sigma}\exp\left[-\frac{y^2}{2\sigma^2}\right] = \frac{1}{2\pi\sigma^2}\exp\left[-\frac{r^2}{2\sigma^2}\right], \end{aligned} \tag{5.10}$$

Thus, the probability density function averaged over a period of the magnetron motion of the cooled ions after their projecting on the x-, y- or r-axis is given by a Gaussian

distribution with a FWHM of $2\Delta r$ given by

$$2\Delta r \approx \frac{2.35}{\pi\nu_+}\sqrt{\frac{kT}{2m}}. \tag{5.11}$$

At SHIPTRAP, $2\Delta r$ corresponds to $\sim 90\mu$m for $^{133}Cs^+$ ions at room temperature.

The performance of PI-ICR in comparison with ToF-ICR

Assuming again the independent measurements of the radial frequencies (Sec. 5.1.1), the resolution $\Delta\nu$ and uncertainty $\delta\nu$ of the radial frequency determination are given by

$$\Delta\nu = \frac{\Delta\phi}{2\pi t} = \frac{2\arcsin\left(\frac{\Delta r}{r}\right)}{2\pi t} \approx \frac{\Delta r}{\pi t r}, \tag{5.12a}$$

$$\delta\nu = \frac{\sqrt{\sum_{i,f}\left[(y\delta x)^2 + (x\delta y)^2\right]}}{2\pi r^2 t}, \tag{5.12b}$$

and with respect to the projections (see Fig. 5.1b)

$$\Delta\nu = \frac{\Delta\phi}{2\pi t} = \frac{2\arcsin\left(\frac{\Delta r_{\mathrm{det}}}{r_{\mathrm{det}}}\right)}{2\pi t} \approx \frac{\Delta r_{\mathrm{det}}}{\pi t r_{\mathrm{det}}}, \tag{5.13a}$$

$$\delta\nu = \frac{\sqrt{\sum\limits_{i,f}\left[(Y\delta X)^2 + (X\delta Y)^2\right]}}{2\pi r_{\mathrm{det}}^2 t}. \tag{5.13b}$$

The difference of the magnetron frequencies of two ion species is much smaller than that of the modified cyclotron frequencies. Hence, the resolving power of the PI-ICR technique is defined by the ability to resolve the phase difference accumulated in a time t for the cyclotron motions of two species:

$$\frac{\nu_c}{\Delta\nu_c} \approx \frac{\nu_+}{\Delta\nu_+} = \frac{\phi + 2\pi n}{\Delta\phi} \approx \frac{\pi\nu_+ t r_{\mathrm{det}+}}{\Delta r_{\mathrm{det}+}} = \frac{\pi\nu_+ t r_+}{\Delta r_+}. \tag{5.14}$$

Dividing Eq. (5.13a) by Eq. (5.5), one can estimate the gain in resolving power for the PI-ICR detection technique in comparison with the standard ToF-ICR technique:

$$\text{gain in resolving power} \approx \frac{0.9\pi r_+}{\Delta r_+}. \tag{5.15}$$

For a typical final radius of $r_+ = 0.7$ mm and a radial spread of $\Delta r_+ = 45$ μm, the improvement factor is about 40.
The coordinates of the center and the reference phase can be considered constant due to the absent of the free evolution period in their determination. Thus, it is sufficient

to measure them just once every several days and the determination of the radial frequency ν reduces to the measurements of the final phases for the magnetron and modified cyclotron motions. If the spatial spread is the same, i.e., $\delta X_f \approx \delta Y_f = \delta A$, what is fulfilled in practice, Eq. (5.13b) reduces to

$$\delta\nu = \frac{\delta A}{2\pi r_{\mathrm{det}} t}. \tag{5.16}$$

The uncertainty in the ν_c determination is defined by the uncertainties of ν_+ and ν_- as $\delta\nu_c = \sqrt{\delta\nu_+^2 + \delta\nu_-^2}$. In the ideal case $r_{\mathrm{det}+} = r_{\mathrm{det}\text{-}} = r_{\mathrm{det}}$, $t_+ = t_- = t$ and $N_+ \simeq N_- \simeq N/2$, where N_+ and N_- are the number of ions detected during a measurement of the modified cyclotron and magnetron frequencies, respectively, and N is the total number of detected ions. Hence, the uncertainties $\delta\nu_+$ and $\delta\nu_-$ can be considered similar. Assuming that $\Delta r_{\mathrm{det}+} \approx \Delta r_{\mathrm{det}\text{-}} = \Delta r_{\mathrm{det}}$, the uncertainty $\delta\nu_c$ is then written as

$$\delta\nu_c = \sqrt{2}\frac{\delta A}{2\pi r_{\mathrm{det}} t} = \frac{1}{\pi t\sqrt{N}}\frac{\Delta r_{\mathrm{det}}}{r_{\mathrm{det}}} = \frac{1}{\pi t\sqrt{N}}\frac{\Delta r}{r}. \tag{5.17}$$

Now one can compare Eq. (5.17) and Eq. (5.4), which define the precision of the PI-ICR and Ramsey ToF-ICR detection techniques, respectively:

$$\frac{(\delta\nu_c)_{\text{ToF-ICR}}}{(\delta\nu_c)_{\text{PI-ICR}}} \cong 5. \tag{5.18}$$

Since the precision (Eq. (5.17)) is inversely proportional to the square root of the number of detected ions, Eq. (5.18) implies the PI-ICR technique to be a 25-times faster method as compared to the Ramsey ToF-ICR technique. If the measurement of the free cyclotron frequency can be reduced to the measurement of the modified cyclotron frequency, then a 10-fold gain in precision can be achieved. As for the second measurement scheme (Sec. 5.1.2), a gain 5 in precision and a gain of 40 in resolving power are also possible.

5.2 SHIPTRAP setup modifications for PI-ICR

As it is mentioned above, the PI-ICR detection technique has been implemented at SHIPTRAP and the investigation has been performed with $^{133}Cs^+$ ions produced by a surface ion source [158]. The major change in a setup as compared to the description given in Sec. 4.4.1 is a position-sensitive MCP detector which has replaced an ordinary MCP detector. In addition, the control system of the experiment has been modified in order to employ the functional of the new detection system.
In this investigation voltage settings of the extraction optics, which define the drift region, were different for the ToF-ICR and PI-ICR techniques (see Tab. 5.1 and Fig. 5.4). The ToF-ICR settings were chosen to provide a sufficient adiabatic conversion of the radial into axial ion energy by slowing down the ions in the strong gradient of the magnetic field with a subsequent fast acceleration in the region of the weak magnetic

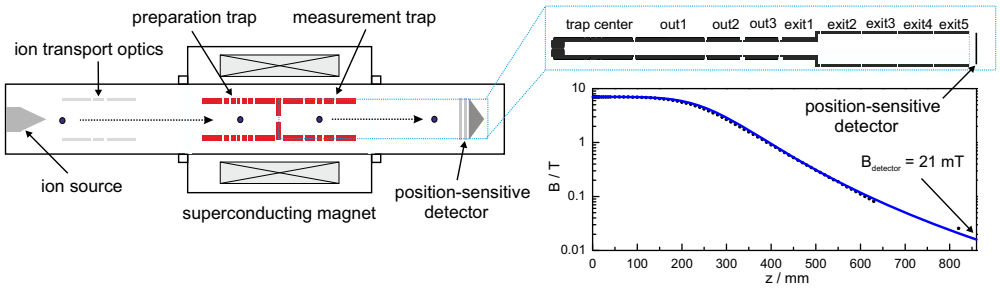

Figure 5.4: (left) Illustration of the off-line SHIPTRAP setup for PI-ICR. The Cs^+ ions from a surface ion source are guided by ion transport optics towards the Penning traps. After the mass-selective buffer-gas cooling and centering in the preparation trap, the ions are moved to the MT, where the cyclotron frequency measurements are performed. (right-top) The sections of the measurement trap and drift region. (right-bottom) The magnetic-field strength B along the z-axis of the SHIPTRAP magnet. The points are measured data. The line is an empirical fit to the data (see next section).

Trap/drift electrode	ToF-ICR	PI-ICR
ring	0	0
correction	4.8	4.8
endcap	41	41
out1	–35	–1300
out2	–3.4	–1300
out3	–35	–1300
exit1	–200	–1300
exit2	–200	–1300
exit3	–200	–1300
exit4	–600	–1300
exit5	–600	–1300

Table 5.1: Voltage settings for the trap electrodes and extraction ion optics used with the ToF-ICR and PI-ICR techniques. The values for the correction and endcap electrodes correspond to the ion-trapping regime. For ion ejection they are switched to about –50 V.

field in order to compress their time-of-flight distribution. In contrast, voltage settings for the PI-ICR technique were chosen in order to provide a very fast ejection of the ions from the region with strong magnetic field to minimize the systematic effects,

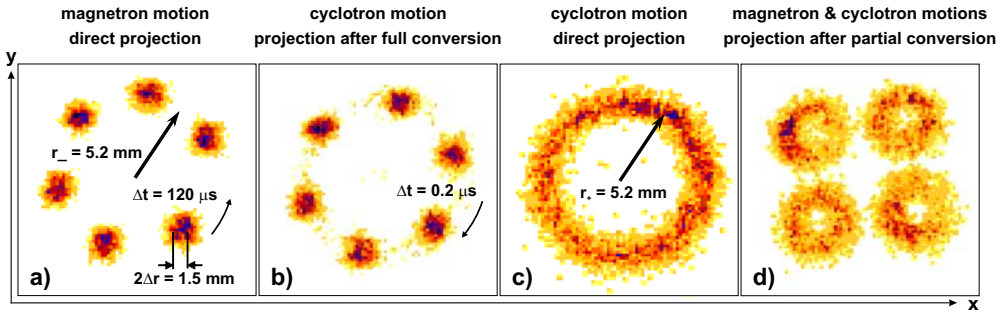

Figure 5.5: Measured projections of the position of $^{133}Cs^{+}$ ions for several phases **a)** of the magnetron motion and **b)** of the cyclotron motion after its full conversion. **c)** Direct projection of the cyclotron motion with a certain phase onto the detector. **d)** Direct projection of the radial motion with non-zero magnetron and cyclotron radii for four phases of the magnetron motion. See text for details.

discussed in the next section. The magnification factor G introduced in Sec. 5.1.1 is defined among other effects by these settings (see Sec. 5.3.1).
In the PI-ICR technique data are represented as 3D-histograms of the projections of the radial ion motion (or simply images). In Fig. 5.5 the results of the data recorded for $^{133}Cs^{+}$ ions with the settings from Tab. 5.1 are presented. The acquired images correspond to the phase projections of the magnetron and cyclotron motion. The radii of both motions were about 0.26 mm. The different phase spots correspond to different projection schemes and different phase-accumulation times ranging from 0 to the period of the corresponding radial motion. The spatial spread in the trap was ~ 42.5 μm.

5.2.1 Delay-line position-sensitive detector

In the novel technique a key component is a position-sensitive detector. Within the present work an MCP detector with a delay-line anode (DLD40) from RoentDek GmbH [159, 160] was implemented at SHIPTRAP. It is worth mentioning that the first attempts to investigate the radial ion motion at SHIPTRAP with such a detector

active diameter	42 mm
channel diameter	25 μm
open area ratio	> 50 %
rate capability	10^6 events/s
position resolution	70 μm
maximal ambient magnetic field	a few 10 mT
time resolution	~ 10 ns

Table 5.2: Specifications of the delay-line detector DLD40 from RoentDek GmbH.

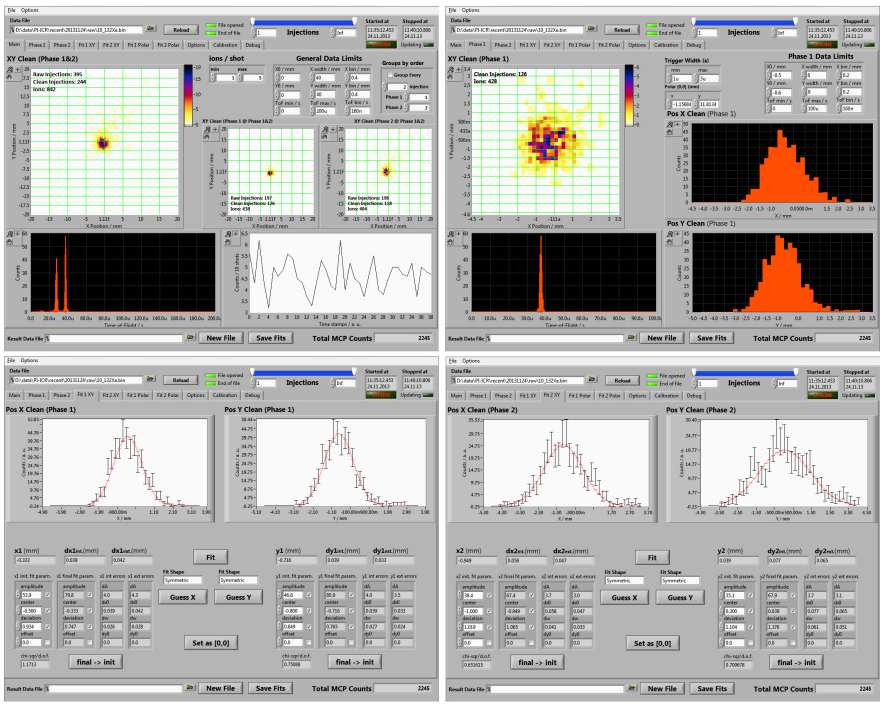

Figure 5.6: Screenshots of the new data analysis system. Various information for one data point consisting of two phase projections of the magnetron and cyclotron ion motions is shown. In the main window (top-left) the phases of two motions can be monitored together with the averaged count rate and aggregate time-of-flight spectrum. Each phase can be monitored separately (top-right) with the projections of the corresponding phase spot in Cartesian coordinates and a fit of each projection is possible (bottom).

were undertaken already a few years ago [156].
The delay-line anode consists of two wire pairs wound in x- and y-directions biased to 300 V with respect to the MCP back-plate. The electron avalanche caused by an ion impact induces an electric signal on the anode wire, which propagates along the delay-line wires. The difference in signal propagation time to each end of the delay-line is converted into the x- and y-coordinates of the impact position with a spatial resolution for a single event of typically 70 μm. The technical specifications of the detector used in the present work are given in Tab. 5.2.
The large active diameter of about 42 mm allows large magnifications in the projection of the ion motion (see next section). The detector does not work in magnetic fields stronger than a few 10 mT. This imposes constraints on the distance from the trap center where the detector can be installed (see Fig. 5.4) and sets the scale of the electrostatic ion optics used to project the ion motion onto the detector. Note that MCP models capable of working in much stronger magnetic fields are also commercially available.

5.2.2 Data acquisition and analysis system

The delay-line detector was supplied together with a data acquisition system consisting of the time-to-digital converter TDC8HP and the CoboldPC software [160]. TDC8HP is the 8-channel pci-card-based converter which provides a 25 ps time resolution. It is capable to record up to 5×10^5 particles/s within a time window of 418 μs for ~ 2 hours.
Since the original data acquisition software did not provide proper data analysis functionality, a new software was developed within the present work. Screenshots of the front panels of the new program are presented in Fig. 5.6. The program serves first for the processing of raw data acquired by TDC8HP. It allows a calibration of the detection system with respect to the detector size and lengths of the delay lines. The data analysis part of the program comprises sorting of the data by many user-defined criteria and independent fits of the projections of the radial motions in Cartesian and polar coordinates by means of the Maximum-Likelihood estimation method with the automatic pre-processing of the results.

5.3 Investigation of the systematic effects

In the present chapter the main research work was dedicated to the development of the PI-ICR detection technique and to a careful investigation of the systematic effects specific to this technique, which limit the achievable resolving power and precision. This section presents the results of the investigation of these effects within the framework given above.
The systematic effects can be sorted into three groups:

- Effects which distort the projection of the ion motion onto the detector. These effects occur from mechanical imperfections like, e.g., misalignment of the trap and magnetic field axes or a tilt of the detector plane with respect to the symmetry axes of the trap electrodes.
- A non-simultaneous measurement of the radial frequencies introduces an error in a cyclotron frequency determination caused by the fluctuations of the electric and magnetic fields.
- Effects resulting in a smearing of the image such as damping of the radial ion motions by residual gas or a non-efficient conversion of the radial motions.

The most significant systematic shifts are summarized in Tab. 5.3 at the end of this section.

5.3.1 Distortion of the orbit image

A certain angular χ and/or linear b displacement between the symmetry axes of the magnetic field and the trap electrodes as well as a finite angle δ between the detector

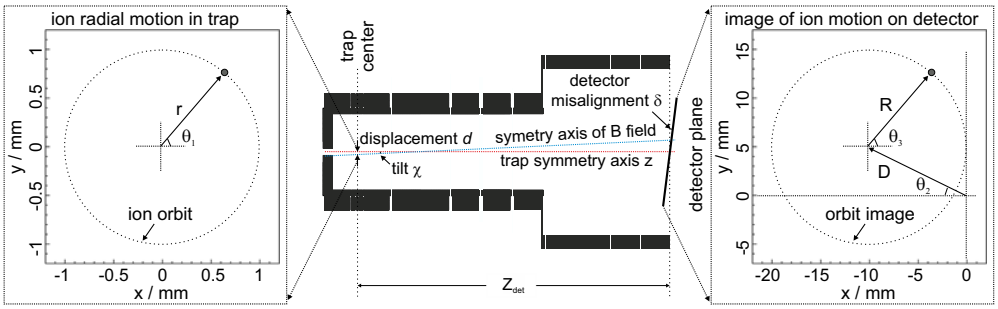

Figure 5.7: A projection of the ion's radial position (r, θ_1) in the trap onto the detector in the presence of an angular χ and linear b displacement of the magnetic field and trap axes results in a displacement of the orbit-image center by (D, θ_3) with respect to the trap axis. Also the orbit-image shape can be distorted. $(r_{\mathrm{det}}, \theta_2)$ are the polar coordinates of the ion's position on the detector with respect to the ion-image center.

plane and the plane perpendicular to the symmetry axis of the trap electrodes (see Fig. 5.7), can result in a distortion of the ion-orbit projection (orbit image) and the movement of the center of the orbit image with respect to the symmetry axis of the detector.

The projection of a certain point in the MT with the coordinates (r, θ_1) to the corresponding point on the detector with the coordinates $(r_{\mathrm{det}}, \theta_2)$ can be described by a projection operator P

$$(r_{\mathrm{det}}, \theta_2) = P \cdot (r, \theta_1). \tag{5.19}$$

The operator P has a simple analytical form when the ions follow the magnetic field lines, i.e., when the ions move in an electric field-free region with low velocity. In practice, such a situation is realized when all drift electrodes (*out*1 to *exit*5, see Fig. 5.4) are set to the same small voltage of a few volts, that is, when the drift electrodes produce a single electric field-free drift region.

If only a magnetic field with axial symmetry is present, the transformation of the coordinates (r, θ_1) to $(r_{\mathrm{det}}, \theta_2)$ is given by

$$\begin{aligned} r_{\mathrm{det}} &= G_B \cdot r, \\ \theta_2 &= \theta_1, \end{aligned} \tag{5.20}$$

where G_B is the magnification in the absence of the electric field for ions which move with low velocity. G_B is in general a function of r. The magnification in the presence of the electric field is designated as G.

From Gauss's flux law, the magnification G_B is given by

$$G_B = \frac{r_{\mathrm{det}}}{r} = \sqrt{\frac{B_z(r,0)}{B_z(r_{\mathrm{det}}, z_{\mathrm{det}})}}, \tag{5.21}$$

where $B_z(r,0)$ and $B_z(r_{\mathrm{det}}, z_{\mathrm{det}})$ are the axial components of the magnetic field in the

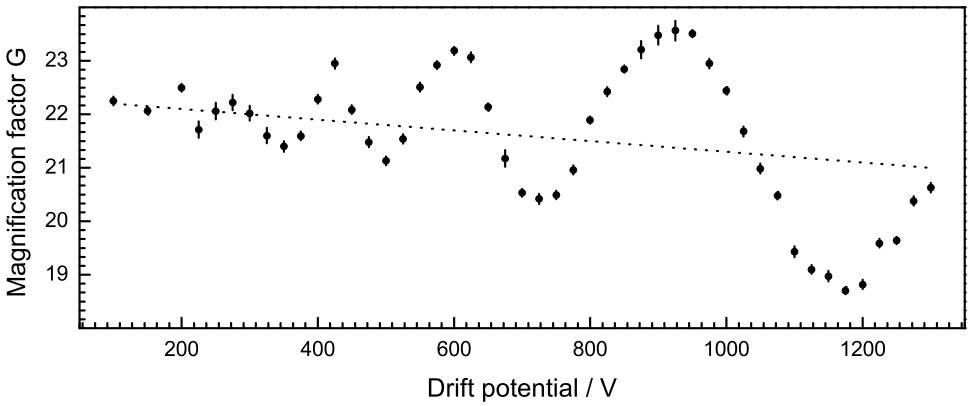

Figure 5.8: The magnification factor G measured at SHIPTRAP versus the drift voltage. The initial radius of the ion orbit in the trap was ∼0.55 mm. The dotted line is the average magnification G.

MT at the radius r and at the detector axial position z_{det} at the radius r_{det}, respectively. In order to estimate G_B for the SHIPTRAP magnet, the axial component $B_z(r_{\mathrm{det}}, z)$ of the magnetic field $\boldsymbol{B}$ was computed from the axial component of the magnetic field $B_z(0, z)$ measured along the symmetry axis z of the TRIGATRAP [161] magnet, which is identical in geometry and field strength to the SHIPTRAP magnet (see Fig. 5.4):

$$B_z(r_{\mathrm{det}}, z) \approx B_z(0, z) - \frac{r_{\mathrm{det}}^2}{4} \cdot \left.\frac{\partial^2 B_z}{\partial^2 z}\right|_{(0,z)}, \tag{5.22}$$

where

$$B_z(0, z) \approx \frac{7T}{1 + (\frac{(z/[\mathrm{mm}])+50}{330})^6}. \tag{5.23}$$

The origin of the z-axis is in the center of the MT.
For the detector position at a distance of $z_{det} = 860$ mm from the trap center the calculation yields

$$G_B \approx 21 \cdot (1 + 10^{-8} \cdot (r_{\mathrm{det}}/[\mathrm{mm}])^2) \approx 21. \tag{5.24}$$

Thus, the magnification factor G_B can be considered constant for $r_{\mathrm{det}} < 20$ mm (detector radius). Although the real magnification can slightly differ from the calculated one due to the deviation between the magnetic fields of the SHIPTRAP and TRIGATRAP magnets, the exact absolute values are not relevant for radial frequency measurements. An angular or a linear displacement between the axes affects the position and the shape of the orbit image. In the case of an angular displacement, the center of the image on the detector is located at the cross-point of the symmetry axis of the magnetic field with the detector plane. In the presence of a linear displacement, the symmetry axis of the magnetic field is replaced by the magnetic field line situated at the displacement b from the symmetry axis. Thus, the position of the orbit-image center D with respect

to the trap electrodes axis can be obtained from

$$\begin{aligned} D &= z_{det} \cdot \chi \cdot 2\pi/360 \\ &\approx 15 \cdot \chi \approx 0.7 \cdot G_B \cdot \chi \quad \text{- angular displacement,} \\ D &= (G_B - 1) \cdot b \qquad\qquad \text{- linear displacement,} \end{aligned} \tag{5.25}$$

where χ is given in degrees, z_{det} and b are expressed in mm.
The movement of the image center has no impact on the frequency determination, whereas the modification of the image shape certainly does. Let us consider first the impact of the angular displacement χ on the orbit image. If one considers the angular displacement as the inclination of the radial ion motion and the detector planes by χ with respect to the axis of the magnetic field, then it becomes clear that the orbit image remains circular with its center shifted by D as given in Eq. (5.25) with respect to the trap electrodes' symmetry axis and hence the detector center.
In order to determine the distortion of the orbit image caused by a linear displacement b, one has to calculate the action of the projection operator on the ion's orbit whose center has an offset of b with respect to the symmetry axis of the magnetic field:

$$r_{\text{det}} = G_B \cdot \left(b \cdot \cos\theta_1 \pm \sqrt{r^2 - b^2 \cdot \sin^2\theta_1} \right), \tag{5.26}$$

where the expression in brackets is the equation of a circle with a center shifted by b along the axis x. (r, θ_1) is the polar coordinate of a generic point on the circle. Since G_B is in fact a constant, the linear displacement keeps the orbit image circular.
Fig. 5.8 shows the measured magnification G as a function of the drift voltage for an ion-orbit radius of 0.55 mm. The increase of the drift voltage up to -1300 V results in a slight decrease of the average magnification G (dotted line) from 22 to about 21. The beating of the magnification G is due to the fact that the ion orbits around the magnetic-field lines. The larger the ion velocity, the larger the amplitude and the period of the beating.
For the presently used detector the optimal magnification factor can be considered to be about ten. The present magnification factor G of about 20 does not allow a complete projection of all phases onto the detector with radius of 21 mm if the radius of the radial motion exceeds 1 mm. Nevertheless, it does not affect the radial frequency measurements. To optimize the SHIPTRAP magnification factor the detector must be moved by 20 cm towards the MT into the region where the magnetic field strength is about 70 mT. The presently used model of the MCP detector would not work properly at this field strength. At present, at SHIPTRAP the drift voltage is set to about -1300 V. This value is considered optimal for the projection of the ion motion onto the detector, since the ions are fast enough to minimize the effect of the surface charges on the electrodes, and the voltage is still low enough to avoid problems with electric discharges during the switching of the voltages applied to the electrodes in the trap region.
The inclination of the detector symmetry axis with respect to the symmetry axis of the

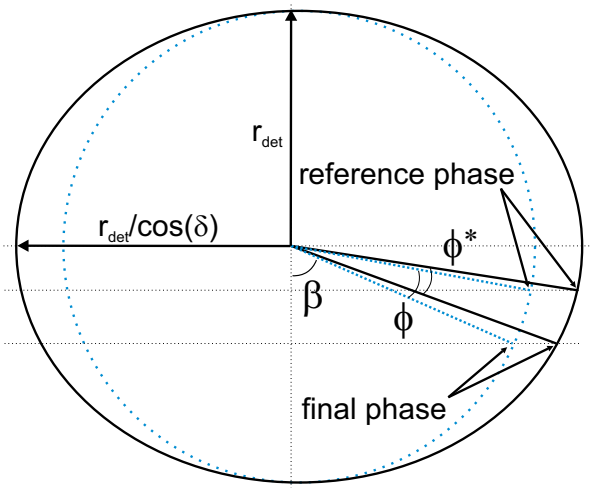

Figure 5.9: Circular (blue dashed line) and elliptical (black solid line) orbit images which correspond to the undistorted and distorted projection of the ion orbit, respectively. The distortion is mainly caused by the angular misplacement δ of the detector with respect to the trap axis. ϕ and ϕ^* are the real and visible angles between the reference and the final phases, respectively. β is the polar coordinate of the real final phase on the detector.

trap electrodes by an angle δ results in an ellipticity of the orbit image. The ratio of the major to the minor radius $e = r_{\mathrm{det}}^{\mathrm{max}}/r_{\mathrm{det}}^{\mathrm{min}}$ of the orbit image (distortion factor) is equal to $1/\cos(\delta)$. With a proper alignment of the detector the angle δ can be made smaller than 1°. In this case, e will not exceed 1.00015.
The distortion introduces no error into the determination of the radial frequency, if the positions of the reference and the final phase spots are the same, i.e., the accumulated phase of the radial motion is equal to the integer number of the radial motion periods. Due to the temporal instability of the trapping voltage the angle ϕ can change over one day of measurements with SHIPTRAP within the range of ±10°. The absolute error of the radial-motion frequency caused by the distortion of the orbit image is given by (see Fig. 5.9):

$$\Delta\nu = \nu - \nu^* = \frac{\phi - \phi^*}{2\pi t} = \frac{\phi - [\arctan(\tan(\beta+\phi)/\cos\delta) - \arctan(\tan\beta/\cos\delta)]}{2\pi t}, \tag{5.27}$$

where ϕ, ν and ϕ^*, ν^* are the angle and radial frequency determined from the undistorted and distorted orbit images, respectively, β is the polar coordinate of the real final phase on the detector, and t is the phase-accumulation time.
For $\phi = 10°$ and $\delta = 1°$, $\Delta\nu/[\mathrm{Hz}]$ is smaller than $5 \times 10^{-6}[\mathrm{s}]/t$. Thus, the relative error in the determination of ν_c for $^{133}Cs^+$ ions (see Tab. 3.1) is well below $10^{-11}[\mathrm{s}]/t$, and hence can be neglected.

5.3.2 Error in the frequency determination due to a non-simultaneous measurement of the reference and final phases

The position of the reference phase is not sensitive to fluctuations of the radial frequency value. Thus, it is sufficient to measure it once a day with high precision. However, this is correct only when the duration of the dipole-excitation pulse, which defines the reference phase, is zero (see Fig. 5.2), and thus the amplitude of the excitation pulse becomes infinite. If the excitation pulse has a finite duration $t_{\rm ex}$, then the position of the reference phase changes with time mainly due to the fluctuations of the trapping voltage. Assuming that the position of the reference phase is measured twice a day, the corresponding radial frequency between these measurements changes by $\Delta\nu$, which results in a change of the angular position of the reference phase $\Delta\phi$ by

$$\Delta\phi = 2\pi t_{ex}\Delta\nu. \tag{5.28}$$

Thus, the error introduced by this to the determination of the radial frequency $\delta\nu$ is given by

$$\delta\nu = \frac{t_{\rm ex}}{t}\Delta\nu, \tag{5.29}$$

where t is the phase-accumulation time. At present, at SHIPTRAP the daily fluctuation of the radial-motion frequency due to the fluctuations of the trapping voltage $\Delta\nu_U$ does not exceed 100 mHz (see next section, Fig. 5.10). The minimal pulse duration of the magnetron excitation which can be set is about 0.75 ms (one period of the magnetron motion). The cyclotron excitation pulse can be set as short as 100 μs – its duration is mainly limited by the maximal voltage the rf-generator can provide. Thus,

$$\frac{\delta\nu}{[Hz]} < \frac{t_{\rm ex}}{t}\frac{\Delta\nu_U}{[Hz]} \approx \frac{7.5\cdot 10^{-5}[s]}{t}, \tag{5.30}$$

where $\delta\nu$ and t are given in Hz and s, respectively. Such a shift can be neglected. Furthermore, if the reference phases of the cyclotron and magnetron motions are measured simultaneously, then according to Eq. (5.29) the errors introduced by the fluctuation of the trapping voltage to the determination of the magnetron and cyclotron frequencies cancel each other. In this case, the determination of the cyclotron frequency ν_c is not affected by the fluctuations of the trapping voltage.
The second important factor which affects the determination of the cyclotron frequency ν_c is the temporal instability of the magnetic field. At SHIPTRAP the typical daily fluctuation of the cyclotron frequency $\Delta\nu_B$ does not exceed 10 mHz due to an active stabilization system (see Sec. 4.4.1). Thus,

$$\frac{\delta\nu}{[Hz]} < \frac{t_{ex}}{t}\frac{\Delta\nu_B}{[Hz]} \approx \frac{7.5\cdot 10^{-6}[s]}{t}. \tag{5.31}$$

For a phase-accumulation time of 1 s the relative frequency shift $\delta\nu/\nu_c$ for $^{133}Cs^+$ ions is smaller than 5×10^{-11}, and hence can be neglected.

5.3.3 Effects which result in a smearing of the phase spot on the detector

The most significant effects which can result in an increase of the spread of the phase spots on the detector are temporal instabilities of the radial ion frequencies due to a fluctuation of the trapping voltage and a damping of the radial ion motions in the Penning trap by residual gas.
If the phase-accumulation time of ions in the measurement trap is t_0, then the values for the radial frequencies measured at time t are given by

$$\overline{\nu}_+(t) \approx \nu_c - \frac{1}{4\pi d^2} \cdot \frac{1}{B} \cdot \frac{\int_t^{t+t_0} U(t')dt'}{t_0} = \nu_c - \frac{1}{4\pi d^2} \cdot \frac{1}{B}\overline{U}(t,t_0), \tag{5.32a}$$

$$\overline{\nu}_-(t) \approx \frac{1}{4\pi d^2} \cdot \frac{1}{B} \cdot \frac{\int_t^{t+t_0} U(t')dt'}{t_0} = \frac{1}{4\pi d^2} \cdot \frac{1}{B}\overline{U}(t,t_0), \tag{5.32b}$$

where $\overline{U}(t,t_0)$ is the trapping voltage at time t averaged for t_0. The instability of the magnetic field in time has by far a lower impact on the frequency and thus is neglected here.
We introduce the terms “fast fluctuations” and a “slow drift” of the trapping voltage. By “fast fluctuations” we mean the component of the temporal change of the trapping voltage which is averaged out by integration over the phase-accumulation time t_0. The function $\overline{U}(t,t_0)$ describes the “slow drift” of the trapping voltage. This distinction of the temporal changes of the trapping voltage in “fast fluctuations” and a “slow drift” depends on the phase-accumulation time t_0. It is important to minimize the “slow drift”. The “fast fluctuations” of the trapping voltage are by far a less critical parameter.
The “slow drift” results in an angular smearing of the phase spot on the detector and thus limits the maximal achievable resolving power and precision. If the total acquisition time of one phase spot is t_m, then the angular smearing of the image spot can be characterized by the standard deviation of the angular distribution of the ions in the image spot and expressed by

$$\delta\phi = \frac{1}{t_m}\sqrt{\int_0^{t_m} \left(\phi - \overline{\phi}\right)^2 dt} \tag{5.33}$$

where

$$\phi = \frac{t_0}{2d^2B} \cdot \overline{U}(t,t_0) + \text{Const}, \tag{5.34a}$$

$$\overline{\phi} = \frac{1}{t_m}\int_0^{t_m} \phi dt = \frac{t_0}{t_m} \cdot \frac{1}{2d^2B} \cdot \int_0^{t_m} \overline{U}(t,t_0)dt + \text{Const}. \tag{5.34b}$$

The subscripts (–) and (+) are omitted since the formulas are valid for both radial motions. Substituting Eq. (5.34a) into Eq. (5.34b) the following final expression for $\delta\phi$ can be obtained

$$\delta\phi = \frac{1}{2d^2B} \cdot \frac{t_0}{t_m} \sqrt{\int_0^{t_m} \left(\overline{U}(t,t_0) - \frac{1}{t_m} \cdot \int_0^{t_m} \overline{U}(t',t_0)dt' \right)^2 dt}. \tag{5.35}$$

The negative effect of the smearing on the resolving power of the method becomes significant when $\delta\phi$ exceeds the angular width of the image spot given by Eq. (5.13a):

$$\arcsin\left(\frac{\Delta r_{\mathrm{det}}}{r_{\mathrm{det}}}\right) < \frac{1}{4d^2B} \cdot \frac{t_0}{t_m} \sqrt{\int_0^{t_m} \left(\overline{U}(t,t_0) - \frac{1}{t_m} \cdot \int_0^{t_m} \overline{U}(t',t_0)dt' \right)^2 dt}. \tag{5.36}$$

This expression can be generalized as

$$r_{\mathrm{det}} \cdot t_0 > f(t_m), \tag{5.37}$$

where $f(t_m)$ is a function which depends on the total acquisition time t_m. Thus, the degree of the smearing is defined by the product of the phase-accumulation time and the radius of the radial motion. For a given phase-accumulation time the radius of the radial motion must be decreased if the smearing of the image spot is to be reduced. But, this results in a decrease of the resolving power and hence the precision of the method. Thus, the fluctuations of the trapping voltage limit the achievable resolving power and precision of the method.

Fig. 5.10 shows the absolute drift of the magnetron frequency of $^{133}Cs^+$ ions (left ordinate) and relative drift of the trapping voltage $\overline{U}(t,t_0)$ (right ordinate) vs. time measured at SHIPTRAP for a phase-accumulation time $t_0 = 0.5$ s and a magnetron radius $r_- = 0.9$ mm. The maximal daily drift of the magnetron and hence modified cyclotron frequency is smaller than 100 mHz. A typical FWHM angular width expressed in terms of frequency for the magnetron-image spot for $t_0 = 1$ s and magnetron radius of 1.0 mm is about 20 mHz. Thus, an hour's measurement does not result in a substantial smearing of the image spot and hence the drift of the trapping voltage on this time scale does not significantly reduce the resolving power. For much shorter phase-accumulation times of, e.g., 0.1 s a day's measurement does not result in an increase of the image-spot size. The drastic change of the magnetron frequency between hours 5 and 7, and 16 and 17 can be explained by a sudden change of the ambient temperature in the experimental hall due to, e.g., the opening of the hall entrance gate. The relatively high stability of 20 mHz in the time intervals between hours 1 and 6, and 7 and 10 is due to a relatively constant hall temperature. Thus, enclosing the trapping-voltage power supplies in a simple insulated box should reduce the daily magnetron frequency drift to a 20 mHz-level.

Another effect which modifies the radial motions is ion collisions with residual gas atoms in the trap. The ion interaction with the gas results in (1) a damping of the radial motions and in (2) a smearing of the image spot. Note that a damping of the

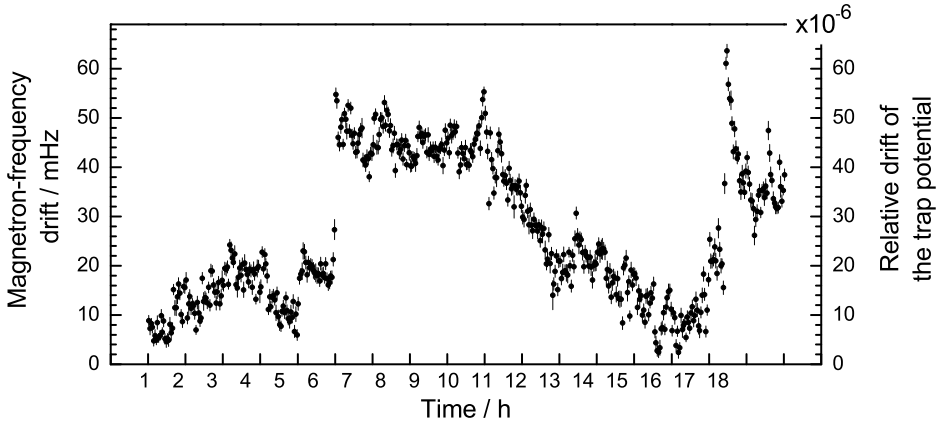

Figure 5.10: The magnetron frequency drift of $^{133}Cs^{+}$ ions (left ordinate) and relative drift of the trapping voltage $\overline{U}(t, t_0)$ (right ordinate) measured over a day at SHIPTRAP for a phase-accumulation time $t_0 = 0.5$ s and a magnetron radius $r_- \approx 0.9$ mm. For details see text.

magnetron motion results in the increase of the magnetron radius due to its metastable nature.

The residual gas composition is altered compared to a normal UHV system by helium atoms which enter the measurement trap from the purification trap through a pumping barrier. Among the restgas constituents water molecules provide the largest damping of the ion motion. Thus, in the following by residual gas water molecules are understood. The helium partial pressure in the measurement trap is about 10^{-7} mbar [162]. The residual-gas pressure after weeks of pumping of the trap volume could be still on a rather high level of 10^{-7} mbar, taking into account that the trap chamber can usually not be baked out.

The average number of ion collisions with residual-gas molecules during the phase-accumulation time t can be estimated by dividing the total distance the ions travel in the trap by their mean free path. A singly charged ion with mass number 133 which performs a magnetron or cyclotron motion with radius 1 mm travels about 8 m and 5 km in 1 s, respectively. The mean free path of these ions in air at 10^{-7} mbar is a few km, whereas the mean free path of these ions in helium at 10^{-7} mbar exceeds ten km. Thus, several conclusions can be drawn. First, the damping and thus smearing of the magnetron motion is negligible even in air at 10^{-7} mbar. Second, as soon as the residual-gas pressure drops well below 10^{-8} mbar the scattering of the ions can be neglected completely for phase accumulating times below 1 s. Third, even at quite a high partial air pressure of 10^{-7} mbar the ions which perform a cyclotron motion just undergo a few collisions.

Considering the situation when the ions perform a pure cyclotron motion and undergo a single elastic collision with residual-gas molecules or helium atoms at rest, a collision results in a decrease of the ion velocity and in a change of the direction of the ion motion.

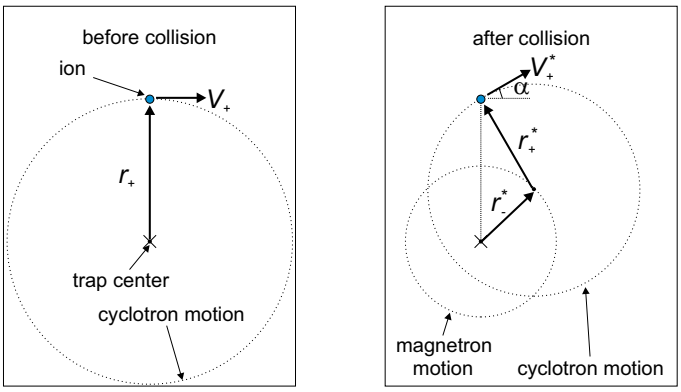

Figure 5.11: Effect of an ion collision with a residual-gas atom on the radial ion motion. r_+ and r_+^* are the cyclotron radii before (left) and after (right) the collision, respectively. r_-^* and α are the magnetron radius after the collision and the scattering angle, respectively. V_+ and V_+^* are the ion velocity before and after the collision, respectively.

This in turn leads to a decrease of the cyclotron motion radius and an increase of the magnetron motion radius of the ions. The conversion to the magnetron motion is the reason for the smearing of the cyclotron-motion image. The change of the magnetron and cyclotron radii can be derived from Fig. 5.11.
In Fig. 5.11 r_+ and r_+^* are the radii of the cyclotron motion before and after the collision, respectively, r_-^* is the magnetron radius after the collision, α is the scattering angle, V_+ and V_+^* are the velocities of the ion before and after the collision, respectively. The magnetron radius r_-^* after the collision is given by

$$r_-^* = \sqrt{(r_+)^2 + (r_+^*)^2 - 2r_+ r_+^* \cos\alpha}. \tag{5.38}$$

Assuming the collision of two hard spheres, the scattering of the ions with mass 133 u on residual-gas molecules is isotropic with a maximal scattering angle of about 10°. Projected onto the radial plane the distribution of the scattered ions as a function of the scattering angle is not isotropic anymore, but peaks at a scattering angle of zero. Thus, for simplicity we assume that the ions after scattering just lose their energy without changing the movement direction in the radial plane. Then, Eq. (5.38) reduces to

$$r_-^* = r_+ - r_+^* = r_+ \cdot \left(1 - \frac{r_+^*}{r_+}\right) = r_+ \cdot (1-k). \tag{5.39}$$

Thus, in order to estimate the average magnetron radius of the ion after a collision, one just needs to estimate the damping factor k of the cyclotron motion.
The damping factor k can be calculated by considering the effect of the residual gas or helium on the ions as a drag force counteracting the ion motion. One can introduce the damping constant γ_+ according to Eq. (4.22) as [113, 114]

$$\gamma_+ \cong \frac{1}{2m}\gamma. \tag{5.40}$$

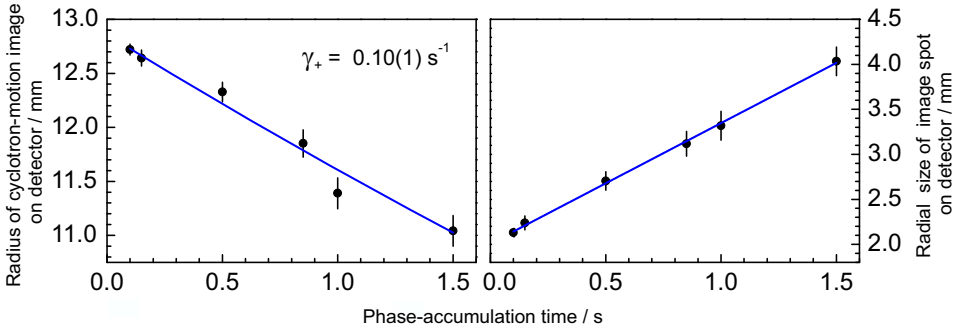

Figure 5.12: Radius of the cyclotron-orbit image (left) and the radial size of the image spot (right) versus the phase-accumulation time. The undamped image-radius is about 12.7 mm, which corresponds to the ion's cyclotron radius in the MT of about 0.60 mm. The blue lines are the exponential fits to the data.

where m is the mass of the ion. The relation between the damping factor k and the damping constant γ_+ is given by $k = \exp(-\gamma_+ t)$. The reduced mobility of singly charged Cs ions of mass 133 u in water vapour and helium is about 0.7×10^{-4} $m^2 s^{-1} V^{-1}$ and 20×10^{-4} $m^2 s^{-1} V^{-1}$, respectively. Thus, for water vapour at a pressure of 10^{-7} mbar the damping constant γ_+ is equal to about 1 s^{-1}. The damping constant γ_+ for helium at the same pressure is about 0.035 s^{-1}. Thus, for a partial water-vapour pressure of 10^{-7} mbar the radius of the cyclotron motion is reduced by 10% even for a phase-accumulation time of only 0.1 s. For a cyclotron radius $r_+ = 1$ mm, it results in an increase of the image-spot size by a factor of two. If the rest-gas pressure drops well below 10^{-8} mbar, the damping is mainly caused by helium. At a helium pressure of 10^{-7} mbar the damping of the cyclotron motion becomes visible on the detector for phase-accumulation times of longer than 1 s.

Fig. 5.12 shows the radius of the cyclotron-motion image and the radial size of the image spot on the detector for $^{133}Cs^+$ ions measured at SHIPTRAP as a function of the phase-accumulation time. The trap volume had been pumped for three months at room temperature.

Fitting an exponential to the data points yields the damping constant of the cyclotron motion $\gamma_+ = 0.10(1)$ s^{-1}, which corresponds to a water-vapour pressure of about 10^{-8} mbar or a helium pressure of about 3×10^{-7} mbar, which is the expected helium pressure in the MT. Thus, after three months of pumping the contribution of water molecules to the damping is either comparable to or already less significant than that of helium. The smearing of the cyclotron-image spot limits the maximal resolving power to about few times 10^7 for singly charged ions of mass 133 u. Note that the decrease of the radius is approximately equal to the increase of the radial spread. Thus, the assumption that the effect of the residual gas on the ion's cyclotron motion can be described in terms of a drag force is justified. With the present performance cyclotron frequency measurements of nuclides with half-lives well below 1 s will not be affected by the presence of helium and residual gas in the MT. If a resolving power of higher than 10^8 is required for long-lived nuclides at SHIPTRAP, a reduction of the helium

pressure in the PT is necessary. This can affect the performance of the cooling of the initial ion motion in the PT.

5.3.4 Shift of ν_+ due to interconversion of radial motions

As it is mentioned in Sec. 5.1, prior to the projection onto the detector the cyclotron motion must be converted into the magnetron motion by applying a quadrupolar rf-excitation pulse at the sideband (or, obviously, free cyclotron) frequency $\nu_c = \nu_+ + \nu_-$. This shifts the angular position of the image spot by a certain phase. Since the difference of the reference and the final phases is measured, this constant offset cancels out. This is correct only if the frequency of the quadrupolar excitation equals the cyclotron frequency ν_c of the ions at the moment of the conversion and the amplitude of the quadrupolar rf-pulse remains constant. In practice, the reference and final phases are measured at different times. Due to the temporal instability of the magnetic field, the ion's cyclotron frequency ν_c is changing in time. Furthermore, the temporal instability of the trapping voltage results in the fluctuation of the radial frequencies. These lead to different phase offsets of the reference and final phases after the conversion and thus to an error of the cyclotron frequency determination.
Considering the ideal situation when the ions before the conversion perform a pure cyclotron motion with a certain radius and phase and employing the theoretical framework given in Sec. 4.3.2, the ion's complex amplitude and phase at time zero are $\alpha_+(0)$ and $\phi_+(0)$, respectively. After conversion of the ion's cyclotron motion into the magnetron motion the complex amplitude and phase of the ion's magnetron motion $\alpha_-(\tau)$ and $\phi_-(\tau)$, respectively, are given by

$$|\alpha_-(\tau)| \cdot \exp(+i\phi_-(\tau)) = \frac{g}{\pi\nu_R}\sin(\pi\nu_R\tau)|\alpha_+(0)| \times \exp\left[+i\left((2\pi\nu_- + \frac{\delta}{2})\tau + \phi_{\mathrm{rf}} - \phi_+(0) + \frac{3\pi}{2}\right)\right], \quad (5.41)$$

where $2\pi\nu_R = \omega_R$ is the Rabi frequency introduced in Eq. (4.15), and thus

$$|\alpha_-(\tau)| = \frac{g}{\pi\nu_R}\sin(\pi\nu_R\tau)|\alpha_+(0)|, \quad (5.42)$$

$$\phi_-(\tau) = \left(2\pi\nu_- + \frac{\delta}{2}\right)\tau + \phi_{\mathrm{rf}} - \phi_+(0) + \frac{3\pi}{2} + 2\pi k, \quad (5.43)$$

where k is an integer. If the conversion is complete and the detuning parameter $\delta = 0$, then $|\alpha_-(\tau)| = |\alpha_+(0)|$ resulting in

$$g \cdot \tau = \frac{\pi}{2} + 2\pi p, \quad (5.44)$$

$$\phi_-(\tau) = 2\pi\nu_-\tau + \phi_{\mathrm{rf}} - \phi_+(0) + \frac{3\pi}{2} + 2\pi k, \quad (5.45)$$

where p is an integer. Thus, the difference of the final and reference phases of the cyclotron motion $\phi_+^f - \phi_+^r$ is converted into the difference of the final and reference phases of the magnetron motion $\phi_-^f - \phi_-^r$:

$$\phi_-^f - \phi_-^r = -(\phi_+^f - \phi_+^r). \tag{5.46}$$

Hence, the complete conversion at the cyclotron frequency ν_c preserves the angle between the reference and final phases. Note that the ion's cyclotron motion and the movement of the image spot on the detector have opposite angular directions.
The temporal instability of the trapping voltage leads to fluctuations of the magnetron frequency. If the instantaneous magnetron frequencies at the measurement time of the reference and final phases differ by $\delta\nu_-$, then the error of the cyclotron phase determination $\delta\phi_+$ is equal to $\delta\phi_+ = 2\pi \cdot \delta\nu_- \cdot \tau$, which results in the relative error in the determination of ν_+:

$$\frac{\delta\nu_+}{\nu_+} = \frac{\delta\nu_- \cdot \tau}{\nu_+ \cdot t}. \tag{5.47}$$

For a typical daily variation of the magnetron frequency of 100 mHz at SHIPTRAP, $\nu_+ = 800$ kHz, and a π-pulse duration of 1.6 ms

$$\frac{\delta\nu_+}{\nu_+} = \frac{2 \cdot 10^{-10}}{t}. \tag{5.48}$$

Thus, this error is negligible even for very short phase-accumulation times of a few ten ms.
The temporal instability of the magnetic field and hence the free cyclotron frequency $\delta\nu_c$ results in a relative uncertainty of the cyclotron frequency determination

$$\frac{\delta\nu_+}{\nu_+} = \frac{\delta\nu_c \cdot \tau}{2 \cdot \nu_+ \cdot t}. \tag{5.49}$$

The daily fluctuations of the free cyclotron frequency at SHIPTRAP do not exceed 10 mHz resulting in

$$\frac{\delta\nu_+}{\nu_+} \approx \frac{10^{-11}[\mathrm{s}]}{t} \tag{5.50}$$

and thus can be neglected.
The smearing of the magnetron radius due to fluctuations of the cyclotron frequency ν_c and the coupling parameter g can be neglected in all practical cases since the initial spatial distribution of the ions by far exceeds this smearing.
The situation gets more complicated when the ion has a certain magnetron amplitude $\alpha_-(0) = |\alpha_-(0)| \cdot \exp[+i \cdot \phi_-(0)]$ before the conversion. Then, Eq. (5.45) does not hold anymore and hence the conversion results in an error of the modified cyclotron frequency determination. Assuming the maximal degree of conversion of the reference

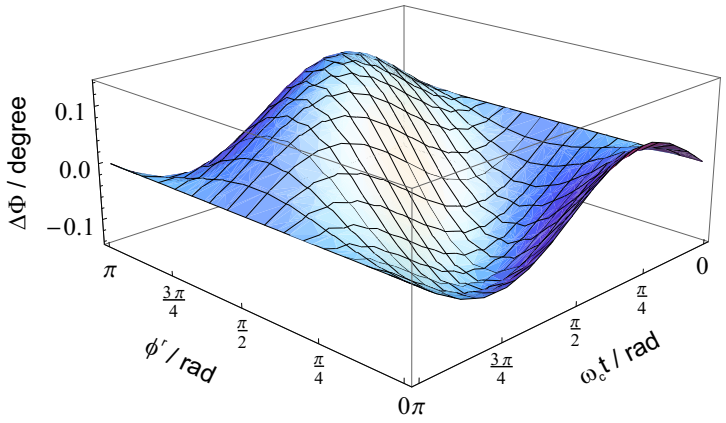

Figure 5.13: Error of the cyclotron phase determination caused by the conversion of the cyclotron motion into the magnetron motion at $S = r_-/r_+ = 0.05$. See text for details.

and final phases, the coupling factor g is given by [104]

$$g \cdot \tau = \frac{\pi}{2} + 2\pi p + \frac{1}{2} \cdot \arctan[2\sin\phi \cdot \frac{S}{S^2 - 1}], \tag{5.51}$$

where $\phi = \phi_{rf} - \phi_-(0) - \phi_+(0)$ and $S = |\alpha_-(0)|/|\alpha_+(0)|$. Then, the error of the cyclotron phase measurement $\Delta\Phi = (\phi_-^f - \phi_-^r) + (\phi_+^f - \phi_+^r)$ for a phase-accumulation time t due to the conversion is given by

$$\Delta\Phi = \arctan\left[\frac{1 - k(f) \cdot \sin(\phi^r + \omega_c t)}{k(f) \cdot \cos(\phi^r + \omega_c t)}\right] - \arctan\left[\frac{1 - k(r) \cdot \sin(\phi^r)}{k(r) \cdot \cos(\phi^r)}\right], \tag{5.52}$$

where $k(f)$ and $k(r)$ are given by

$$k(f) = \frac{2\sin(\phi^r + \omega_c t) \cdot \frac{S^2}{S^2-1}}{1 + \sqrt{1 + 4\sin^2(\phi^r + \omega_c t) \cdot \frac{S^2}{(S^2-1)^2}}} \tag{5.53a}$$

$$k(r) = \frac{2\sin(\phi^r) \cdot \frac{S^2}{S^2-1}}{1 + \sqrt{1 + 4\sin^2(\phi^r) \cdot \frac{S^2}{(S^2-1)^2}}}. \tag{5.53b}$$

$\Delta\Phi$ becomes zero when $\omega_c t = \pi n$, i.e., in order to eliminate the conversion error the phase-accumulation time must be a multiple of half the period of the free cyclotron motion. In practice, this is easily realized with modern delay and rf-function generators. Fig. 5.13 shows $\Delta\Phi$ vs. $\omega_c t$ and ϕ^r for a realistic $S = 0.05$, which corresponds to $r_+ = 0.5$ mm and $r_- = 0.025$ mm.
The maximal conversion error $\Delta\Phi_{max}(S)$ (in degree) vs. S ($S < 1$) is given by

$$\Delta\Phi_{max}(S) \approx 60 \cdot S^2. \tag{5.54}$$

Table 5.3: Relative systematic shifts $\delta\nu_c/\nu_c$ in the cyclotron frequency determination specific to the PI-ICR detection technique.

Source of systematic shift	$\delta\nu_c/\nu_c$
Distortion of orbit-image projection	$< 10^{-11}$
Non-simultaneous measurement of reference and final phases	$\approx 10^{-10}$
Shifts due to conversion caused by	
temporal fluctuations of the trapping voltage	$\approx 10^{-10}$
temporal fluctuations of the magnetic field	$\approx 10^{-10}$
frequency detuning $\delta = \omega_{\mathrm{rf}} - \omega_c$	$\approx 10^{-11}$
poor initial damping of the magnetron motion	$< 5 \times 10^{-10}$

For a realistic $S = 0.05$ the relative uncertainty in the determination of the modified cyclotron frequency at a phase-accumulation time $t = 1$ s is about 0.5 ppb, which can result in a similar relative uncertainty of the cyclotron-frequency-ratio determination. If S is substantially larger than 0.1 or if a precision of better than 0.5 ppb is required, it becomes necessary to choose the phase-accumulation time a multiple of half the period of the free cyclotron motion. In practice, this can only be realized to some extent, since the cyclotron frequency changes in time due to the temporal instability of the magnetic field. Furthermore, very often the masses of the nuclides under investigation and hence their cyclotron frequencies ν_c are not known very precisely. At SHIPTRAP the typical daily absolute and relative fluctuations of the cyclotron frequency of $^{133}Cs^+$ are about 10 mHz and 10^{-8}, respectively. The corresponding maximal daily deviation of $\omega_c t$ from a multiple of π does not exceed $5t/[\mathrm{s}]$ degree and hence can be neglected in all practical cases. Mass formulas predict masses of unknown nuclides on the level of about 1 MeV/c^2. This results in a relative uncertainty of the cyclotron frequency determination of about 10^{-5}. The corresponding uncertainty for $\omega_c t$ exceeds 2π. Thus, first, it is necessary to roughly measure the cyclotron frequency ν_c of the investigated nuclide with at least 100 mHz uncertainty using the ToF-ICR technique. This allows one to set $\omega_c t$ with an uncertainty of better than few $10t/[\mathrm{s}]$ degree. This reduces the conversion error of the cyclotron frequency determination by at least a factor of five, thus making it irrelevant in all practical cases for phase-accumulation times $t < 1$ s and a realistic S.

Tab. 5.3 summarizes different systematic effects specific to the PI-ICR detection technique which cause the corresponding shifts in a determination of the free cyclotron frequency. The magnitudes of the shifts were estimated according to the investigation performed with $^{133}Cs^+$ ions at SHIPTRAP within this thesis work.

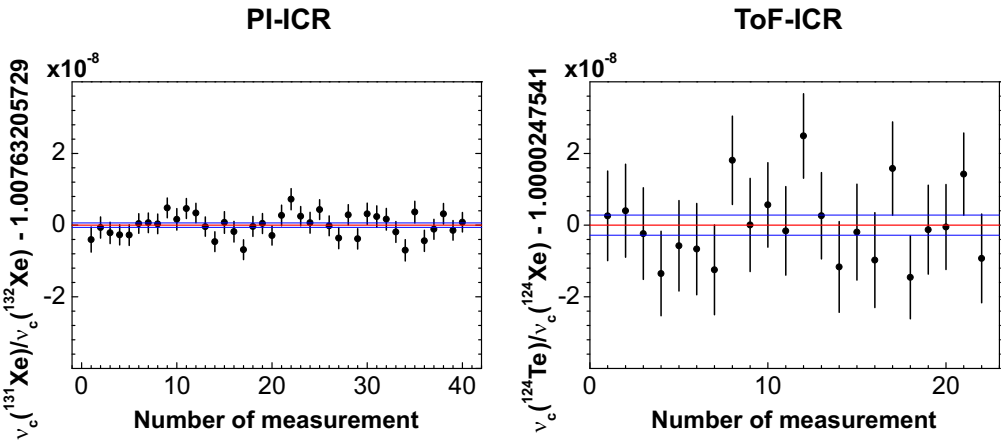

Figure 5.14: Experimental comparison of the PI-ICR and ToF-ICR detection techniques. (left) $\nu_c(^{131}\mathrm{Xe}^+)/\nu_c(^{132}\mathrm{Xe}^+)$ cyclotron frequency ratios, determined with the PI-ICR detection technique. The time intervals between the data points correspond to ~ 5 minutes. (right) $\nu_c(^{124}\mathrm{Te}^+)/\nu_c(^{124}\mathrm{Xe}^+)$ cyclotron frequency ratios, obtained by means of the Ramsey ToF-ICR technique. The time intervals for the measurements of the corresponding ion species were ~ 10 minutes. The red line represents the mean value and the blue lines mark its uncertainty. See text for details.

5.4 Conclusion: Experimental comparison of the PI-ICR and ToF-ICR detection techniques

In order to compare the new technique with the presently used Ramsey time-of-flight detection technique, the data obtained at SHIPTRAP in a day's measurement is presented in Fig. 5.14. The measurements on ^{124}Te/ ^{124}Xe were performed with the Ramsey ToF-ICR technique within the program of a search for $0\nu\epsilon\epsilon$-candidates [141]. The non-isobaric pair of ^{131}Xe/ ^{132}Xe has been recently probed in order to compare the accuracy of the PI-ICR detection technique implemented at SHIPTRAP with the accuracy of the FSU Penning-trap mass spectrometer [73] and the final results are to be published soon [163]. Note that the ^{132}Xe – ^{131}Xe mass difference ~ 1 u imposes even stronger constraints onto the performance of the PI-ICR technique thus challenging the new method.

In general, mass-ratio determination experiments with either technique in use at SHIPTRAP imply alternate cyclotron frequency measurements as described in Chap. 4. Preliminary analysis in both cases was done similar to the analysis routine described in Chap. 4.4.3. Singly charged ions of ^{124}Te were produced by the laser-ablation ion source and the isotopes of xenon were produced by the electron-impact ion source (see Sec. 4.4.1). The performance of the SHIPTRAP setup at the moment of both experiments was the same.

For the measurements employing the Ramsey ToF-ICR detection technique a pulse-

excitation pattern with two π-pulses of 25 ms separated by a 900 ms time delay was used and the acquisition time of a single Ramsey spectrum was ~ 10 minutes resulting in about 800-900 ion events. Thus, for the data shown in Fig. 5.14 (right) the mean frequency ratio was estimated to be $\nu_c(^{124}\mathrm{Te}^+)/\nu_c(^{124}\mathrm{Xe}^+) = 1.0000247541(28)$.
With the PI-ICR technique the frequency ratios $\nu_c(^{131}\mathrm{Xe}^+)/\nu_c(^{132}\mathrm{Xe}^+)$ were obtained using the second pulse-excitation scheme (see Sec. 5.1.2). The phase-accumulation time was $t \sim 500$ ms for both isotopes corresponding to the equal number of cyclotron motion periods $N = 426900$. A single cyclotron frequency measurement lasted ~ 5 minutes resulting in about 800-900 ion events. The mean freqeuency ratio was estimated to be $\nu_c(^{131}\mathrm{Xe}^+)/\nu_c(^{132}\mathrm{Xe}^+) = 1.00763205729(62)$ (Fig. 5.14 (left)).
Hence, employing the PI-ICR detection technique a gain of ~ 4.5 in precision of the frequency-ratio determination was achieved. With an estimated cyclotron radius $r_+ \approx 0.56$ mm and a radial spread $\Delta r_+ \approx 36$ μm a gain in achievable resolving power due to Eq. (5.15) was estimated to be ~ 43.4.
It is worth mentioning that the very first mass-ratio measurements in order to compare the ToF-ICR and PI-ICR techniques [56] were done within this thesis work. Even though a relative error in the determination of the frequency-ratio $\nu_c(^{129}\mathrm{Xe}^+)/\nu_c(^{130}\mathrm{Xe}^+)$ was found to be $\sim 2 \times 10^{-9}$ and the improvement of ~ 3.6 as compared to the ToF-ICR technique was reached, the result was already quite promising for further investigations of this outstanding and relatively simple measurement technique.

Chapter 6

The PENTATRAP mass spectrometer

The novel Penning-trap mass spectrometer PENTATRAP is currently developed at the Max-Planck-Institut für Kernphysik (MPIK) in Heidelberg, Germany. The main goal of PENTATRAP is to perform mass-ratio measurements on highly-charged medium-heavy and heavy ions with a relative precision better than 10^{-11}. As mentioned in Chap. 2, such a precision is required in order to improve the present knowledge on the endpoint energy of the β-decay in ^{187}Re and electron capture in ^{163}Ho for the forthcoming microcalorimetric neutrino experiments.
The main advantage of the PENTATRAP mass spectrometer is the employment of five cylindrical Penning traps, stacked together into one tower. The trap tower is disposed in a 7 T superconducting magnet in liquid helium, which is originally used for cooling of the magnet's coils. Thus, the traps and the cryogenic detection system are cooled down to the 4 K temperature and a cryogenic non-destructive detection system is employed. Another advantage of PENTATRAP is its openness meaning that different ion sources can be used. At present, a commercial electron beam ion trap (EBIT) – the Dresden-EBIT3 [164, 165] – is used allowing to perform experiments with highly charged ions of medium and medium-heavy masses. In the near future, it is planned to replace it with the Heidelberg-EBIT [166] in order to provide mass-ratio measurements on heavy highly charged ions up to bare uranium. The advantage in using of highly charged ions is that the free cyclotron frequency and thus a precision of its determination increases with higher charge state of the ion species by definition, see Eq. (3.1). On the other hand, if one has to determine atomic masses of the nuclides, the electron binding energy has to be known with same relative uncertainty. This is often not the case for heavy ion species and thus a compromise has to be found.
This chapter is dedicated to the development of the Control System for PENTATRAP (CSPT), which was done within the present thesis work. The detailed description of the main components and the measurement principle of the PENTATRAP mass spectrometer can be found in [27, 88, 167]. Thus, only a brief outline of the experimental setup is given in this chapter.

6.1 Overview of the PENTATRAP mass spectrometer

An illustration of the experimental setup is shown in Fig. 6.1. Aimed for the ultra-high precision measurements, the PENTATRAP magnet system is installed in a specially prepared laboratory. Surrounding materials are chosen in order to isolate the room from outer thermal fluctuations and mechanical vibrations. In addition, the magnet is installed on the anti-vibration pneumatic pads. Environmental conditions of the laboratory are actively pressure- and temperature-stabilized by a commercial stabilization system (see details in [167]). Passive shielding of stray electric and high-frequency magnetic fields can be performed by enclosing the magnet with an aluminum housing (not shown in Fig. 6.1).

6.1.1 Cryogenic environment and the magnet system

The PENTATRAP setup employs a 7 T superconducting magnet with the coils designed for a self-shielding of stray magnetic fields. The magnet is installed vertically providing an access from the top to the cold inner bore, filled with liquid helium. The spatial homogeneity of the magnetic field $\Delta B/B$ is about a few ppm in a 1 cm^3 volume in its center [27].
For active shielding of the magnet from stray magnetic fields, a feedback system consisting of a flux-gate magnetometer and a pair of Helmholtz coils mounted around the magnet was developed. The system together with the self-shielding of the magnet provides the estimated total shielding factor larger than 1000. Details concerning the investigation of the magnetic field and the active shielding system are given in the Ph.D. thesis of J. Repp [167] and the Bachelor thesis of A. Rischka [168].
The trap tower consisting of five Penning-traps is fixed inside a vacuum chamber, which holds the cryogenic detection system on the bottom. From top, the chamber is connected by flexible titanium bellows to a stainless steel tube, which is connected in turn to the outer beam line. The trap tower can be aligned with respect to the magnetic field lines by means of a mechanical tilt and shift system, which allows a fine adjustment in the range of $\pm 1^\circ$ and ± 2 mm in the horizontal plane. The total assembly up to the first vacuum valve (Fig. 6.1 (6)) is mounted inside the cold magnet bore. More details on the assembly can be found in [167].
A helium level and pressure stabilization system was developed in order to exclude additional frequency shifts caused by additional magnetic field components that can appear due to the changes in the magnetic susceptibility of the materials around the Penning traps. These changes have a direct dependence on the temperature gradient of the material, which varies due to the evaporation of helium. Details on the development, implementation and control of the helium level and pressure stabilization system will be given in the Ph.D. thesis of Ch. Böhm [169] and the Master thesis of A. Rischka [170].

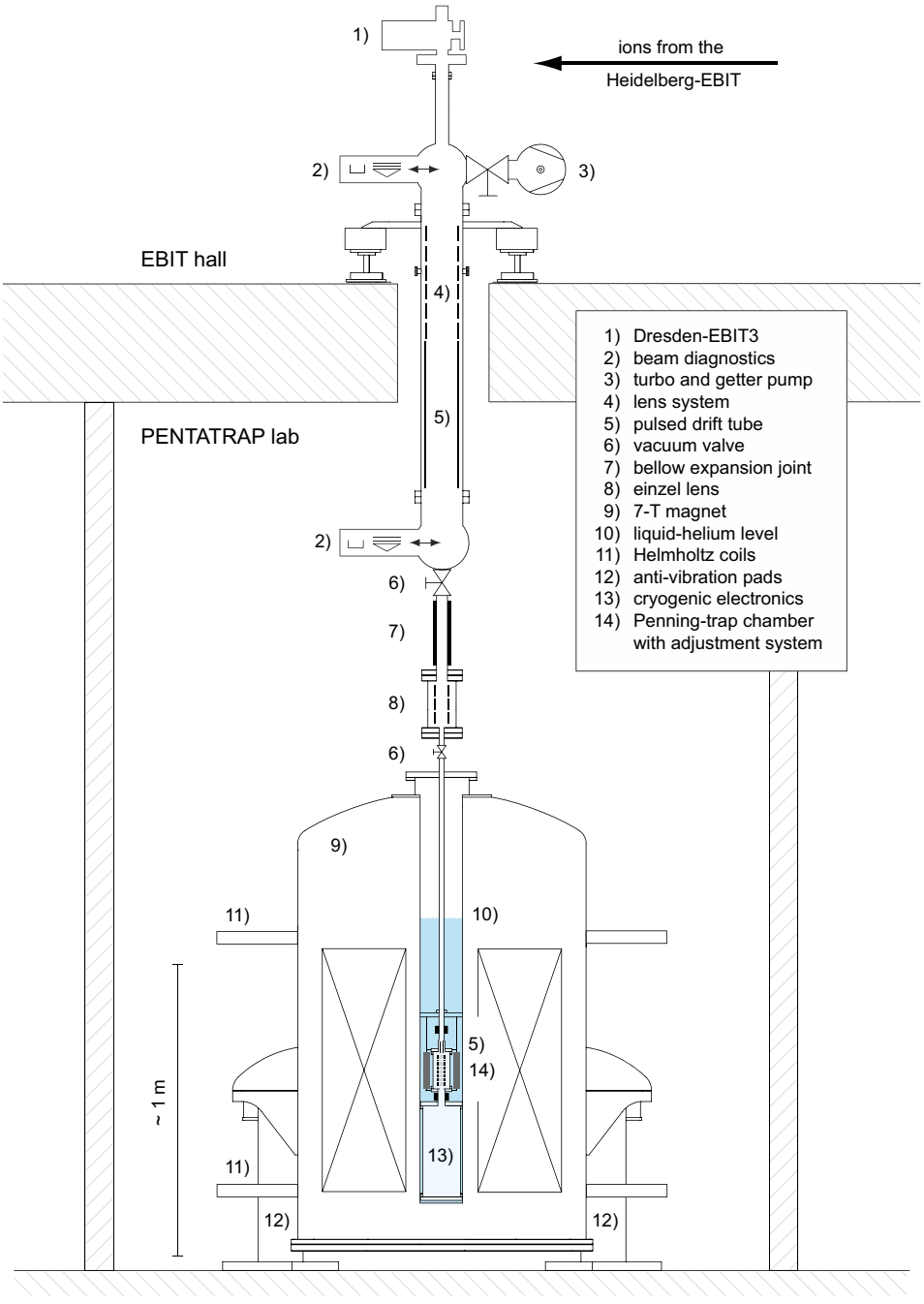

Figure 6.1: Overview of the PENTATRAP setup. The illustration is taken from [88]. For details see text.

6.1.2 Highly stable voltage sources

At PENTATRAP, in order to determine the free cyclotron frequency with precision better than 10^{-11}, the invariance theorem expressed by Eq. (3.9) is employed and all eigenfrequencies are mainly measured via the axial frequency measurements, which are performed by the non-destructive cryogenic detection technique (see below). As it was mentioned in Sec. 3.2.3, in this case voltage fluctuations must be taken into account.
To this end, a novel highly stable voltage source is under development at MPIK, Heidelberg, in collaboration with the Physikalisch-Technische Bundesanstalt (PTB), Braunschweig. The Stable Reference source for Penning traps (StaReP) offers 25 channels with a resolution of ~ 1.5 μV within a voltage range of 0 to -100 V. A temporal stability of the prototype is measured to $\Delta V/V < 4 \times 10^{-8}/(10\text{ min})$ resulting in the relative axial frequency drift of $< 2 \times 10^{-8}$, see Eq. (3.29), and a temperature stability is $< 4 \times 10^{-7}$/K. Details about the technical design, performance and commissioning will be presented in [169].
It is worth mentioning that at present a commercial voltage source UM 1-14 [171] is used. It has a voltage range of 0 to -14 V with a resolution of ~ 1 μV thus limiting the range of highly charged ions due to their charge-to-mass ratio values[1]. The stability of the source was measured to $\Delta V/V \leq 2 \times 10^{-7}/(10\text{ min})$.

6.1.3 Beam line and Ion Sources

The cryogenic assembly of PENTATRAP is connected to the beam line for the external ion injection. It consists of a system of einzel lenses, steerers and pulse drift tubes. The ion-optics assembly was simulated and then designed in order to reach the injection efficiency $> 95\%$ for a beam energy of 7 keV/q and a beam emittance of 3π mm·mrad [27]. In order to trap the ions, the drift tubes are capable to slow the ion's energy from ~ 7 keV/q down to 10 eV/q and below. Two retractable diagnostic stations consisting of a Faraday cup and MCP with phosphor screen can be used to monitor the ion beam.
At present, a commercial EBIT (the DresdenEBIT3 [164, 165]) is mounted on top of the PENTATRAP assembly (see Fig. 6.1, "EBIT hall"). It is capable to produce bare ionic states of nuclides with Z up to 30. Within the installation and commissioning of the DresdenEBIT3 the ions of ^{187}Re and ^{187}Os with charge states up to 50+ were successfully produced [27]. Details on the production process and commissioning of the DresdenEBIT3 are given in [167].
Besides the mass-ratio measurements for neutrino physics, it is planned to perform the measurements on extremely highly charge states of heavy elements. To this end, PENTATRAP will be connected to the Heidelberg-EBIT [166]. Currently, the maximum electron beam energy of 100 keV allows a production of ion species up to helium-like mercury Hg^{78+} or hydrogen-like Ba^{55+} [172]. It is planned to improve the Heidelberg-EBIT in order to produce hydrogen-like or even bare lead or uranium.

[1] Estimations of the voltage range required for different ion species can be found in [88].

6.1.4 Non-destructive detection technique and resistive cooling

In contrast with the ToF-ICR and PI-ICR detection techniques, a non-destructive detection technique [173], used at PENTATRAP, implies the measurement of all eigenfrequencies in order to determine the cyclotron frequency by means of the invariance theorem, see Eq. (3.9). Moreover, in a cryogenic environment this technique offers a single-ion sensitivity and natural cooling of the ions.
Since the PENTATRAP detection system is out of the scope of the present work, only basic concepts are given in this subsection. Detailed description of the detection system developed for PENTATRAP can be found in the Ph.D. theses of C. Roux [88] and A. Dörr [174].
The basic idea of this technique is that if the charged particle oscillates between the plates of an infinitely extended capacitor, it induces image currents in an externally connected impedance [175]. This model can be extended by substituting the capacitor's plates with the trap electrodes [176]. Thus, image currents, induced in the trap electrodes, are given as

$$I = \frac{q}{D_i} 2\pi\nu_i\rho_i, \tag{6.1}$$

where $i = \pm, z$ denotes the eigenmotions, ν_i and ρ_i are the frequency and amplitude of the corresponding eigenmotion, and D_i is an effective electrode distance defined by the geometry of the trap. Typically, the detection system is a tuned circuit, which consists of an inductor L and a total capacitance C of the system given as a sum of the trap capacitance and additional parasitic capacitances. Thus, the detection system has the resonance frequency

$$\nu_{\mathrm{LC}} = \frac{1}{2\pi\sqrt{LC}} \tag{6.2}$$

with the corresponding real effective resistance

$$R = 2\pi\nu_{\mathrm{LC}} QL, \tag{6.3}$$

where Q is the "quality factor" given as

$$Q = \frac{R}{2\pi\nu_{\mathrm{LC}} L} = \frac{\nu_{\mathrm{LC}}}{\Delta\nu}. \tag{6.4}$$

$\Delta\nu$ is a full -3 dB width of the corresponding resonance spectrum defined by the total impedance of the tuned circuit

$$Z_{\mathrm{LC}} = \frac{1}{\frac{1}{R} + i\left(2\pi\nu C - \frac{1}{2\pi\nu L}\right)}. \tag{6.5}$$

If the ion's frequency is tuned to the resonance frequency of the detection system, the ion current produces a voltage signal

$$U = RI = 2\pi\nu_{\mathrm{LC}} QLI. \tag{6.6}$$

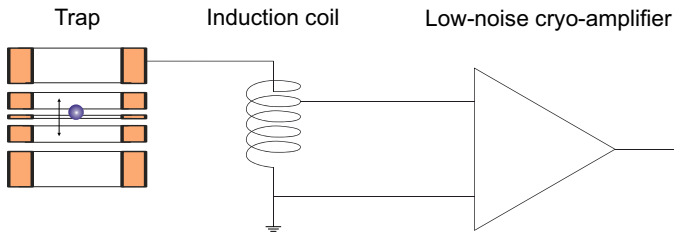

Figure 6.2: Exemplary sketch of the non-destructive detection system. The endcap electrode is connected in parallel to a high-quality inductance and a low-noise cryogenic amplifier. See text for details.

Due to this current flowing through the effective resistance, the excess energy of the ion dissipates if the system was not in thermal equilibrium. Thus, if the trap is coupled, e.g., to the axial detection system, the ion cools to the ambient temperature of the system [173] with a time cooling constant given by

$$\tau_z = \frac{m}{R}\frac{D_z^2}{q^2}. \tag{6.7}$$

Since typically the induced currents are in the fA range, this detection technique requires to employ resonators with extremely large quality factors as well as amplifiers with a high signal-to-noise ratio. Overall, this leads to a low cryogenic environment for a single ion detection, otherwise the ion's signal would be "lost" in the tuned circuit's Johnson noise $u_{\mathrm{th}} = \sqrt{4kTR}$ [177].
A schematic sketch of the cryogenic detection system is shown in Fig. 6.2. At PENTATRAP, the quality factor of the axial detection system is ~ 7000 at the resonance frequency $\nu_{\mathrm{LC}} \approx 660$ kHz and the signal-to-noise ratio is ~ 34 dB [88]. Concerning radial ion motions, their frequencies are measured by quadrupolar coupling to the axial ion motion [102]. A relative precision better than 10^{-11} is planned to be reached by means of the novel so-called Pulse-and-Amplify (PnA) detection technique [178]. The new technique utilizes a phase determination (and hence a frequency) of the modified cyclotron motion by means of the quadrupolar coupling at the sideband frequency $\nu_+ + \nu_z$. This allows the cyclotron frequency measurements with smaller initial amplitudes of the cyclotron motion, which result in a substantial reduction of energy-dependent systematic shifts.

6.1.5 Mass-ratio measurements

As mentioned above, the PENTATRAP mass spectrometer utilizes a stack of five cylindrical Penning traps, what is the main advantage of the novel experimental setup. The traps are designed in order to eliminate the influence of c_4 and c_6 terms in the electric field expansion given by Eq. (3.16) and to fulfill the orthogonality criterion (see

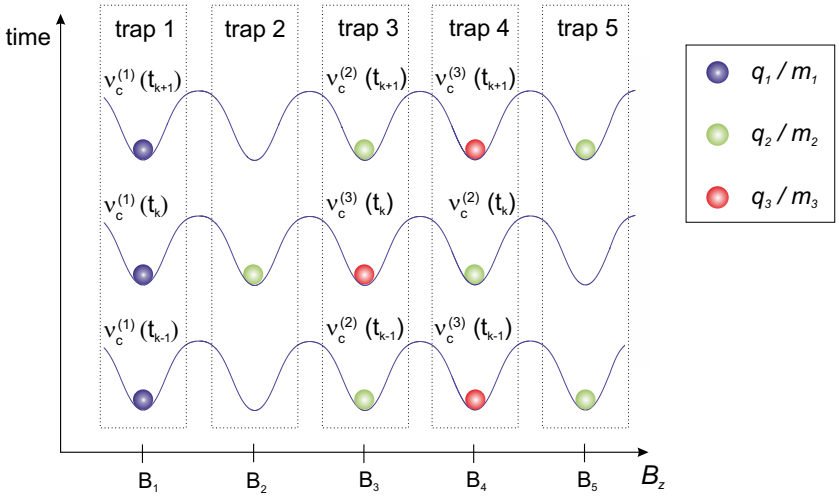

Figure 6.3: Most promising measurement scheme for the PENTATRAP mass spectrometer. Blue lines indicate the electric trapping potentials. B_{1-5} indicate mean values (averaged over time) of the magnetic field in the corresponding traps. The cyclotron frequencies $\nu_c^{(1)}(t_{k-1})$, $\nu_c^{(2)}(t_{k-1})$ and $\nu_c^{(3)}(t_{k-1})$ of three ion species with q_1/m_1, q_2/m_2 and q_3/m_3, respectively, are measured simultaneously at time t_{k-1}. Subsequently, the ions in traps 3 to 5 are moved in block to the adjacent traps (to the left in this figure) and the cyclotron frequency measurement is performed at t_k. Finally, the ions are moved back to their previous positions and the frequency measurement is repeated at time t_{k+1}. This measurement scheme is proposed in order to map fluctuations of the electric and magnetic fields. The illustration is adopted from [167]. For more details see text.

Sec. 3.2.1). A detailed description of the trap design can be found in [88, 179] and the manufacturing process of the traps as well as the assembly of the trap tower are presented in [167].
The most promising measurement routine with five Penning traps is shown in Fig. 6.3. At time t_{k-1} the cyclotron frequencies $\nu_c^{(2)}(t_{k-1})$ and $\nu_c^{(3)}(t_{k-1})$ of two ion species with q_2/m_2 and q_3/m_3, respectively, are measured simultaneously in two adjacent traps 3 and 4 thus resulting in the frequency ratio

$$R(t_{k-1}) = \frac{\nu_c^{(2)}(t_{k-1})}{\nu_c^{(3)}(t_{k-1})} = \frac{q_2}{q_3}\frac{m_3}{m_2} \cdot \frac{B_3}{B_4}|_{t_{k-1}}, \tag{6.8}$$

where $B_3/B_4|_{t_{k-1}}$ is a ratio of the magnetic field strengths in traps 3 and 4 at time t_{k-1}, averaged over the measurement time. This can be understood in a sense that in the presence of magnetic field fluctuations the ratio is nearly constant, while absolute values $B_3(t)$ and $B_4(t)$ can slightly vary over time. The second measurement at time t_k gives the ratio

$$R(t_k) = \frac{\nu_c^{(2)}(t_k)}{\nu_c^{(3)}(t_k)} = \frac{q_2}{q_3}\frac{m_3}{m_2} \cdot \frac{B_4}{B_3}|_{t_k}. \tag{6.9}$$

Thus, under the assumption of constant magnetic field ratios the mass-ratio can be determined from a square root of the product of two ratios:

$$\sqrt{R(t_{k-1}) \cdot R(t_k)} = \sqrt{\left(\frac{q_2}{q_3}\frac{m_3}{m_2}\right)^2 \cdot \frac{B_3}{B_4}|_{t_{k-1}} \frac{B_4}{B_3}|_{t_k}} = \frac{q_2}{q_3}\frac{m_3}{m_2}. \tag{6.10}$$

Finally, the ions are moved back to their initial positions and the measurement is repeated at time t_{k+1}.
During all measurement steps, the frequency $\nu_c^{(1)}$ of the ion species in the first trap is measured continuously. This can serve for additional calibration to the fluctuations of the magnetic field or for a fine-tuning of the voltage source providing the trapping potentials [180] by means of the axial frequency measurements on this ion species.
The measurement scheme proposed in Fig. 6.3 is not the only one. Perhaps, the simplest one is to perform alternate measurements in the central trap (here the highest homogeneity of the magnetic field was measured) similar to those described in Chap. 4. In this case, the advantage of simultaneous trapping of two different ion species in the adjacent traps together with a monitoring of the field fluctuations by means of the third ion species is obvious.
In order to perform fast and reliable frequency measurements, an adiabatic and fast swap of the ion species has to be performed synchronously with the loading of the traps, preparation of the ions and data acquisition. Thus, automation of the measurement process is one of the important tasks in the development of the PENTATRAP mass spectrometer.

6.2 PENTATRAP Control System

The development of the Control System for PENTATRAP (CSPT) has started with choosing of a proper framework. Since the requirements were not really known at the beginning of the PENTATRAP project, it was decided to implement "CS - A Control System Framework for Experiments" (CS-framework or simply CS in the following) already developed by D. Beck and H. Brand at GSI [181, 182] using the LabVIEW System Design Software from National Instruments (NI) [183] as a control system for the SHIPTRAP mass spectrometer. In this context, CS was a promising tool by many reasons given in the following list of requirements imposed to the ISOLTRAP control system [184]:

- CS-framework is open, so that new hardware can easily be included.
- Important is the ability to call any function of any device at any moment. This feature allows investigating systematic effects and debugging of an apparatus.
- The stability and reliability of the control system is an important factor.
- The devices are distributed over a larger area and connected to different PCs. This implies a distributed system with remote access.
- A simple data acquisition must be included in the control system.

Here the last string was crucial due to the fact that all Penning-trap-based experiments (e.g., SHIPTRAP, ISOLTRAP, HITRAP) which employed the CS-framework use also a data acquisition program called "Mass Measure version 6" (mm6). This program is actually a keystone of those control systems since it comprises 1) a Graphical User Interface (GUI) for the control of the measurement process; 2) a state-machine for the control of the internal processes within itself and the CS-framework; 3) a calibration routine for the management of the excitation frequencies, voltages and timings corresponding to the ions with certain charge-to-mass ratio; 4) a proper routine for a setup of the timing schemes used by FPGA-based Pulse-Pattern Generators (PPG); 5) a data handling routine in order to simply write down the acquired data. The drawback of this program is that it was developed specially for the time-of-flight experiments and it has a closed source-code making impossible any transformations to the other types of Penning-trap experiments.
Naturally, the question on what is provided by the CS-framework could arise. Briefly, CS offers a possibility to communicate between different types of devices, a great scalability meaning that employing the object-oriented programming paradigm a class of generic devices can be easily expanded to their successors and any number of devices belonging to the same class can be implemented "on-the-fly" into the experimental setup, an outstanding robustness meaning that it is really hard to crush the core components and they are designed to be self-restoring within any Operational System (OS), and built-in advantages of its "mother" LabVIEW development system.

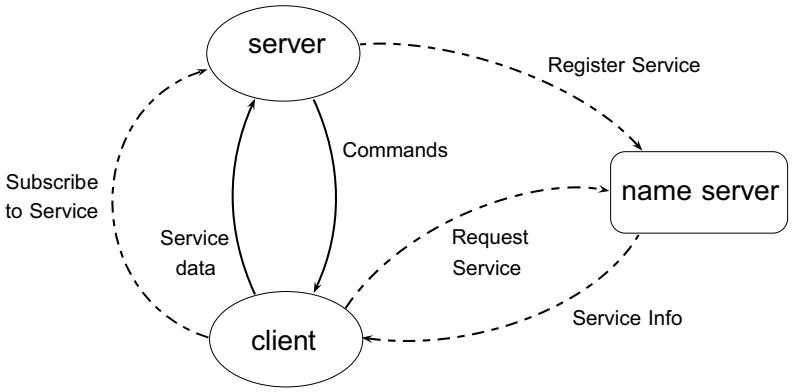

Figure 6.4: Dataflow diagram of DIM. *Name server* keeps an up-to-date directory of all the *servers* and *services* available in the system. *Server* publishes his *services* by registering them with the *name server*. *Client* subscribes to *services* by requesting the *name server* for the name of the corresponding *server* and then directly connects to that *server*. *Client* is updated by means of two possible mechanisms: either it executes a callback routine or its buffer is updated every time the data of the *service* to which the *client* is subscribed is updated.

Thus, with all these *pro et contra* a new program (or a package of programs) should have been developed in order to meet the performance and requirements of the forthcoming PENTATRAP experiment. To this end, it was decided to continue the development within the CS-framework, since the LabVIEW environment wrapping this framework was already an easy and reliable tool for the laboratory experiments supporting a variety of equipment and providing ready-to-use tools like, e.g., Datalogging and Supervisory Control (DSC) module, which is a method of choice for the development of Supervisory Control and Data Acquisition (SCADA) applications, or NI-VISA (Universal I/O Interface Software), which is a fundamental tool for communication with a majority of laboratory equipment. The first steps in the development of the PENTATRAP Control System were done within the author's Master thesis and a deeper investigation has been performed within this thesis work.

6.2.1 Distributed Information Management System

The core of the CS-framework is a so-called Distributed Information Management System (DIM), developed in CERN (Switzerland) [185, 186]. It is a cross-platforming client-server communication engine which provides a high performance and reliability. The diagram of the DIM dataflow is shown in Fig. 6.4. The basic idea of DIM is to manage a list of unique services, distributed across different nodes (i.e., working stations) within the control system. A service is a data unit essentially consisting of a name, a data type and a value. Services belong to the publishers or servers, which in turn are responsible to provide an up-to-date information on their services. Clients subscribe to

the services by means of the name server, which store an up-to-date directory of all the servers and corresponding services. After the client is subscribed, it deals directly with the server. Note that DIM services must have unique names which typically consist of a server and a service names thus providing a clear identification of the parameters in the control system.
The client can be updated either by a direct callback command to the server requesting the data of a certain service or by subscribing to a service. In the second case, the client waits and receives new data only when the data of the service is updated by its server. The client can monitor the status of the service continuously and thus it is updated as soon as the service data has changed (an even-driven concept).
All these basic concepts result in a highly robust system, which stays stable in case of a breakdown of one or more servers or even nodes. Moreover, an event-driven concept provides a high performance allowing to support up to several 10000 services simultaneously without significant losses in a throughput and the processing time.
The CS-framework employs the DIM system by means of the LabVIEW-DIM interface, developed by D. Beck [187]. It was demonstrated that even in the presence of intermediate connection steps which are DIMWrapper and a LabVIEW Run-Time engine the LabVIEW-DIM interface is capable to support almost the same amount of services without significant decrease in the performance. Hence, CS inherits all the benefits of DIM while providing its own advantages.

6.2.2 CS-framework

As mentioned above, CS is a LabVIEW based framework. LabVIEW is a graphical programming language which offers a lot of benefits for the development of applications for experimental investigations. The main advantage is that most of the manufacturers of the laboratory equipment provide LabVIEW-specific device drivers and a variety of communication interfaces is supported by default.
CS is developed following an object-oriented programming paradigm. In the context of the control system this means that each type of the device is represented by its own class, which inherits common features from a parent class, and a single device is an object of the corresponding class. Thus, e.g., voltage sources share a property to set a voltage. This function or a method can be implemented in a common class "Voltage sources", while child classes specific, e.g., for different types or manufacturers could already inherit an internal "low-level" CS routine and only minor changes according to the driver specifications of a certain device are to be implemented.
According to the DIM specifications, CS-framework is a multiplatform system which can naturally intercommunicate across the network. Thus, by means of DIM services any object (or device[2]) can be addressed through the network without "leaving" the CS-framework. Typically, DIM services are not queried directly but by subscription to them, since the first method can result in a significant decrease of the overall performance in case of intensive activity within the control system. Thus, with their

[2] Besides the devices many different utility classes are typically used within CS-framework.

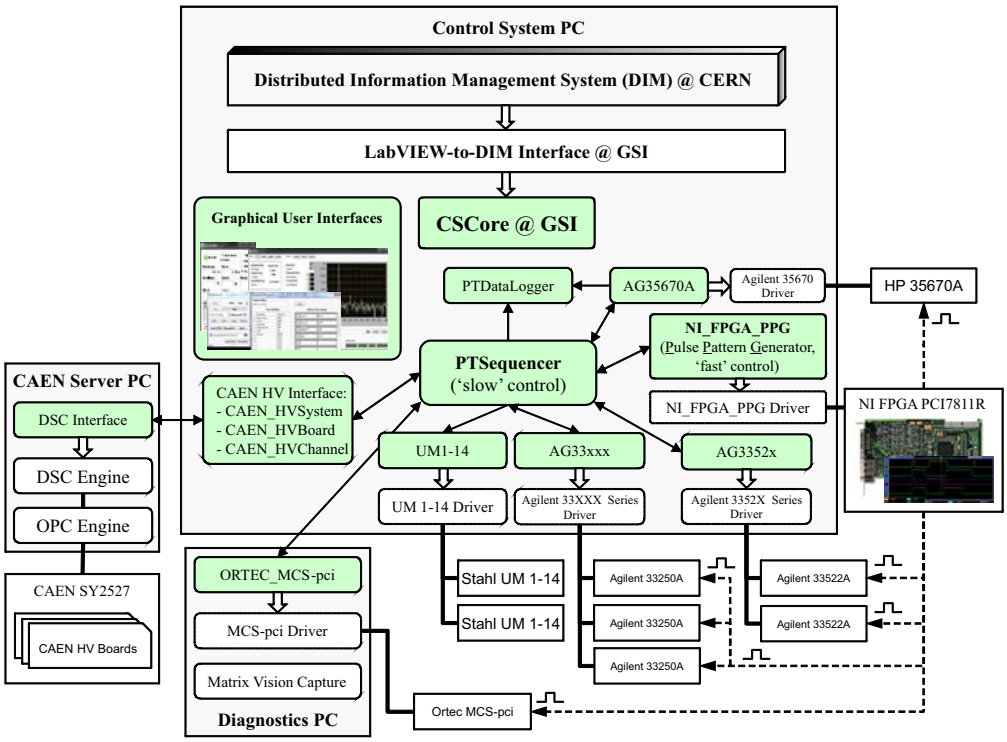

Figure 6.5: Scheme of the PENTATRAP Control System. Green color code indicates the CS classes. White rectangles with round corners correspond to the device-specific drivers. Sharp rectangles represent the devices in use at PENTATRAP (only the devices implemented into the Control System are shown). Solid arrowed lines mark dataflows, dashed arrowed lines mark fast digital triggers. Thick solid lines represent the hardware device interfaces. Grey color indicates the working stations.

uniqueness DIM services in general can be considered as global variables within a single control system.

6.2.3 Structure of the PENTATRAP Control System

A scheme of the PENTATRAP Control System is presented in Fig. 6.5. The PENTATRAP Control System was developed in order to substitute the mm6 program, specific for the ToF-ICR Penning-trap experiments. To this end, new classes for the automation of the measurement procedure were developed and the class of the FPGA card, which serves as a pattern-pulse generator (PPG), was significantly modified. The devices in Fig. 6.5 do not comprise a total device kit used at PENTATRAP. A lot of minor equipment dedicated to specific routines like Fluke multimeters or servo motors are controlled currently by small self-made programs or a commercial software. Moreover, recent activity at the PENTATRAP laboratory has shown that it is often more convenient to use a development environment instead of a complete assembled system

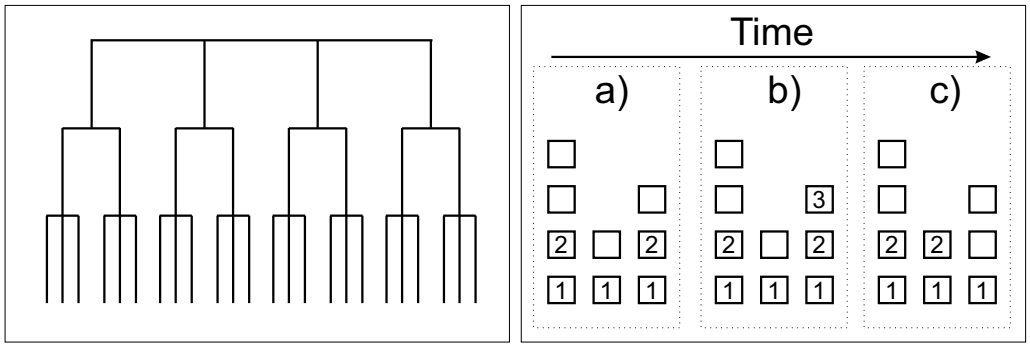

Figure 6.6: Exemplary scheme of the multi-dimensional scan. (left) A tree corresponding to an arbitrary 3D-scan with 4, 2 and 3 steps at the corresponding levels. (right) 3 subsequent steps of a 3D-scan expressed as a flattened version of the tree. Every column in a single step corresponds to the level of the scan resulting in a 3-digit number, in which every digit is counted within its own numeral system. Weights of their numeral systems are given as 4, 2 and 3, respectively. See text for details.

in case of intensive development of the experimental setup. This is another advantage of LabVIEW since it is possible to control the devices in parallel with the running compilation of the Control System.
Specific details concerning recent developments of the device and automation classes are given in the following. Unfortunately, the best way to present this work is to present a source-code or working modules of the Control System. Since it is not possible here, only the main issues are considered.

6.2.4 Automation classes of the PENTATRAP Control System

For automation of the experiment three main classes, namely PTScanner, PTSequencer and PTDataHandler, as well as a package of small utilities were developed. These classes are aimed to offer the maximal flexibility due to the lack of knowledge concerning a final version of the PENTATRAP setup and the measurement procedure. Hence, all these classes allow to subscribe to any DIM service "on-the-fly" and offer several options for sorting and analyzing the values of these global variables.

PTScanner

PTScanner is a class that allows to provide multi-dimensional scans of various parameters of the system. To scan the parameter means to change it stepwise in a certain range around the aimed value. Thus, the user has to define a parameter, which corresponds to the device and a certain function like, e.g., frequency or voltage, its central value x_0, a range $2\Delta x$ and a step δx. Thus, the simplest scan is just a linear variation of the value from $x_0 - \Delta x$ to $x_0 + \Delta x$ with $2\Delta x/\delta x$ steps. In case of many variables, it is straight forward to use a recursion in order to build a tree of corresponding steps as shown in Fig. 6.6 (left). However, recursive calls were not supported by LabVIEW 8.5 and some

	Command Description	Object	Command	Check	Passed	Failed
	Reset NV Scanner	PTScanner	Reset		Next	Next
	Reset PV Scanner	PTScanner1	Reset		Next	Next
	Set next negative voltage	PTScanner	SetNextStep		Next	Next
	Set next positive voltage	PTScanner1	SetNextStep		Next	Next
	Wait until voltages has switched	TestSequencer	Ping	X	Next	Next
	Clear MCS	MCS-pci1	Clear	X	Next	Repeat
	Start measurement	MCS-pci1	Start	X	Jump: 08	Repeat
	Stop MCS	MCS-pci1	Stop	X	Jump: 11	Repeat
	Wait for measurement has been dor	TestSequencer	Ping	X	Next	Repeat
	Save data	DataLogger	SaveData		Next	Next
	Check stop conditions	TestSequencer	Ping	X	Jump: 12	Next
	Check loop conditions	TestSequencer	Ping	X	Jump: 02	Jump: 02
	Stopping	MCS-pci1	Ping	X	Next	Repeat

Figure 6.7: Lookup table of PTSequencer setup for the measurements with DresdenEBIT3. For details see text.

other solution should have been implemented. To this end, the multi-dimensional scan can be flattened as shown in Fig. 6.6 (right). Assuming a 3D-scan with $i = 4$, $j = 2$ and $k = 3$ steps at the first, second and third levels of the tree, respectively, one can count as in the case of numeral system with non-decimal weight with an exception that every single digit in number ijk belongs to its own numeral system. Thus, a series of numbers corresponding to the steps of a 3D-scan is given as

$$111,\ 112,\ 113,\ 121,\ 122,\ 123,\ 211,\ 212,\ 213,\ 221, \ldots \tag{6.11}$$

where the last three numbers correspond to the steps a), b) and c) in Fig. 6.6 (left), respectively. With LabVIEW 2009 it was possible to implement a recursive method. However, due to the modern speed of computing it cannot be concluded precisely, which method offers better performance. Thus, the method described here is still employed.

PTSequencer

A sequencer was developed in order to gather different devices into one chain of a single measurement. This class can be explained in terms of a lookup table, for which the user has to define all the steps. An example of such a table used in the measurements with DresdenEBIT3 is presented in Fig. 6.7. Here, the user can assign how a sequencer should move across the table after a certain step is accomplished.
Crucial points in the development of a sequencer were: How to provide a proper indexing between the steps and the corresponding devices in order not to overload the system and to save available memory; and how to organize a complicated case structure (due to the maximal flexibility of a sequencer) in a way that no bugs are introduced into the system.

PTDataHandler

The only purpose of this class is the data acquisition. It was developed in a way that the user can setup how the data from different sources should be organized in order to be stored. A flexibility here is a drawback since querying hundreds of DIM services during a setup procedure significantly slows the system. In the near future this is planned to be fixed by introducing additional setup steps which should reduce an amount of the processor time consumed by the class.

6.2.5 Device classes of the PENTATRAP Control System

A full list of the devices included into the Control System is presented in Tab. 6.1. Agilent frequency generators were found to be the most reliable devices. However, couple of hardware bugs like lower available time resolution was found within this work. Thanks for their support team, a firmware update was provided extremely fast. The Agilent (Hewlett-Packard) FFT 35670A is currently in use but out of the control system due to its slow read-out routine. The classes of high voltage sources from CAEN are to be modified in a sense that their network latency seems to be too high. Ultra-high stable voltage source StaReP is currently in development so it is hard to say what will be the final version of this class.

6.3 Summary

The very first commissioning of the Control System was done within the commissioning of the DresdenEBIT3 [167]. In the measurements, a multi-channel scalar (MCS) from ORTEC, Agilent frequency generators, CAEN voltage sources and utility classes were successfully employed and significant amount of data was acquired during continuous runs of the Control System.
Currently the loading scheme at PENTATRAP implies a usage of CSPT together with LabVIEW development system. To this end, the FPGA timing source was modified in order to be able to start its sequence by two trigger pulses in coincidence. The first pulse is produced by the frequency generator which serves as a continuous trigger for the trap opening of the DresdenEBIT3. The second pulse is generated manually from the LabVIEW environment. Thus, the semi-manual loading routine is performed.
To conclude, the main parts of the PENTATRAP Control System was developed and the results are presented in this chapter. Due to a rapid development of the experiment at present it is hard to make a snapshot of the setup in order to implement new ideas into the Control System, since it is still heavier than a toolkit of small utility programs, which can be changed in minutes. In the future, with the final estimations on the setup performance it will be possible to complete the Control System in order to provide automatic mass-ratio measurements with a variety of scenarios due to the flexibility of the system.

Table 6.1: A list of the devices included into the Control System is presented in the first column. In column 2, "modified" means the class was already implemented in CS and significantly modified within this work. In column 3 "modified" means either the driver was provided by the manufacturer or developed in CS-framework and then modified for PENTATRAP. Column 4 shows the availability of the Graphical User Interface (everything developed in this work) and column 5 indicates the usage of the devices at present.

Device	Class	LabVIEW Driver	GUI	Status
Agilent 33250A	AG33XXX	commercial	available	in active use
rf-generator	(modified)			
Agilent 33522B	AG3352X	modified	available	in active use
rf-generator	(new)			
HP35670A	AG35670A	self-made	available	not in use
FFT analyzer	(new)			
CAEN SY2527	CAEN_HVChannel	modified	available	in active use
high voltage source	(modified)			
NI-FPGA	NI_FPGA_PPG	modified	available	in active use
delay-line generator	(modified)			
ORTEC MCS-pci	ORTEC_MCS-pci	self-made	available	in use
multi-channel scalar	(new)			
UM 1-14	UM1-14	self-made	available	driver in use
UHS voltage source	(new)			
StaReP	StaReP	self-made	not available	driver in use
UHS voltage source	(new)			

Chapter 7

Conclusion and Outlook

This thesis is dedicated to the mass-ratio measurements for neutrino physics by means of Penning-trap mass spectrometry. In the following, a brief summary on the research work done in the context of the thesis is outlined.

A detection of neutrinoless double-electron capture would reveal the Majorana nature of the neutrino, what violates lepton number conservation. This question is one of the fundamental questions in neutrino physics, which is already beyond the Standard Model of elementary particles. The $0\nu\epsilon\epsilon$-decay is a very rare process due to its nature. However, with recent investigations concerning a possible resonance enhancement of the decay rate in certain nuclides it could be possible to find a suitable candidate with which the task on the detection of this process by means of, e.g., microcalorimetry would become realistic.
Within the present thesis work, a series of measurements dedicated to a search for the resonantly enhanced $0\nu\epsilon\epsilon$-transitions in ^{102}Pd, ^{106}Cd, ^{144}Sm and ^{156}Dy was performed with the SHIPTRAP mass spectrometer. The results of this work are presented in Chapter 4. The total decay energy of the transitions was determined from the mass-ratios of the corresponding isobaric pairs which were measured with a relative precision of a few 10^{-9}.
In the framework of the resonance enhancement it was found that several transitions in ^{106}Cd and ^{156}Dy are resonantly enhanced. Moreover, ^{156}Dy was found to provide multiresonance enhancement due to its nuclear and atomic structure. Careful investigation of the transitions in ^{156}Dy was resulted in the estimated partial half-lives of 6×10^{28} years in the most promising case. The main uncertainty in the determination of the resonance enhancement was due to the poor knowledge on the nuclear structure of the corresponding nuclides. Thus, it was concluded that ^{102}Pd, ^{106}Cd, ^{144}Sm and ^{156}Dy can be temporary excluded from the list of promising candidates unless the improvements in the field of nuclear structure physics will occur.

In Chapter 5, the novel Phase-Imaging Ion-Cyclotron-Resonance detection technique, which was developed and implemented at SHIPTRAP within this work, is presented. This technique imply a determination of the cyclotron frequencies by acquiring the

phase images of the radial motions of the charged particles in a Penning trap. It was shown theoretically and proved empirically that in comparison with the presently used Ramsey time-of-flight detection technique a gain 40 in resolving power and a gain of ~ 5 in precision can be achieved while the measurement time can be substantially decreased. With the new PI-ICR method a study of systematic effects specific for this technique was done at SHIPTRAP employing $^{133}Cs^{+}$ ions.
With the performance of the novel detection technique it should be possible to resolve isobars and isomers of short-lived nuclides and to measure their masses with higher precision than that provided presently by the time-of-flight detection technique. This is of great importance due to specific of the production mechanisms corresponding to the existing radioactive facilities. Moreover, Q-value measurements of $^{187}Re - ^{187}Os$ and $^{163}Ho - ^{163}Dy$ with an absolute uncertainty of a few tens eV could be performed employing the PI-ICR detection technique in order to provide a systematic check of the forthcoming microcalorimetric experiments.

The novel Penning-trap mass-spectrometer PENTATRAP aims for mass-ratio measurements on highly-charged ions with a relative precision better than 10^{-11}. In order to reach such a precision, a lot of advanced techniques has been recently developed. A control system – one of the bricks of the PENTATRAP setup – was developed within the present work and is presented in Chapter 6. As the development has started at the time the magnet was not even installed, the very general considerations concerning the experimental design were put into the foundation of the control system. Moreover, since different equipment used at PENTATRAP is not typically compatible to each other, the control system should have provided common communication mechanisms in order to cover all devices in use. Eventually, the successful commissioning of the PENTATRAP EBIT ion source as well as a detection of the first trapped ions was done employing the new control system.
With the aimed ultra-high precision several future experimental programs are proposed at PENTATRAP. The first goal is to determine the Q-values of $^{187}Re - ^{187}Os$ and $^{163}Ho - ^{163}Dy$ with an absolute uncertainty better than a few eV in order to improve the present knowledge on the endpoint energy of the corresponding β-processes. Another interesting task is to perform experiments with highly-charged ions of heavy elements like, e.g., U^{92+}. This can push forward the present knowledge on QED in strong electric fields.

All these exciting perspectives conclude this thesis.

The End.

Bibliography

[1] Sir Isaac Newton, *The Mathematical Principles of Natural Philosophy*, Benjamin Motte, London (1729). Translated into English by Andrew Motte.

[2] L. B. Okun', *The concept of mass (mass, energy, relativity)*, UFN **158**, 511 (1989).

[3] E. Goldstein, *Über eine noch nicht untersuchte Strahlungsform an der Kathodeinducirter Entladungen*, Berlin Akd. Monatsber. **II**, 691 (1886).

[4] J. J. Thomson, *Cathode Rays*, Phil. Mag. **44**, 293 (1897).

[5] J. J. Thomson, *Further experiments on positive rays*, Phil. Mag. **24**, 209 (1912).

[6] F. W. Aston, *Isotopes and Atomic Weights*, Nature **105**, 617 (1920).

[7] F. W. Aston, *"Mass Spectra and Isotopes"* in Nobel Lectures, Chemistry 1922–1941, Elsevier, Amsterdam (1966).

[8] F. W. Aston, *Bakerian Lecture. A New Mass-Spectrograph and the Whole Number Rule*, Proc. R. Soc. Lond. A **115**, 487 (1927).

[9] A. Einstein, *Ist die Trägheit eines Körpers von seinem Energieinhalt abhängig?*, Ann. Phys. **323**, 639 (1905).

[10] A. S. Eddington, *The Internal Constitution of the Stars*, Cambridge University Press (1926).

[11] G. Gamow, *Mass Defect Curve and Nuclear Constitution*, Proc. R. Soc. Lond. A **126**, 632 (1930).

[12] C. F. von Weizsäcker, *Zur Theorie der Kernmassen*, Z. Phys. **96**, 431 (1935).

[13] H. A. Bethe and R. F. Bacher, *Nuclear Physics A. Stationary States of Nuclei*, Rev. Mod. Phys. **8**, 82 (1936).

[14] K. Blaum, *High-accuracy mass spectrometry with stored ions*, Phys. Rep. **425**, 1 (2006).

[15] H. G. Dehmelt, *Stored-Ion Spectroscopy*, Advances in Laser Spectroscopy **A**, 153 (1983). Springer US.

[16] P. B. Schwinberg, R. S. Van Dyck Jr. and H. G. Dehmelt, *Trapping and thermalization of positrons for geonium spectroscopy*, Phys. Lett. A **81**, 119 (1981).

[17] G. Gräff, H. Kalinowsky and J. Traut, *A Direct Determination of the Proton Electron Mass Ratio*, Z. Phys. A **297**, 35 (1980).

[18] H. Stolzenberg *et al.*, *Accurate mass determination of short-lived isotopes by a tandem Penning-trap mass spectrometer*, Phys. Rev. Lett. **65**, 3104 (1990).

[19] R. S. Van Dyck Jr., D. B. Pinegar, S. van Liew and S. L. Zafonte, *The UW-PTMS: Systematic studies, measurement progress, and future improvements*, Int. J. Mass Spectrom. **251**, 231 (2006).

[20] M. Redshaw, J. McDaniel and E. G. Myers, *Dipole Moment of PH^+ and the Atomic Masses of Si^{28}, P^{31} by Comparing Cyclotron Frequencies of Two Ions Simultaneously Trapped in a Penning Trap*, Phys. Rev. Lett. **100**, 093002 (2008).

[21] A. Kellerbauer *et al.*, *From direct to absolute mass measurements: A study of the accuracy of ISOLTRAP*, Eur. Phys. J. D **22**, 53 (2003).

[22] J. Dilling *et al.*, *Mass measurements on highly charged radioactive ions, a new approach to high precision with TITAN*, Int. J. Mass Spectr. **251**, 198 (2006).

[23] J. Hakala *et al.*, *Precision Mass Measurements beyond ^{132}Sn: Anomalous Behavior of Odd-Even Staggering of Binding Energies*, Phys. Rev. Lett. **109**, 032501 (2012).

[24] Y. Fukuda *et al. (Super-Kamiokande Collaboration)*, *Evidence for Oscillation of Atmospheric Neutrinos*, Phys. Rev. Lett. **81**, 1562 (1998).

[25] E. Ferri *et al.*, *MARE-1 in Milan: Status and Perspectives*, J. Low Temp. Phys. **167**, 1035 (2012).

[26] P. C.-O. Ranitzsch *et al.*, *Development of Metallic Magnetic Calorimeters for High Precision Measurements of Calorimetric ^{187}Re and ^{163}Ho Spectra*, J. Low Temp. Phys. **167**, 1004 (2012).

[27] J. Repp *et al.*, *PENTATRAP: a novel cryogenic multi-Penning-trap experiment for high-precision mass measurements on highly charged ions*, Appl. Phys. B **107**, 983 (2012).

[28] S. Eliseev, Yu. N. Novikov and K. Blaum, *Penning-trap mass spectrometry and neutrino physics*, Ann. Phys. **525**, 707 (2013).

[29] C. Jensen and F. Aaserud, *Controversy and Consensus: Nuclear Beta Decay 1911-1934*, Science Networks. Historical Studies, Springer (2000).

[30] L. M. Brown, *The idea of the neutrino*, Physics Today **31**, 23 (1978).

[31] Fred L. Wilson, *Fermi's Theory of Beta Decay*, Am. J. Phys. **36**, 1150 (1968).

[32] F. Boehm and P. Vogel, *Physics of massive neutrinos, Second edition*, Cambridge University Press (1992).

[33] Z. Maki, M. Nakagawa and S. Sakata, *Remarks on the Unified Model of Elementary Particles*, Prog. Theor. Phys. **28**, 870 (1962).

[34] B. Pontecorvo, *Neutrino experiments and the question concerning the lepton charge conservation*, JETP **53**, 1717 (1967).

[35] R. Davis Jr., D. S. Harmer and K. C. Hoffman, *Search for Neutrinos from the Sun*, Phys. Rev. Lett. **20**, 1205 (1968).

[36] Y. Fukuda *et al.* (Super-Kamiokande Collaboration), *Evidence for Oscillation of Atmospheric Neutrinos*, Phys. Rev. Lett. **81**, 1562 (1998).

[37] B. Aharmim *et al.* (SNO Collaboration), *Combined Analysis of all Three Phases of Solar Neutrino Data from the Sudbury Neutrino Observatory*, Phys. Rev. C **88**, 025501 (2013).

[38] K. Nakamura *et al.* (Particle Data Group), *Review of particle physics*, J. Phys. G-Nucl. Part. Phys. **37**, 1 (2010).

[39] F. Šimkovic, R. Dvornický and A. Faessler, *Exact relativistic tritium β-decay endpoint spectrum in a hadron model*, Phys. Rev. C **77**, 055502 (2008).

[40] Nicola Cabibbo, *Unitary Symmetry and Leptonic Decays*, Phys. Rev. Lett. **10**, 531 (1963).

[41] Makoto Kobayashi and Toshihide Maskawa, *CP-Violation in the Renormalizable Theory of Weak Interaction*, Prog. Theor. Phys. **49**, 652 (1973).

[42] G. C. Rodrigues *et al.*, *Systematic calculation of total atomic energies of ground state configurations*, Atomic Data and Nuclear Data Tables **86**, 117 (2004).

[43] G. Drexlin, V. Hannen, S. Mertens and C. Weinheimer, *Current Direct Neutrino Mass Experiments*, Advances in High Energy Phys. **2013**, 293986 (2013).

[44] KATRIN collaboration, *KATRIN: A next generation tritium beta decay experiment with sub-eV sensitivity for the electron neutrino mass*, Letter of Intent (2001). arXiv:hep-ex/0109033.

[45] S. Nagy, T. Fritioff, M. Björkhage, I. Bergström and R. Schuch, *On the Q-value of the tritium β-decay*, Europhys. Lett. **74**, 404 (2006).

[46] V. Lobashev *et al.*, *Direct search for neutrino mass and anomaly in the tritium beta-spectrum: Status of "Troitsk neutrino mass" experiment*, Nucl. Phys. B - Proc. Sup. **91**, 280 (2001).

[47] C. Kraus *et al.*, *Final Results from phase II of the Mainz Neutrino Mass Search in Tritium β Decay*, Eur. Phys. J. C **40**, 447 (2005).

[48] K. Blaum, Yu. N. Novikov and G. Werth, *Penning traps as a versatile tool for precise experiments in fundamental physics*, Contemp. Phys. **51**, 149 (2010).

[49] C. Diehl *et al.*, *Progress with the MPIK/UW-PTMS in Heidelberg*, Hyperfine Interact. **199**, 291 (2011).

[50] G. Audi *et al.*, *The Ame2012 atomic mass evaluation*, Chinese Phys. C **36**, 1287 (2012).

[51] E. W. Otten and C. Weinheimer, *Neutrino mass limit from tritium β decay*, Rep. Prog. Phys. **71**, 086201 (2008).

[52] M. Galeazzi, F. Fontanelli, F. Gatti and S. Vitale, *End-point energy and half-life of the 187Re β decay*, Phys. Rev. C **63**, 014302 (2000).

[53] C. Arnaboldi *et al.*, *Bolometric Bounds on the Antineutrino Mass*, Phys. Rev. Lett. **91**, 161802 (2003).

[54] F. Gatti, *Microcalorimeter measurements*, Nucl. Phys. B - Proc. Sup. **91**, 293 (2001).

[55] M. Sisti *et al.*, *New limits from the Milano neutrino mass experiment with thermal microcalorimeters*, Nucl. Instr. Meth. A **520**, 125 (2004).

[56] S. Eliseev *et al.*, *Phase-Imaging Ion-Cyclotron-Resonance Measurements for Short-Lived Nuclides*, Phys. Rev. Lett. **110**, 082501 (2013).

[57] S. Eliseev *et al.*, *A phase-imaging technique for cyclotron-frequency measurements*, Appl. Phys. B, **114**, 107 (2014).

[58] F. Gatti, P. Meunier, C. Salvo and S. Vitale, *Calorimetric measurement of the ^{163}Ho spectrum by means of a cryogenic detector*, Phys. Lett. B **398**, 415 (1997).

[59] S. Eliseev and Ch. Böhm *et al.*, *Direct mass measurements of ^{194}Hg and ^{194}Au: A new route to the neutrino mass determination?*, Phys. Lett. B **693**, 426 (2010).

[60] A. Thompson *et al.*, , X-ray data booklet (2009). URL http://xdb.lbl.gov/.

[61] P. T. Springer, C. L. Bennett and P. A. Baisden, *Measurement of the neutrino mass using the inner bremsstrahlung emitted in the electron-capture decay of ^{1}63Ho*, Phys. Rev. A **35**, 679 (1987).

[62] M. Goeppert-Mayer, *Double Beta-Disintegration*, Phys. Rev. **48**, 512 (1935).

[63] W. H. Furry, *On Transition Probabilities in Double Beta-Disintegration*, Phys. Rev. **56**, 1184 (1939).

[64] K. Zuber, *On the physics of massive neutrinos*, Phys. Rep. **305**, 295 (1998).

[65] J. Kotila and F. Iachello, *Phase-space factors for double-β decay*, Phys. Rev. C **85**, 034316 (2012).

[66] A. S. Barabash, *Double Beta Decay: Historical Review of 75 Years of Research*, Phys. Atom. Nucl. **74**, 603 (2011).

[67] B. Schwingenheuer, *Status and prospects of searches for neutrinoless double beta decay*, Annalen Phys. **525**, 269 (2013).

[68] H. V. Klapdor-Kleingrothaus and I. V. Krivosheina, *The evidence for the observation of $0\nu\beta\beta$ decay: The identification of $0\nu\beta\beta$ events from the full spectra*, Mod. Phys. Lett. **A21**, 1547 (2006).

[69] E. Andreotti *et al.* (CUORICINO collaboration), *130Te Neutrinoless Double-Beta Decay with CUORICINO*, Astropart. Phys. **34**, 822 (2011).

[70] R. Arnold *et al.* (NEMO-3 collaboration), Search for Neutrinoless Double-Beta Decay of ^{100}Mo with the NEMO-3 Detector, arXiv:1311.5695 [hep-ex] (2013). URL http://arxiv.org/abs/1311.5695.

[71] M. Redshaw, E. Wingfield, J. McDaniel and E. G. Myers, *Mass and Double-Beta-Decay Q Value of ^{136}Xe*, Phys. Rev. Lett. **98**, 053003 (2007).

[72] S. Rahaman *et al.*, *Q values of the ^{76}Ge and ^{100}Mo double-beta decays*, Phys. Lett. B **662**, 111 (2008).

[73] M. Redshaw, B. J. Mount, E. G. Myers and F. T. Avignone, *Masses of ^{130}Te and ^{130}Xe and Double-β-Decay Q Value of ^{130}Te*, Phys. Rev. Lett. **102**, 212502 (2009).

[74] S. Eliseev, Yu. N. Novikov and K. Blaum, *Search for resonant enhancement of neutrinoless double-electron capture by high-precision Penning-trap mass spectrometry*, J. Phys. G: Nucl. Part. Phys. **39**, 124003 (2012).

[75] R. G. Winter, *Double K Capture and Single K Capture with Positron Emission*, Phys. Rev. **100**, 142 (1955).

[76] Masaru Doi and Tsuneyuki Kotani, *Neutrinoless Modes of Double Beta Decay*, Prog. Theor. Phys. **89**, 139 (1993).

[77] J. Bernabéu, A. D. Rújula and C. Jarlskog, *Neutrinoless double electron capture as a tool to measure the electron neutrino mass*, Nucl. Phys. B **223**, 15 (1983).

[78] Z. Sujkowski and S. Wycech, *Neutrinoless double electron capture: A tool to search for Majorana neutrinos*, Phys. Rev. C **70**, 052501 (2004).

[79] M. I. Krivoruchenko, F. Šimkovic, D. Frekers and A. Faessler, *Resonance enhancement of neutrinoless double electron capture*, Nucl. Phys. A **859**, 140 (2011).

[80] F. T. Avignone, S. R. Elliott and J. Engel, *Double beta decay, Majorana neutrinos, and neutrino mass*, Rev. Mod. Phys. **80**, 481 (2008).

[81] J. Suhonen, *Neutrinoless double beta decays of ^{106}Cd revisited*, Phys. Lett. B **701**, 490 (2011).

[82] F. Šimkovic, A. Faessler, H. Müther, V. Rodin and M. Stauf, *$0\nu\beta\beta$-decay nuclear matrix elements with self-consistent short-range correlations*, Phys. Rev. C **79**, 055501 (2009).

[83] T. R. Rodríguez and G. Martínez-Pinedo, *Energy Density Functional Study of Nuclear Matrix Elements for Neutrinoless $\beta\beta$ Decay*, Phys. Rev. Lett. **105**, 252503 (2010).

[84] F. B. Larkins, *Semiempirical Auger-electron energies for elements $10 \leq Z \leq 100$*, Atom. Data Nucl. Data Tables **20**, 311 (1977).

[85] K. Zuber, *Double beta decay*, Contemporary Physics **45**, 491 (2004).

[86] J. Suhonen, *Sub-eV neutrino masses from $0\nu\beta\beta$ decay to an excited 0^+ state*, Phys. Rev. C **62**, 042501 (2000).

[87] L. S. Brown and G. Gabrielse, *Geonium theory: Physics of a single electron or ion in a Penning trap*, Rev. Mod. Phys. **58**, 233 (1986).

[88] C. Roux, *High-Resolution Mass Spectrometry: The Trap Design and Detection System of PENTATRAP and New Q-Values for Neutrino Studies*, Ph.D. thesis, Universität Heidelberg (2012).

[89] S. Ulmer, *First Observation of Spin Flips with a Single Proton Stored in a Cryogenic Penning Trap*, Ph.D. thesis, Universität Heidelberg (2011).

[90] M. Kretzschmar, *Single particle motion in a Penning trap: description in the classical canonical formalism*, Phys. Scr. **46**, 544 (1992).

[91] J. Ketter, T. Eronen, M. Höcker, S. Streubel and K. Blaum, *First-order perturbative calculation of the frequency-shifts caused by static cylindrically-symmetric electric and magnetic imperfections of a Penning trap*, Int. J. Mass Spectrom. **358**, 1 (2014).

[92] P. J. Mohr, B. N. Taylor and D. B. Newell, *CODATA Recommended Values of the Fundamental Physical Constants: 2010*, J. Phys. Chem. Ref. Data **41**, 043109 (2012).

[93] C. Weinheimer and K. Zuber, *Neutrino Masses*, Annalen Phys. **525**, 565 (2013).

[94] G. Audi *et al.*, *The AME2003 atomic mass evaluation: (II). Tables, graphs and references*, Nucl. Phys. A **729**, 337 (2003).

[95] *Nuclear Levels and Gammas*, National Nuclear Data Center (NNDC), Brookhaven National Laboratory. URL http://www.nndc.bnl.gov.

[96] A. S. Barabash, *Double-beta decay: Present status*, Phys. Atom. Nucl. **73**, 162 (2010).

[97] Vladimir I. Tretyak and Yuri G. Zdesenko, *TABLES OF DOUBLE BETA DECAY DATA–AN UPDATE*, Atom. Data Nucl. Data Tables **80**, 83 (2002).

[98] *Ground States and Ionization Energies*, Atomic Spectra Database, National Institute of Standards and Technology. URL http://www.nist.gov/pml/data/asd.cfm.

[99] P. J. Mohr, B. N. Taylor and D. B. Newell, *CODATA recommended values of the fundamental physical constants: 2006*, Rev. Mod. Phys. **80**, 633 (2008).

[100] S. Rainville, J. Thompson and D. Pritchard, *An Ion Balance for Ultra-High-Precision Atomic Mass Measurements*, Science **303**, 334 (2004).

[101] K. Blaum *et al.*, *Recent developments at ISOLTRAP: towards a relative mass accuracy of exotic nuclei below* 10^{-8}, J. Phys. B: At. Mol. Opt. Phys. **36**, 921 (2003).

[102] E. A. Cornell, R. M. Weisskoff, K. R. Boyce and D. E. Pritchard, *Mode coupling in a Penning trap: π pulses and a classical avoided crossing*, Phys. Rev. A **41**, 312 (1990).

[103] M. Kretzschmar, *The Ramsey method in high-precision mass spectrometry with Penning traps: Theoretical foundations*, Int. J. Mass Spectrom. **264**, 122 (2007).

[104] M. Kretzschmar, *On the phase dependence of the interconversion of the motional modes in a Penning trap by quadrupolar excitation*, Int. J. Mass Spectrom. **309**, 30 (2012).

[105] N. F. Ramsey, *A New Molecular Beam Resonance Method*, Phys. Rev. **76**, 996 (1949).

[106] N. F. Ramsey, *A Molecular Beam Resonance Method with Separated Oscillating Fields*, Phys. Rev. **78**, 695 (1950).

[107] S. George *et al.*, *The Ramsey method in high-precision mass spectrometry with Penning traps: Experimental results*, Int. J. Mass Spectrom. **264**, 110 (2007).

[108] S. Eliseev and C. Roux *et al.*, *Octupolar-Excitation Penning-Trap Mass Spectrometry for Q-Value Measurement of Double-Electron Capture in* ^{164}Er, Phys. Rev. Lett. **107**, 152501 (2011).

[109] M. Rosenbusch *et al.*, *A study of octupolar excitation for mass-selective centering in Penning traps*, Int. J. Mass Spectrom. **314**, 6 (2012).

[110] R. Ringle, G. Bollen, P. Schury, S. Schwarz and T. Sun, *Octupolar excitation of ion motion in a Penning trap – A study performed at LEBIT*, Int. J. Mass Spectrom. **262**, 33 (2007).

[111] G. Savard *et al.*, *A new cooling technique for heavy ions in a Penning trap*, Phys. Lett. A **158**, 247 (1991).

[112] M. König, G. Bollen, H.-J. Kluge, T. Otto and J. Szerypo, *Quadrupole excitation of stored ion motion at the true cyclotron frequency*, Int. J. Mass Spectrom. **142**, 95 (1995).

[113] M. Kretzschmar, *Calculating damping effects for the ion motion in a Penning trap*, Eur. Phys. J. D **48**, 313 (2008).

[114] S. George *et al.*, *Damping effects in Penning trap mass spectrometry*, Int. J. Mass Spectrom. **299**, 102 (2011).

[115] G. Münzenberg *et al.*, *The velocity filter ship, a separator of unslowed heavy ion fusion products*, Nucl. Instrum. Methods **161**, 65 (1979).

[116] M. Dworschak *et al.*, *Penning trap mass measurements on nobelium isotopes*, Phys. Rev. C **81**, 064312 (2010).

[117] M. Block *et al.*, *Mass Measurements of No and Lr isotopes with SHIPTRAP*, GSI Scientific Report (2010).

[118] M. Block *et al.*, *Direct mass measurements above uranium bridge the gap to the island of stability*, Nature **463**, 785 (2010).

[119] M. Dworschak, *First direct mass measurements on nobelium and lawrencium with the Penning trap mass spectrometer SHIPTRAP*, Ph.D. thesis, Universität Mainz (2009).

[120] M. Block *et al.*, *Towards direct mass measurements of nobelium at SHIPTRAP*, Eur. Phys. J. D **45**, 39 (2007).

[121] A. Chaudhuri *et al.*, *Carbon-cluster mass calibration at SHIPTRAP*, Eur. Phys. J. D **45**, 47 (2007).

[122] G. Sikler, *Massenspektrometrie kurzlebiger Sr- und Sn-Isotope und Aufbau der SHIPTRAP-Penningfallen*, Ph.D. thesis, Universität Heidelberg (2003).

[123] C. Droese *et al.*, *Investigation of the magnetic field fluctuation and implementation of a temperature and pressure stabilization at SHIPTRAP*, Nucl. Instrum. Meth. A **632**, 157 (2011).

[124] M. Block *et al.*, *Penning trap mass measurements of transfermium elements with SHIPTRAP*, Hyperfine Interact. **196**, 225 (2010).

[125] M. Mukherjee *et al.*, *ISOLTRAP: An on-line Penning trap for mass spectrometry on short-lived nuclides*, Eur. Phys. J. A **35**, 1 (2008).

[126] J. K. *et al.*, *Recent developments in ion detection techniques for Penning trap mass spectrometry at TRIGA-TRAP*, Eur. Phys. J. A **42**, 311 (2009).

[127] C. Roux *et al.*, *Data analysis of Q-value measurements for double-electron capture with SHIPTRAP*, The European Physical Journal D **67**, 1 (2013).

[128] R. T. Birge, *The Calculation of Errors by the Method of Least Squares*, Phys. Rev. **40**, 207 (1932).

[129] P. J. Mohr and B. N. Taylor, *CODATA recommended values of the fundamental physical constants: 1998*, Rev. Mod. Phys. **72**, 351 (2000).

[130] R. S. Van Dyck, F. L. Moore, D. L. Farnham and P. B. Schwinberg, *Number dependency in the compensated Penning trap*, Phys. Rev. A **40**, 6308 (1989).

[131] G. Bollen *et al.*, *Resolution of nuclear ground and isomeric states by a Penning trap mass spectrometer*, Phys. Rev. C **46**, R2140 (1992).

[132] M. P. Bradley, J. V. Porto, S. Rainville, J. K. Thompson and D. E. Pritchard, *Penning Trap Measurements of the Masses of* ^{133}Cs, $^{85,87}Rb$, *and* ^{23}Na *with Uncertainties* ≤ 0.2 *ppb*, Phys. Rev. Lett. **83**, 4510 (1999).

[133] S. Eliseev and C. Roux *et al.*, *Resonant Enhancement of Neutrinoless Double–Electron Capture in* ^{152}Gd, Phys. Rev. Lett. **106**, 052504 (2011).

[134] C. Droese *et al.*, *Probing the nuclide* ^{180}W *for neutrinoless double-electron capture exploration*, Nucl. Phys. A **875**, 1 (2012).

[135] S. Eliseev and M. Goncharov *et al.*, *Multiple-resonance phenomenon in neutrinoless double-electron capture*, Phys. Rev. C **84**, 012501 (2011).

[136] S. Rahaman *et al.*, *Accurate Q Value for the* ^{112}Sn *Double-*β *Decay and its Implication for the Search of the Neutrino Mass*, Phys. Rev. Lett. **103**, 042501 (2009).

[137] V. S. Kolhinen *et al.*, *On the resonant neutrinoless double-electron-capture decay of* ^{136}Ce, Phys. Lett. B **697**, 116 (2011).

[138] V. S. Kolhinen *et al.*, *Accurate Q value for the* ^{74}Se *double-electron-capture decay*, Phys. Lett. B **684**, 17 (2010).

[139] B. J. Mount, M. Redshaw and E. G. Myers, *Double-*β*-decay Q values of* ^{74}Se *and* ^{76}Ge, Phys. Rev. C **81**, 032501 (2010).

[140] C. Smorra *et al.*, *Q value and half-life of double-electron capture in* ^{184}Os, Phys. Rev. C **86**, 044604 (2012).

[141] D. A. Nesterenko *et al.*, *Double-β transformations in isobaric triplets with mass numbers A = 124, 130, and 136*, Phys. Rev. C **86**, 044313 (2012).

[142] S. Eliseev *et al.*, *Q values for neutrinoless double-electron capture in* ^{96}Ru, ^{162}Er *and* ^{168}Yb, Phys. Rev. C **83**, 038501 (2011).

[143] K. Blaum, J. Dilling and W. Nörtershäuser, *Precision atomic physics techniques for nuclear physics with radioactive beams*, Phys. Scr. **2013**, 014017 (2013).

[144] G. Bollen *et al.*, *First absolute mass measurements of short-lived isotopes*, Hyperfine Interact. **38**, 793 (1987).

[145] M. Mukherjee *et al.*, *Mass measurements and evaluation around A = 22*, Eur. Phys. J. A **35**, 31 (2008).

[146] H.-J. Kluge, *Penning trap mass spectrometry of radionuclides*, Int. J. Mass Spectrom. **349-350**, 26 (2013). 100 years of Mass Spectrometry.

[147] C. Rauth *et al.*, *First Penning Trap Mass Measurements beyond the Proton Drip Line*, Phys. Rev. Lett. **100**, 012501 (2008).

[148] C. Weber *et al.*, *Mass measurements in the vicinity of the rp-process and the νp-process paths with the Penning trap facilities JYFLTRAP and SHIPTRAP*, Phys. Rev. C **78**, 054310 (2008).

[149] V.-V. Elomaa *et al.*, *Quenching of the SnSbTe Cycle in the rp Process*, Phys. Rev. Lett. **102**, 252501 (2009).

[150] D. Lunney, J. M. Pearson and C. Thibault, *Recent trends in the determination of nuclear masses*, Rev. Mod. Phys. **75**, 1021 (2003).

[151] V. L. Ryjkov *et al.*, *Direct Mass Measurement of the Four-Neutron Halo Nuclide* ^{8}He, Phys. Rev. Lett. **101**, 012501 (2008).

[152] C. Fröhlich *et al.*, *Neutrino-Induced Nucleosynthesis of A > 64 Nuclei: The νp Process*, Phys. Rev. Lett. **96**, 142502 (2006).

[153] H. Schatz *et al.*, *End Point of the rp Process on Accreting Neutron Stars*, Phys. Rev. Lett. **86**, 3471 (2001).

[154] R. Wolf *et al.*, *On-line separation of short-lived nuclei by a multi-reflection time-of-flight device*, Nucl. Instrum. Meth. A **686**, 82 (2012).

[155] R. Wolf *et al.*, *ISOLTRAP's multi-reflection time-of-flight mass separator/spectrometer*, Int. J. Mass Spectrom. **349–350**, 123 (2013). 100 years of Mass Spectrometry.

[156] G. Eitel *et al.*, *Position-sensitive ion detection in precision Penning trap mass spectrometry*, Nucl. Instrum. Methods **606**, 475 (2009).

[157] G. Bollen, *Mass measurements of short-lived nuclides with ion traps*, Nucl. Phys. A **693**, 3 (2001). Radioactive Nuclear Beams.

[158] A. Chaudhuri, *Carbon-cluster mass calibration at SHIPTRAP*, Ph.D. thesis, Universität Greifswald (2007).

[159] O. Jagutzki *et al.*, *Position sensitive anodes for MCP read-out using induced charge measurement*, Nucl. Instrum. Meth. A **477**, 256 (2002). 5th Int. Conf. on Position-Sensitive Detectors.

[160] RoentDek GmbH URL http://www.roentdek.com.

[161] J. Ketelaer *et al.*, *TRIGA-SPEC: A setup for mass spectrometry and laser spectroscopy at the research reactor TRIGA Mainz*, Nucl. Instrum Meth. A **594**, 162 (2008).

[162] D. Neidherr *et al.*, *Measurement and simulation of the pressure ratio between the two traps of double Penning trap mass spectrometers*, Nucl. Instrum. Meth. B **266**, 4556 (2008).

[163] E. Minaya Ramirez *et al.*, in preparation (2014).

[164] V. P. Ovsyannikov and G. Zschornack, *First investigations of a warm electron beam ion trap for the production of highly charged ions*, Rev. Sci. Instrum. **70**, 2646 (1999).

[165] U. Kentsch, G. Zschornack, A. Schwan and F. Ullmann, *Short time ion pulse extraction from the Dresden electron beam ion trap*, Rev. Sci. Instrum. **81**, 02A507 (2010).

[166] J. R. Crespo López-Urrutia *et al.*, *Optimization of the charge state distribution of the ion beam extracted from an EBIT by dielectronic recombination*, Rev. Sci. Instrum. **75**, 1560 (2004).

[167] J. Repp, *The setup of the high-precision Penningtrap mass spectrometer PENTATRAP and first production studies of highly charged ions*, Ph.D. thesis, Universität Heidelberg (2012).

[168] A. Rischka, *Aufbau und Charakterisierung eines Systems zur Stabilisierung des Magnetfeldes an PENTATRAP*, Bachelor thesis, Universität Heidelberg (2011).

[169] C. Böhm, Ph.D. thesis (in preparation), Universität Heidelberg (2014).

[170] A. Rischka, Master thesis (in preparation), Universität Heidelberg (2014).

[171] Dr. S. Stahl, Stahl-Electronics URL http://www.stahl-electronics.com/voltage-supplies.html.

[172] A. J. González Martínez *et al.*, *Benchmarking high-field few-electron correlation and QED contributions in Hg^{75+} to Hg^{78+} ions. I. Experiment*, Phys. Rev. A **73**, 052710 (2006).

[173] D. J. Wineland and H. G. Dehmelt, *Principles of the stored ion calorimeter*, J. Appl. Phys. **46**, 919 (1975).

[174] A. Dörr, Ph.D. thesis (in preparation), Universität Heidelberg (2014).

[175] W. Shockley, *Currents to Conductors Induced by a Moving Point Charge*, J. Appl. Phys. **9**, 635 (1938).

[176] S. Stahl, Aufbau eines Experiments zur Bestimmung elektronischer g-Faktoren einzelner wasserstoffähnlicher Ionen, Ph.D. thesis, Universität Heidelberg (1998).

[177] J. B. Johnson, *Thermal Agitation of Electricity in Conductors*, Phys. Rev. **32**, 97 (1928).

[178] S. Sturm, A. Wagner, B. Schabinger and K. Blaum, *Phase-Sensitive Cyclotron Frequency Measurements at Ultralow Energies*, Phys. Rev. Lett. **107**, 143003 (2011).

[179] C. Roux *et al.*, *The trap design of Pentatrap*, Appl. Phys. B **107**, 997 (2012).

[180] D. B. Pinegar, K. Blaum, T. P. Biesiadzinski, S. L. Zafonte and R. S. Van Dyck, *Stable voltage source for Penning trap experiments*, Rev. Sci. Instrum. **80**, 064701 (2009).

[181] Dietrich Beck, Holger Brand, Klaus Poppensieker and Kai Wunderle, *LabVIEW Control Applications for Cave A and SHIPTRAP*, GSI Scientific Report (2002).

[182] CSDeveloperGroup, *CS - A Control System Framework for Experiments*, CS-framework wiki (2014). URL http://wiki.gsi.de/cgi-bin/view/CSframework/.

[183] National Instruments, *LabVIEW System Design Software* (2014). URL http://www.ni.com/labview/.

[184] D. Beck, K. Blaum, H. Brand, F. Herfurth and S. Schwarz, *A new control system for ISOLTRAP*, Nucl. Instrum. Meth. A **527**, 567 (2004).

[185] C. Gaspar and M. Dönszelmann, *DIM: a distributed information management system for the DELPHI experiment at CERN*, Proceedings of the 8th Conference on Real-Time Computer applications in Nuclear, Particle and Plasma Physics p. 156 (1993). URL http://cdsweb.cern.ch/record/254799.

[186] C. Gaspar, M. Dönszelmann and P. Charpentier, *DIM, a Portable, Light Weight Package for Information Publishing, Data Transfer and Inter-process Communication*, Presented at: International Conference on Computing in High Energy and Nuclear Physics (2000). URL http://dim.web.cern.ch/dim/papers/CHEP/DIM.PDF.

[187] D. Beck, LabVIEW-DIM Interface (2014). URL http://wiki.gsi.de/cgi-bin/view/CSframework/LVDimInterface.

Credits

Here I would like to express my appreciation to all the people inspiring me in my work. Maybe I will forget someone, and this order issue... But who cares?

First of all, I would like to thank Klaus Blaum and Yuri Nikolaevich Novikov for a given opportunity to become a part of their great team. Thank you for being patient to all the problems students could have in their life. With your outstanding examples on how one should do his job with a great care and responsibility my experience has grown up tremendously. Thank you, Klaus, for being always positive and spreading around tons of your energy. This helps a lot to all of us! Thank you, Yuri Nikolaevich, for your wise advices and answers to the questions which were quite often beyond the scope of physics. Thank you, my godfathers in physics.

Thanks to Markus Oberthaler for accepting being the second referee of this thesis.

I would like to appreciate the PENTATRAP team. You are the best! With all these depressing moments we have finally managed to give a birth to our baby. Thank you, Sergey, for the first lessons on how one should work in the lab: always aimed for the result, always efficient, never sleeping. Thank you, Christian, for all these stories, soldering lessons, cigarettes and jazz, jazz, jazz... Thank you, Julia and Christine, for keeping everything in order, for you optimism and sense of humor. Thank you, Andreas, for being patient to one dummy with one hundred "why"-questions. Thank you, Alex, for your outstanding help and friendliness. And thank you, guys, for all these cakes and cookies.

Thank you, guys from SHIPTRAP. Many thanks to Michael Block, Enrique and Christian for letting us to mob around your setup and to bother you with all our problems.

Thank you, my MPIK friends. Thanks, Ralf, for your help, Tommi, for your smile, Jochen, for your neverending stories, Sebastian, for your "Fleisch", Marc, for your speed, Marko, for your songs, Andreas, Christoph, Hendrik and Hendrik, Robert, for a cigarette, – thank you all. You are the best colleagues one can ever imaging. Special thanks to Burcu, I will always miss you in my office. And thank you, the guys from MATS!

Now I would like to thank David. Man, you will always be in my heart. I will never

forget our adventures even though they were a bit shorter then I'd like to. Well, you know, now you have a very long adventure, who knows, when we'll meet again. Thank you, Marta! Just thank you as a human being. You were keeping me straight and in mind in the worst cases. Heidelberg and Max Bar have become boring after you left... Thanks, Michi! We were a nice team in everything, and I will never forget the time I spent with you. And Xua, thanks to you, girl! It was really a great time! Many thanks to Martin and Hermine, you're a great couple, thank you for your support in my not the best times!

Thank you, the French invaders! You are outstanding, guys, all of you. Pauline and Carl, all my love to you, guys, I've got a new life after you, you know? And skiing, and Paris, and... Sarah, I will never forget how we met, all our late talks and disputes, from where the truth comes. Antoine (still hard to spell your name), thank you too, you have arrived just in time, you know. I'm glad that you are here in Heidelberg while I'm still here. Seriously!

Thank you, Russian Heidelbergers. Андрей, Саша, спасибо вам за всё! За скалы, поездки, посиделки, шумные и не очень... Мы еще обязательно встретимся!

Спасибо всем моим друзьям из Севастополя и Санкт-Петербурга. Миша и Настя, вы практически моя семья, Вова и Кира, Саша и Света, и все, все, все, – вы те самые друзья, о которых можно мечтать. Аня Беседа и Светлана Николаевна, вы мои лучи культурного света в этом темном царстве невежества. Не унывайте, гражданки с Фонтанки! Спасибо вам всем за поддержку!

Оленька, ты моё всё. Не знаю, как бы получилось написать эту диссертацию без твоей поддержки. Спасибо, что ты есть, моя девочка.

I have dedicated this thesis first of all *in memoriam* of my parents. I don't know how else to express my appreciation to them, so I have to stop here.

Огромное всем спасибо!